

Precision and accuracy of single-molecule FRET measurements—a multi-laboratory benchmark study

Björn Hellenkamp^{1,2,33}, Sonja Schmid^{1,3,33}, Olga Doroshenko⁴, Oleg Opanasyuk⁴, Ralf Kühnemuth⁴, Soheila Rezaei Adariani⁵, Benjamin Ambrose⁶, Mikayel Aznauryan⁷, Anders Barth⁸, Victoria Birkedal⁷, Mark E. Bowen⁹, Hongtao Chen¹⁰, Thorben Cordes^{11,12}, Tobias Eilert¹³, Carel Fijen¹⁴, Christian Gebhardt¹², Markus Götz¹, Giorgos Gouridis^{11,12}, Enrico Gratton¹⁰, Taekjip Ha¹⁵, Pengyu Hao¹⁶, Christian A. Hanke⁴, Andreas Hartmann¹⁷, Jelle Hendrix^{18,19}, Lasse L. Hildebrandt⁷, Verena Hirschfeld²⁰, Johannes Hohlbein^{14,21}, Boyang Hua¹⁵, Christian G. Hübner²⁰, Eleni Kallis¹³, Achillefs N. Kapanidis²², Jae-Yeol Kim²³, Georg Krainer^{17,24}, Don C. Lamb⁸, Nam Ki Lee²³, Edward A. Lemke^{25,26,27}, Brié Levesque⁹, Marcia Levitus²⁸, James J. McCann⁹, Nikolaus Naredi-Rainer⁸, Daniel Nettels²⁹, Thuy Ngo¹⁵, Ruoyi Qiu¹⁶, Nicole C. Robb²², Carlheinz Röcker¹³, Hugo Sanabria⁵, Michael Schlierf¹⁷, Tim Schröder³⁰, Benjamin Schuler²⁹, Henning Seidel²⁰, Lisa Streit¹³, Johann Thurn¹, Philip Tinnefeld^{30,31}, Swati Tyagi²⁷, Niels Vandenberg¹⁸, Andrés Manuel Vera³⁰, Keith R. Weninger¹⁶, Bettina Wünsch³¹, Inna S. Yanez-Orozco⁵, Jens Michaelis^{13*}, Claus A. M. Seidel^{4*}, Timothy D. Craggs^{6,22*} and Thorsten Hugel^{1,32*}

Single-molecule Förster resonance energy transfer (smFRET) is increasingly being used to determine distances, structures, and dynamics of biomolecules in vitro and in vivo. However, generalized protocols and FRET standards to ensure the reproducibility and accuracy of measurements of FRET efficiencies are currently lacking. Here we report the results of a comparative blind study in which 20 labs determined the FRET efficiencies (E) of several dye-labeled DNA duplexes. Using a unified, straightforward method, we obtained FRET efficiencies with s.d. between ± 0.02 and ± 0.05 . We suggest experimental and computational procedures for converting FRET efficiencies into accurate distances, and discuss potential uncertainties in the experiment and the modeling. Our quantitative assessment of the reproducibility of intensity-based smFRET measurements and a unified correction procedure represents an important step toward the validation of distance networks, with the ultimate aim of achieving reliable structural models of biomolecular systems by smFRET-based hybrid methods.

FRET¹, also known as fluorescence resonance energy transfer, is a well-established method for studying biomolecular conformations and dynamics at both the ensemble^{2–4} and the single-molecule level^{5–10}. In such experiments, the energy transfer between donor and acceptor fluorophores is quantified with respect to their proximity¹. The fluorophores are usually attached via flexible linkers to defined positions of the system under investigation. The transfer efficiency depends on the interdyer distance, which is well described by Förster's theory for distances $> 30 \text{ \AA}$ ^{11,12}. Accordingly, FRET has been termed a 'spectroscopic ruler' for measurements on the molecular scale², capable of determining distances in vitro, and even in cells¹³, with potentially ångström-level accuracy and precision. In its single-molecule implementation, FRET largely overcomes ensemble-averaging and time-averaging and can uncover individual species in heterogeneous and dynamic biomolecular complexes, as well as transient intermediates⁵.

The two most popular smFRET approaches for use in determining distances are confocal microscopy of freely diffusing molecules

in solution and total internal reflection fluorescence (TIRF) microscopy of surface-attached molecules. Various fluorescence-intensity- and lifetime-based procedures have been proposed with the aim of determining FRET efficiencies^{10,14–20}. Here we focus on intensity-based measurements in which the FRET efficiency E is determined from donor and acceptor photon counts and subsequently used to calculate the interfluorophore distance according to Förster's theory.

So far most intensity-based smFRET studies have characterized relative changes in FRET efficiency. This ratiometric approach is often sufficient to distinguish different conformations of a biomolecule (e.g., an open conformation with low FRET efficiency versus a closed conformation with high FRET efficiency) and to determine their interconversion kinetics. However, knowledge about distances provides additional information that can be used, for example, to compare an experimental structure with known structures, or to assign conformations to different structural states. In combination with other structural measurements and computer simulations,

A full list of affiliations appears at the end of the paper.

FRET-derived distances are increasingly being used to generate novel biomolecular structural models via hybrid methods^{7–9,21–26}.

However, it is difficult to compare and validate distance measurements from different labs, especially when detailed methodological descriptions are lacking. In addition, different methods for data acquisition and analysis, which often involve custom-built microscopes and in-house software, can have very different uncertainties and specific pitfalls. To overcome these issues, here we describe general methodological recommendations and well-characterized standard samples for FRET that can enable researchers to validate results and estimate the accuracy and precision of distance measurements. This approach should allow the scientific community to confirm the consistency of smFRET-derived distances and structural models. To facilitate data validation across the field, we recommend the use of a unified nomenclature to report specific FRET-related parameters.

The presented step-by-step procedure for obtaining FRET efficiencies and relevant correction parameters was tested in a worldwide, comparative, blind study by 20 participating labs. We show that, for standardized double-stranded DNA FRET samples, FRET efficiencies can be determined with an s.d. value of less than ± 0.05 .

To convert the measured smFRET efficiencies to distances, we used the Förster equation (equation (3); all numbered equations cited in this paper can be found in the Methods section), which critically depends on the dye-pair-specific Förster radius, R_0 . We discuss the measurements required to determine R_0 and the associated uncertainties. Additional uncertainty arises from the fact that many positions are sampled by the dye relative to the biomolecule to which it is attached. Therefore, specific models are used to describe the dynamic movement of the dye molecule during the recording of each FRET-efficiency measurement^{22,23}. The investigation of the uncertainties in FRET-efficiency determination and the conversion into distance measurements enabled us to specify uncertainties for individual FRET-derived distances.

Results

Benchmark samples and approaches. We chose double-stranded DNA as a FRET standard for several reasons: DNA sequences can be synthesized, FRET dyes can be specifically tethered at desired positions, the structure of B-form DNA is well characterized, and the samples are stable at room temperature long enough that they can be shipped to labs around the world. The donor and acceptor dyes were attached via C2 or C6 amino linkers to thymidines of opposite strands (Supplementary Fig. 1). These thymidines were separated by 23 bp, 15 bp (Fig. 1), or 11 bp (Supplementary Fig. 1, Supplementary Table 1, and Supplementary Note 1). The attachment positions were known only to the reference lab that designed the samples. The samples were designed in such a way that we were able to determine all correction parameters and carry out a self-consistency test (described below).

In this study we used Alexa Fluor and Atto dyes because of their high quantum yields and well-studied characteristics (Supplementary Note 2). Eight hybridized double-stranded FRET samples were shipped to all participating labs. In the main text, we focus on four FRET samples that were measured by most labs in our study:

- 1-lo: Atto 550/Atto 647N; 23-bp separation
- 1-mid: Atto 550/Atto 647N; 15-bp separation
- 2-lo: Atto 550/Alexa Fluor 647; 23-bp separation
- 2-mid: Atto 550/Alexa Fluor 647; 15-bp separation

In revision, 13 labs evaluated two additional samples:

- 1-hi: Atto 550/Atto 647N; 11-bp separation
- 2-hi: Atto 550/Alexa Fluor 647; 11-bp separation

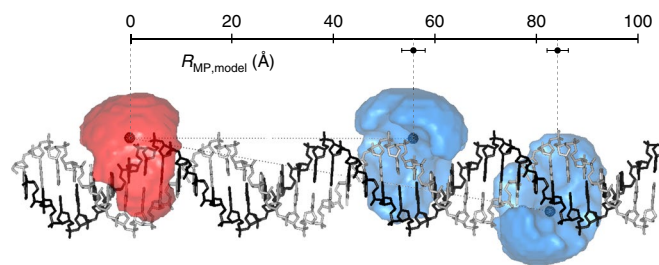


Fig. 1 | Schematic of the FRET standard molecules. Double-stranded DNA was labeled with a FRET pair at 15-bp or 23-bp separation for the “lo” and “mid” samples, respectively (sequences are provided in the Methods). The accessible volumes (AVs) of the dyes (donor, blue; acceptor, red) are illustrated as semi-transparent surfaces and were calculated with freely available software⁸. The mean dye positions are indicated by darker spheres (assuming homogeneously distributed dye positions; Supplementary Note 3). The distance between the mean dye positions is defined as $R_{MP,model}$. Calculated values for $R_{MP,model}$ and the errors obtained by varying parameters of the AV model are shown (Supplementary Note 3). The B-DNA model was generated with Nucleic Acid Builder version 04/17/2017 for Amber²⁷.

In this nomenclature, the number refers to the dye pair, and lo, mid, and hi indicate low-efficiency, medium-efficiency, and high-efficiency configurations, respectively. The results with other FRET pairs (Alexa Fluor 488/Alexa Fluor 594 and Alexa Fluor 488/Atto 647N) at these positions, per lab, for all samples and for different methods, are reported in Supplementary Fig. 2 and Supplementary Note 2.

To avoid dye stacking^{28,29}, we designed the DNA molecules such that the dyes were attached to internal positions sufficiently far from the duplex ends. As a first test for the suitability of the labels, we checked the fluorescence lifetimes and time-resolved anisotropies (Supplementary Table 2) of all donor-only and acceptor-only samples. The results indicated that there was no significant quenching or stacking and that all dyes were sufficiently mobile at these positions (Supplementary Note 2).

Most measurements were carried out on custom-built setups that featured at least two separate spectral detection channels for donor and acceptor emission (Supplementary Figs. 3 and 4). Results obtained with different fluorophores (samples 3 and 4) and different FRET methods (ensemble lifetime³⁰, single-molecule lifetime¹⁶, and a phasor approach³¹) are presented in Supplementary Fig. 2 and Supplementary Notes 1 and 2.

A robust correction procedure to determine absolute fluorescence intensities is needed. The ideal solution is a ratiometric approach that, for intensity-based confocal FRET measurements, was pioneered by Weiss and coworkers and uses alternating two-color laser excitation (ALEX) with microsecond pulses^{17,32}. In this approach the fluorescence signal after donor excitation is divided by the total fluorescence signal after donor and acceptor excitation (referred to as apparent stoichiometry; see equation (16)), to correct for dye and instrument properties¹⁷. The ALEX approach was also adapted for TIRF measurements²⁰. To increase time resolution and to enable time-resolved spectroscopy, Lamb and coworkers introduced pulsed interleaved excitation with picosecond pulses³³.

Procedure to determine the experimental FRET efficiency $\langle E \rangle$.

In both confocal and TIRF microscopy, the expectation value of the FRET efficiency $\langle E \rangle$ is computed from the corrected FRET efficiency histogram. In this section, first we outline a concise and robust procedure to obtain $\langle E \rangle$. Then we describe distance and uncertainty calculations, assuming a suitable model for the interdye distance distribution and dynamics^{6,11,34}. Finally, we derive self-consistency

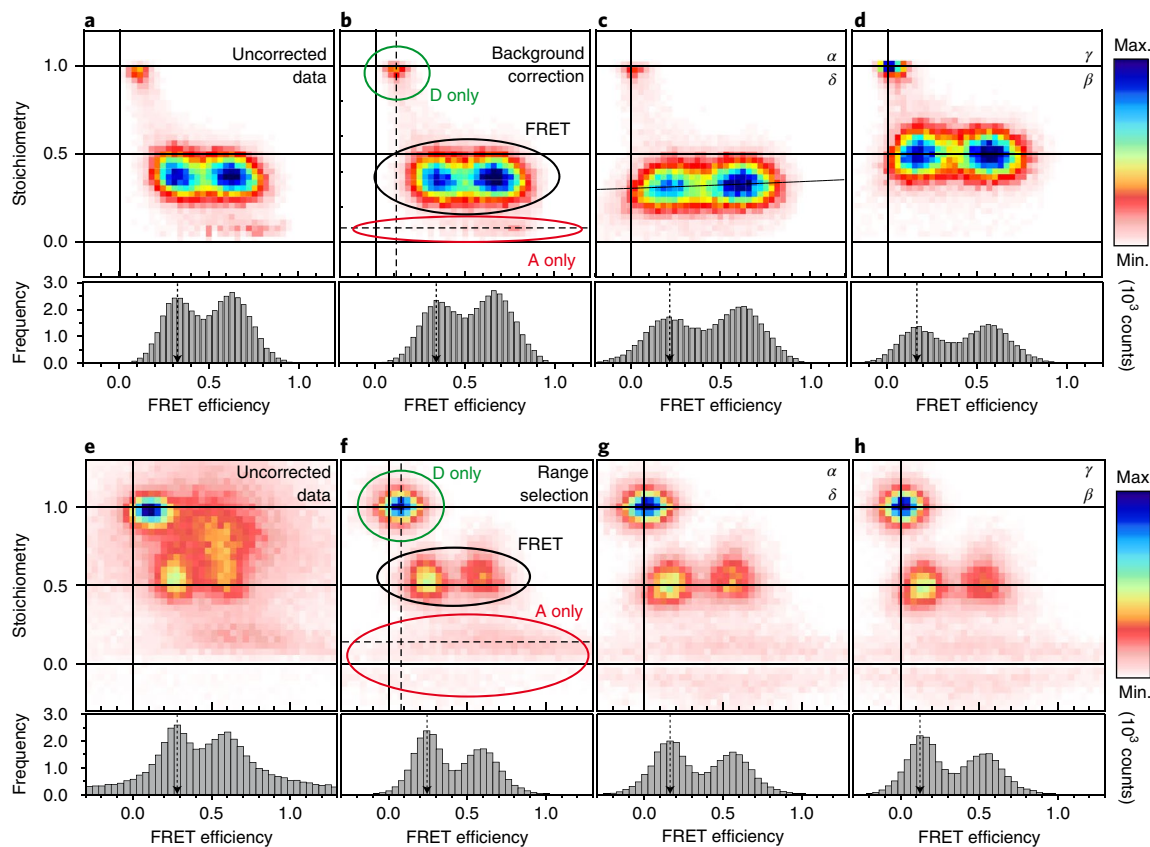


Fig. 2 | Stepwise data correction for 1-lo and 1-mid samples. **a–d**, Workflow for correction of the confocal data for background (**a** → **b**); leakage (factor α); and direct excitation (δ) (**b** → **c**), excitation, and detection factors (β , γ) (**c** → **d**). **e–h**, Workflow for correction of TIRF data for background and photobleaching by selection of the prebleached range (**e** → **f**); leakage; and direct excitation (**f** → **g**), detection, and excitation factors (**g** → **h**). The efficiency histograms show a projection of the data with a stoichiometry between 0.3 and 0.7. The general terms “stoichiometry” and “FRET efficiency” are used in place of the corresponding specific terms for each correction step. Donor (D)-only, FRET, and acceptor (A)-only populations are specified.

arguments and comparisons to structural models to confirm the accuracy of this approach.

Our general procedure is largely based on a previous approach¹⁷, with modifications to establish a robust workflow and standardize the nomenclature. Intensity-based determination of FRET efficiencies requires consideration of the following correction factors (details in the Methods section): background signal correction (BG) from donor and acceptor channels; α , a factor for spectral cross-talk arising from donor fluorescence leakage in the acceptor channel; δ , a factor for direct excitation of the acceptor with the donor laser; and a detection correction factor (γ). The optimal way to determine these factors is to alternate the excitation between two colors, which allows for determination of the FRET efficiency (E) and the relative stoichiometry (S) of donor and acceptor dyes, for each single-molecule event. This requires the additional excitation correction factor β to normalize the excitation rates.

The following step-by-step guide presents separate instructions for confocal and TIRF experiments; notably, the order of the steps is crucial (Methods).

Diffusing molecules: confocal microscopy. Photon arrival times from individual molecules freely diffusing through the laser focus of a confocal microscope are registered. Signal threshold criteria are applied, and bursts are collected and analyzed. From the data, first a 2D histogram of the uncorrected FRET efficiency (E_{app}) versus the uncorrected stoichiometry (S_{app}) is generated (Fig. 2a). Then the average number of background photons is subtracted for each channel separately (Fig. 2b). Next, to obtain the FRET sensitized acceptor

signal ($F_{A|D}$), one must subtract the donor leakage ($\alpha^d I_{D_{em}|D_{ex}}$) and direct excitation ($\delta^{ii} I_{A_{em}|A_{ex}}$) from the acceptor signal after donor excitation. As samples never comprise 100% photoactive donor and acceptor dyes, the donor-only and acceptor-only populations are selected from the measurement and used to determine the leakage and direct excitation (Fig. 2c). After this correction step, the donor-only population should have an average FRET efficiency of 0, and the acceptor-only population should have an average stoichiometry of 0.

The last step deals with the detection correction factor γ and the excitation correction factor β . If at least two species (two different samples or two populations within a sample) with different interdy distances are present, they can be used to obtain the ‘global γ -correction’. If one species with substantial distance fluctuations (e.g., from intrinsic conformational changes) is present, a ‘single-species γ -correction’ may be possible. Both correction schemes assume that the fluorescence quantum yields and extinction coefficients of the dyes are independent of the attachment point. The correction factors obtained by the reference lab are compiled in Supplementary Table 3. The final corrected FRET efficiency histograms are shown in Fig. 2d. The expected efficiencies ($\langle E \rangle$) are obtained as the mean of a Gaussian fit to the respective efficiency distributions. After correction, we noted a substantial shift of the FRET-efficiency peak positions, especially for the low-FRET-efficiency peak ($E \sim 0.25$ uncorrected to $E \sim 0.15$ when fully corrected).

Surface-attached molecules: TIRF microscopy. The correction procedure for TIRF-based smFRET experiments is similar to the

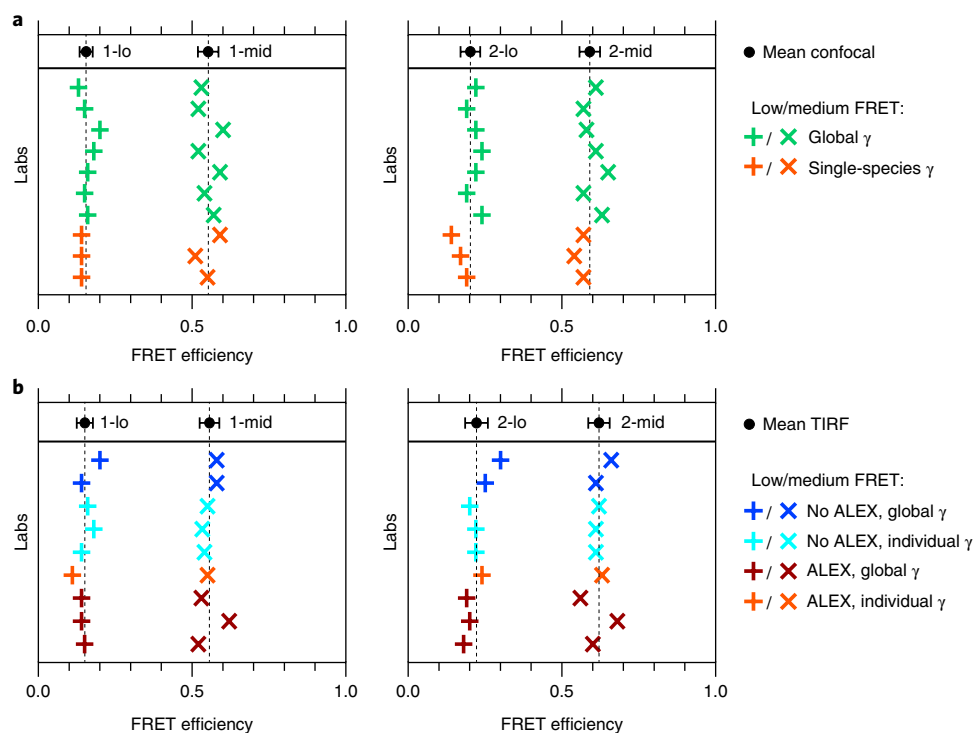


Fig. 3 | Summary of the results of the intensity-based methods. a, Confocal measurements. **b**, TIRF measurements. Note that some laboratories performed measurements with both methods. The mean \pm s.d. is depicted in the upper portion of each plot. Dashed lines indicate mean values (summarized in Supplementary Table 4). Example correction factors are given in Supplementary Table 3.

procedure for confocal-based experiments. In the procedure used for ALEX data²⁰, a 2D histogram of the uncorrected FRET efficiency versus the uncorrected stoichiometry is generated (Fig. 2e). The background subtraction is critical in TIRF microscopy, as it can contribute substantially to the measured signal. Different approaches can be used to accurately determine the background signal, such as measuring the background in the vicinity of the selected particle or measuring the intensity after photobleaching (Fig. 2f). After background correction, the leakage and direct excitation can be calculated from the ALEX data as for confocal microscopy (Fig. 2g).

Again, determination of the correction factors β and γ is critical¹⁵. As with confocal microscopy, one can use the stoichiometry information available from ALEX when multiple populations are present to determine an average detection correction factor (global γ -correction). In TIRF microscopy, the detection correction factor can also be determined on a molecule-by-molecule basis, provided the acceptor photobleaches before the donor (individual γ -correction). In this case, the increase in the fluorescence of the donor can be directly compared to the intensity of the acceptor before photobleaching. A 2D histogram of corrected FRET efficiency versus corrected stoichiometry is shown in Fig. 2h.

In the absence of alternating laser excitation, the following problems occasionally arose during this study: (i) the low-FRET-efficiency values were shifted systematically to higher efficiencies, because FRET-efficiency values at the lower edge were overlooked owing to noise; (ii) the direct excitation was difficult to detect and correct because of its small signal-to-noise ratio; and (iii) acceptor bleaching was difficult to detect for low FRET efficiencies. Therefore, we strongly recommend implementing ALEX in order to obtain accurate FRET data.

Nine of the twenty participating labs determined FRET efficiencies by confocal methods for samples 1 and 2 (Fig. 3a). Seven of the twenty participating labs determined FRET efficiencies by TIRF-based methods (Fig. 3b). The combined data from all labs for

measurements of samples 1 and 2 agree very well, with s.d. for the complete dataset of $\Delta E < \pm 0.05$. This is a remarkable result, considering that different setup types were used (confocal- and TIRF-based setups) and different correction procedures were applied (e.g., individual, global, or single-species γ -correction).

Distance determination. The ultimate goal of this approach is to derive distances from FRET efficiencies. The efficiency-to-distance conversion requires knowledge of the Förster radius, R_0 , for the specific FRET pair used and of a specific dye model describing the behavior of the dye attached to the macromolecule^{22,23}. In the following, we describe (i) how R_0 can be determined and (ii) how to use a specific dye model to calculate two additional values, $R_{(E)}$ and R_{MP} . $R_{(E)}$ is the apparent distance between the donor and the acceptor, which is directly related to the experimental FRET efficiency (E) that is averaged over all sampled donor–acceptor distances R_{DA} (equation (5)), but it is not a physical distance. R_{MP} is the real distance between the center points (mean positions) of the accessible volumes and deviates from $R_{(E)}$ because of the different averaging in distance and efficiency space. R_{MP} cannot be measured directly but is important, for example, for mapping the physical distances required for structural modeling³⁴.

R_0 is a function of equation (7) and depends on the index of refraction of the medium between the two fluorophores (n_{im}), the spectral overlap integral (J), the fluorescence quantum yield of the donor (Φ_{FD}), and the relative dipole orientation factor (κ^2) (an estimate of their uncertainties is provided in the Methods section). Our model assumes that the FRET rate (k_{FRET}) is much slower than the rotational relaxation rate (k_{rot}) of the dye and that the translational diffusion rate (k_{diff}) allows the dye to sample the entire accessible volume within the experimental integration time ($1/k_{int}$), that is, $k_{rot} \gg k_{FRET} \gg k_{diff} \gg k_{int}$. The validity of these assumptions is justified by experimental observables discussed in the Methods.

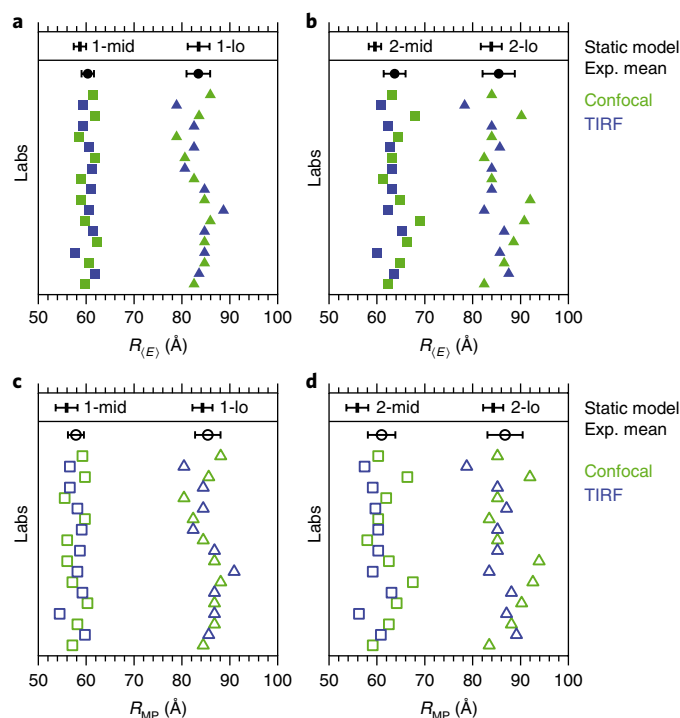


Fig. 4 | Mean interdyne distances determined from 19 $\langle E \rangle$ values measured in 16 different labs. a, b, $R_{(E)}$ for samples 1 (a) and 2 (b). **c, d**, R_{MP} for samples 1 (c) and 2 (d). Data are shown as individual values (colored symbols) and as the mean (black dots) and s.d., assuming $R_0 = 62.6 \text{ \AA}$ and $R_0 = 68.0 \text{ \AA}$ for samples 1 and 2, respectively. The black bars at the top of each plot indicate the static model values and their error (determined by variation of model parameters); see Supplementary Table 4 for values. The depicted errors include only the statistical variations of the FRET efficiencies, and do not include the error in the Förster radii; thus these errors represent the precision of the measurement, but not the accuracy. Exp., experimental.

The determined Förster radii for samples 1 and 2 are given in Supplementary Table 4. Note that literature values differ mainly because donor fluorescence quantum yields are not specified and the refractive index of water is often assumed, whereas we used $n_{im} = 1.40$ here. Our careful error analysis led to an error estimate of 7% for the determined R_0 , which is relatively large (mainly owing to the uncertainty in κ^2).

We used the measured smFRET efficiencies and the calculated Förster radii to compute the apparent distance $R_{(E)}$ from each lab's data (equation (5)). Figure 4a,b shows the calculated values for these apparent distances for samples 1 and 2 for each data point in Fig. 3. The average values for all labs are given in Supplementary Table 4, together with model values based on knowledge of the dye attachment positions, the static DNA structure, and the mobile dye model (Supplementary Note 3). Considering the error ranges, the experimental and model values agree very well with each other (the deviations range between 0 and 8%).

Although this study focused on measurements on DNA, the described FRET analysis and error estimation are fully generalizable to other systems (e.g., proteins), assuming mobile dyes are used. What becomes more difficult with proteins is specific dye labeling, and the determination of an appropriate dye model, if the dyes are not sufficiently mobile (Supplementary Note 3). $R_{(E)}$ corresponds to the real distance R_{MP} only in the hypothetical case in which both dyes are unpolarized point sources, with zero accessible volume (AV). In all other cases, R_{MP} is the only physical distance. It can be calculated in two ways: (i) if the dye model and the local environment of the dye are known, simulation tools such as the FRET

Positioning and Screening tool⁸ can be used to compute R_{MP} from $R_{(E)}$ for a given pair of AVs; or (ii) if the structure of the investigated molecule is unknown a priori, a sphere is a useful assumption for the AV. In both cases, a lookup table is used to convert $R_{(E)}$ to R_{MP} for defined AVs and R_0 values (Supplementary Note 5). Our results for these calculations, given as distances determined via the former approach, are shown in Fig. 4c,d and Supplementary Table 4. The respective model values are based on the center points of the AVs depicted in Fig. 1 and given in Supplementary Table 4 (details in Supplementary Note 3).

Distance uncertainties. We estimated all uncertainty sources arising from both the measurement of the corrected FRET efficiencies and the determination of the Förster radius, and propagated them into distance uncertainties. We discuss the error in determining the distance between two freely rotating but spatially fixed dipoles, R_{DA} , with the Förster equation (equation (26)). Figure 5a shows how uncertainty in each of the correction factors (α , γ , and δ) and the background signals (BG_D , BG_A) is translated into the uncertainty of R_{DA} (Supplementary Note 6). The uncertainty of R_{MP} is similar but depends on the dye model and the AVs. The solid gray line in Fig. 5a shows the sum of these efficiency-dependent uncertainties, which are mainly setup-specific quantities. For the extremes of the distances, the largest contribution to the uncertainty in R_{DA} arises from background photons in the donor and acceptor channels. In the presented example with $R_0 = 62.6 \text{ \AA}$, the total uncertainty ΔR_{DA} based on the setup-specific uncertainties is less than 4 \AA for $35 \text{ \AA} < R_{DA} < 90 \text{ \AA}$. Notably, in confocal measurements, larger intensity thresholds can decrease this uncertainty further. The uncertainty in R_{DA} arising from errors in R_0 (blue line in Fig. 5b) is added to the efficiency-related uncertainty in R_{DA} (bold gray line in Fig. 5b) to estimate the total experimental uncertainty in R_{DA} (black line in Fig. 5b). The uncertainties for determining R_0 are dominated by the dipole orientation factor κ^2 and the refractive index n_{im} (Methods). Including the uncertainty in R_0 , the error $\Delta R_{DA, total}$ for a single smFRET-based distance between two freely rotating point dipoles is less than 6 \AA for $35 \text{ \AA} < R_{DA} < 80 \text{ \AA}$. The uncertainty is considerably reduced when multiple distances are calculated and self-consistency in distance networks is exploited⁹. Besides background contributions, an R_{DA} shorter than 30 \AA may lead to larger errors due to (i) potential dye–dye interactions and (ii) the dynamic averaging of the dipole orientations being reduced owing to an increased FRET rate.

Comparing distinct dye pairs. To validate the model assumption of a freely rotating and diffusing dye, we developed a self-consistency argument based on the relationship between different dye pairs that bypasses several experimental uncertainties. We define the ratio R_{rel} for two dye pairs as the ratio of their respective $R_{(E)}$ values (Methods, equation (30)). This ratio is quasi-independent of R_0 , because all dye parameters that are contained in R_0 are approximately eliminated by our DNA design. Therefore, these ratios should be similar for all investigated dye pairs, which we indeed found was the case (Supplementary Table 4). When comparing, for example, the low- to mid-distances for three dye pairs with $E > 0.1$, we obtained a mean R_{rel} of 1.34 and a maximum deviation of 2.7%. This is a relative error of 2.3%, which is less than the estimated error of our measured distances of 2.8% (Fig. 5a). This further demonstrates the validity of the assumptions for the dye model and averaging regime used here. This concept is discussed further in the Methods.

Although calculated model distances are based on a static model for the DNA structure, DNA is known not to be completely rigid³⁵. We tested our DNA model by carrying out molecular dynamics simulations using the DNA molecule (without attached dye molecules; Supplementary Note 7) and found that the averaged expected FRET efficiency obtained with the computed dynamically varying slightly bent DNA structure led to comparable but slightly longer distances

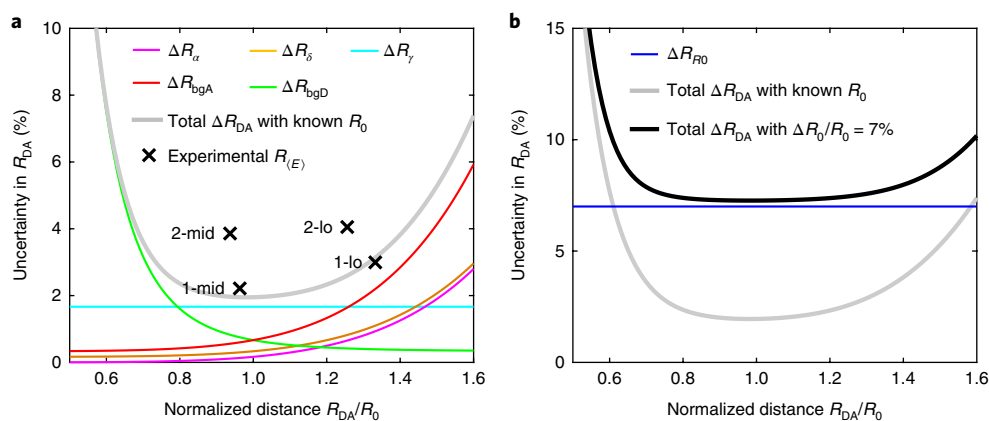


Fig. 5 | Error propagation of experimental uncertainty. **a**, R_{DA} uncertainty contributions from the experimental correction factors: ΔR_α (leakage), ΔR_δ (direct excitation), and ΔR_γ (gamma factor), ΔR_{bgD} and ΔR_{bgA} (background), ΔR_α (leakage), ΔR_δ (direct excitation), and total uncertainty with known R_0 ; crosses indicate the uncertainty of experimental values of $R_{(E)}$ across the labs. **b**, Uncertainty in R_{DA} (black line) based on the efficiency-related uncertainty (gray line) and the uncertainty for determining R_0 (blue line). Here we used the following uncertainties, which were determined for the confocal-based measurements on sample 1: $\Delta R_0/R_0 = 7\%$, $\Delta\gamma/\gamma = 10\%$, $\Delta I^{(BG)}/I = 2\%$, $\Delta\alpha/\alpha = 10\%$, and $\Delta\delta/\delta = 10\%$. Absolute values are presented in Supplementary Table 3.

than for the static model. The deviations between the models and data were reduced (Supplementary Table 4) for those cases where we observed larger deviations with static models.

Discussion

Despite differences in the setups used, the reported intensity-based FRET efficiencies were consistent between labs in this study. We attribute this remarkable consistency ($\Delta E \pm 0.05$) to the use of a general step-by-step procedure for the experiments and data analysis.

We also showed that the factors required for the correction of FRET efficiency can be determined with high precision, regardless of the setup type and acquisition software used. Together the measurement errors caused an uncertainty in R_{DA} of less than 5%, which agrees well with the variations between the different labs. Ultimately, we were interested in the absolute distances derived from these FRET efficiencies. Figure 5 shows that any distance between $0.6 R_0$ and $1.6 R_0$ could be determined with an uncertainty of less than $\pm 6 \text{ \AA}$. This fits well with the distance uncertainty measured across the labs and corresponds to a distance range from 35 to 80 \AA for the dye pairs used in sample 1. This estimation is valid if the dyes are sufficiently mobile, as has been supported by time-resolved anisotropy measurements and further confirmed by a self-consistency argument. The s.d. for sample 2 was slightly larger than that for sample 1 (Fig. 5a), which could be explained by specific photophysical properties. The values for samples 3 and 4 (Supplementary Table 4) showed similar precision, considering the smaller number of measurements.

For the samples 1-hi and 2-hi, which were measured after each lab verified its setup and procedure, the precision was further increased by almost a factor of two (Supplementary Table 4), possibly owing to the thorough characterization during this study.

We also tested the accuracy of the experimentally derived distances by comparing them with distances in the static model. For every single FRET pair we found excellent agreement between 0.1% and 4.1% (0.4–2.4 \AA) for sample 1 and agreement mostly within the range of experimental error between 3.1% and 9.0% (2.7–5.5 \AA) for sample 2. The deviations could be even smaller for dynamic DNA models. For sample 2, which had the cyanine-based dye Alexa Fluor 647 instead of the carbopyronine-based dye Atto 647N as an acceptor, the lower accuracy could be explained by imperfect sampling of the full AV or dye-specific photophysical properties (details are presented in Supplementary Table 2). It was shown previously that cyanine dyes are sensitive to their local environment³⁶ and therefore

require especially careful characterization for each newly labeled biomolecule.

For future work, it will be powerful to complement intensity-based smFRET studies with single-molecule lifetime studies, as the picosecond time resolution could provide additional information on calibration and fast dynamic biomolecular exchange. In addition, it will be important to establish appropriate dye models for more complex (protein) systems in which the local chemistry may affect dye mobility (Supplementary Note 4). However, when used with mobile dyes (which can be checked via anisotropy and lifetime experiments; Supplementary Note 2), the dye model here is fully generalizable to any biomolecular system^{8,9}.

The results from different labs and the successful self-consistency test clearly show the great potential of absolute smFRET-based distances for investigations of biomolecular conformations and dynamics, as well as for integrative structural modeling. The ability to accurately determine distances on the molecular scale with smFRET experiments and to estimate the uncertainty of the measurements provides the groundwork for smFRET-based structural and hybrid approaches. Together with the automated selection of the most informative pairwise labeling positions²³ and fast analysis procedures^{8–10}, we anticipate that smFRET-based structural methods will become an important tool for de novo structural determination and structure validation, especially for large and flexible structures with which the application of other structural biology methods is difficult.

Methods

Methods, including statements of data availability and any associated accession codes and references, are available at <https://doi.org/10.1038/s41592-018-0085-0>.

Received: 5 October 2017; Accepted: 25 May 2018;

Published online: 31 August 2018

References

- Förster, T. Zwischenmolekulare Energiewanderung und Fluoreszenz. *Ann. Phys.* **437**, 55–75 (1948).
- Stryer, L. & Haugland, R. P. Energy transfer: a spectroscopic ruler. *Proc. Natl Acad. Sci. USA* **58**, 719–726 (1967).
- Murchie, A. I. et al. Fluorescence energy transfer shows that the four-way DNA junction is a right-handed cross of antiparallel molecules. *Nature* **341**, 763–766 (1989).
- Mekler, V. et al. Structural organization of bacterial RNA polymerase holoenzyme and the RNA polymerase-promoter open complex. *Cell* **108**, 599–614 (2002).

5. Ha, T. et al. Probing the interaction between two single molecules: fluorescence resonance energy transfer between a single donor and a single acceptor. *Proc. Natl Acad. Sci. USA* **93**, 6264–6268 (1996).
6. Schuler, B., Lipman, E. A., Steinbach, P. J., Kumke, M. & Eaton, W. A. Polyproline and the “spectroscopic ruler” revisited with single-molecule fluorescence. *Proc. Natl Acad. Sci. USA* **102**, 2754–2759 (2005).
7. Choi, U. B. et al. Single-molecule FRET-derived model of the synaptotagmin 1-SNARE fusion complex. *Nat. Struct. Mol. Biol.* **17**, 318–384 (2010).
8. Kalinin, S. et al. A toolkit and benchmark study for FRET-restrained high-precision structural modeling. *Nat. Methods* **9**, 1218–1227 (2012).
9. Hellenkamp, B., Wortmann, P., Kandzia, F., Zacharias, M. & Hugel, T. Multidomain structure and correlated dynamics determined by self-consistent FRET Networks. *Nat. Methods* **14**, 174–180 (2017).
10. Eilert, T., Beckers, M., Drechsler, F. & Michaelis, J. Fast-NPS—a Markov chain Monte Carlo-based analysis tool to obtain structural information from single-molecule FRET measurements. *Comput. Phys. Commun.* **219**, 377–389 (2017).
11. Hofmann, D., Korzdorfer, T. & Kummel, S. Energy transfer and Förster's dipole coupling approximation investigated in a real-time Kohn-Sham scheme. *Phys. Rev. A* **82**, 012509 (2010).
12. Spiegel, J. D., Fulle, S., Kleinschmidt, M., Gohlke, H. & Marian, C. M. Failure of the IDA in FRET systems at close inter-dye distances is moderated by frequent low k^2 values. *J. Phys. Chem. B* **120**, 8845–8862 (2016).
13. Sakon, J. J. & Weninger, K. R. Detecting the conformation of individual proteins in live cells. *Nat. Methods* **7**, 203–205 (2010).
14. Sabanayagam, C. R., Eid, J. S. & Meller, A. Using fluorescence resonance energy transfer to measure distances along individual DNA molecules: corrections due to nonideal transfer. *J. Chem. Phys.* **122**, 61103–61107 (2005).
15. McCann, J. J., Choi, U. B., Zheng, L., Weninger, K. & Bowen, M. E. Optimizing methods to recover absolute FRET efficiency from immobilized single molecules. *Biophys. J.* **99**, 961–970 (2010).
16. Sisamakos, E., Valeri, A., Kalinin, S., Rothwell, P. J. & Seidel, C. A. M. Accurate single-molecule FRET studies using multiparameter fluorescence detection. *Methods Enzymol.* **475**, 455–514 (2010).
17. Lee, N. K. et al. Accurate FRET measurements within single diffusing biomolecules using alternating-laser excitation. *Biophys. J.* **88**, 2939–2953 (2005).
18. Kudryavtsev, V. et al. Combining MFD and PIE for accurate single-pair Förster resonance energy transfer measurements. *ChemPhysChem* **13**, 1060–1078 (2012).
19. Hohlbein, J., Craggs, T. D. & Cordes, T. Alternating-laser excitation: single-molecule FRET and beyond. *Chem. Soc. Rev.* **43**, 1156–1171 (2014).
20. Margeat, E. et al. Direct observation of abortive initiation and promoter escape within single immobilized transcription complexes. *Biophys. J.* **90**, 1419–1431 (2006).
21. Muschielok, A. et al. A nano-positioning system for macromolecular structural analysis. *Nat. Methods* **5**, 965–971 (2008).
22. Beckers, M., Drechsler, F., Eilert, T., Nagy, J. & Michaelis, J. Quantitative structural information from single-molecule FRET. *Faraday Discuss.* **184**, 117–129 (2015).
23. Dimura, M. et al. Quantitative FRET studies and integrative modeling unravel the structure and dynamics of biomolecular systems. *Curr. Opin. Struct. Biol.* **40**, 163–185 (2016).
24. Brunger, A. T., Strop, P., Vrljic, M., Chu, S. & Weninger, K. R. Three-dimensional molecular modeling with single molecule FRET. *J. Struct. Biol.* **173**, 497–505 (2011).
25. Craggs, T. D. et al. Substrate conformational dynamics drive structure-specific recognition of gapped DNA by DNA polymerase. *bioRxiv* Preprint at <https://www.biorxiv.org/content/early/2018/02/10/263038> (2018).
26. Nagy, J., Eilert, T. & Michaelis, J. Precision and accuracy in smFRET based structural studies—a benchmark study of the FAST-Nano-Positioning System. *J. Chem. Phys.* **148**, 123308 (2018).
27. Ivani, I. et al. Parmbsc1: a refined force field for DNA simulations. *Nat. Methods* **13**, 55–58 (2016).
28. Neubauer, H. et al. Orientational and dynamical heterogeneity of rhodamine 6G terminally attached to a DNA helix revealed by NMR and single-molecule fluorescence spectroscopy. *J. Am. Chem. Soc.* **129**, 12746–12755 (2007).
29. Iqbal, A. et al. Orientation dependence in fluorescent energy transfer between Cy3 and Cy5 terminally attached to double-stranded nucleic acids. *Proc. Natl Acad. Sci. USA* **105**, 11176–11181 (2008).
30. Peulen, T. O., Opanasyuk, O. & Seidel, C. A. M. Combining graphical and analytical methods with molecular simulations to analyze time-resolved FRET-measurements of labeled macromolecules accurately. *J. Phys. Chem. B* **121**, 8211–8241 (2017).
31. Digman, M. A., Caiola, V. R., Zamai, M. & Gratton, E. The Phasor approach to fluorescence lifetime imaging analysis. *Biophys. J.* **84**, L14–L16 (2008).
32. Kapanidis, A. N. et al. Fluorescence-aided molecule sorting: analysis of structure and interactions by alternating-laser excitation of single molecules. *Proc. Natl Acad. Sci. USA* **101**, 8936–8941 (2004).
33. Müller, B. K., Zaychikov, E., Bräuchle, C. & Lamb, D. C. Pulsed interleaved excitation. *Biophys. J.* **89**, 3508–3522 (2005).
34. Wozniak, A. K., Schröder, G. F., Grubmüller, H., Seidel, C. A. M. & Oesterhelt, F. Single-molecule FRET measures bends and kinks in DNA. *Proc. Natl Acad. Sci. USA* **105**, 18337–18342 (2008).
35. Stelzl, L. S., Erlenbach, N., Heinz, M., Prisner, T. F. & Hummer, G. Resolving the conformational dynamics of DNA with ångström resolution by pulsed electron-electron double resonance and molecular dynamics. *J. Am. Chem. Soc.* **139**, 11674–11677 (2017).
36. Levitus, M. & Ranjit, S. Cyanine dyes in biophysical research: the photophysics of polymethine fluorescent dyes in biomolecular environments. *Q. Rev. Biophys.* **44**, 123–151 (2011).

Acknowledgements

We thank the Eaton lab for early measurements that helped us design this study. We thank T. Peulen, M. Dimura, and R. McDonald for stimulating discussions on FRET measurements, data analysis, and modeling, and B. Bulat for measuring fluorescence quantum yields of Atto 550 and 1-mid (Atto 550). We also thank the company Atto-Tec for providing a reference sample of the dye Atto 550 for fluorescence characterization. The authors acknowledge networking support by the Dr. Wilhelm Heinrich und Else Heraeus Foundation and COST Action CM1306 “Understanding Movement and Mechanism in Molecular Machines.” The idea of a worldwide benchmark study of standard FRET rulers emerged at the 512th WE Heraeus Seminar “Single molecule kinetics” (Bad Honnef, Germany, 2012) and evolved further during the international COST symposium “Integrating spectroscopic and theoretical methods to analyse molecular machines” (Castle of Ringberg, Germany, 2014).

This work was supported by the European Research Council (ERC; grant agreement nos. 261227 (to A.N.K.), 646451 (to E.L.), 638536 (to T.C.), 671208 (to C.A.M.S.), and 681891 (to T. Hugel)), the Deutsche Forschungsgemeinschaft (DFG) (grant MI 749/4-1 to J.M., grant TI 329/10-1 to P.T., and grant SCHL 1896/3-1 to M.S.), the Swiss National Science Foundation (to B.S.), the German Federal Ministry of Education and Research (BMBF; 03ZZEN11 to M.S.), Research Foundation Flanders (FWO; grant G0B4915N to J. Hendrix), the Agency for Innovation by Science and Technology (IWT Flanders; doctoral scholarship to N.V.), the Danish Council for Independent Research (Sapere Aude grant 0602-01670B to V.B.), the Novo Nordisk Foundation (NNF15OC0017956 to V.B.), the UK BBSRC (grant BB/H01795X/1 to A.N.K.), the National Institute of Mental Health (grant MH081923 to M.E.B.), Clemson University (start-up funds to H. Sanabria, S.R.A., and I.S.Y.-O.), the NIH (grants GM109832 and GM118508 to K.R.W.; grant GM112659 to T. Ha), the NSF (Career Award MCS1749778 to H. Sanabria), the Carl-Zeiss-Stiftung (doctoral fellowship to E.K.), the Stipendienstiftung Rheinland-Pfalz (doctoral scholarship to G.K.), the Braunschweig International Graduate School of Metrology (B-IGSM; to B.W.), the DFG Research Training Group (GrK1952/1 “Metrology for Complex Nanosystems” to B.W.), the University of Sheffield (start-up funds to T.D.C.), and the National Research Foundation of Korea funded by the Ministry of Science and ICT (NRF-2017R1A2B3010309 to N.K.L.).

Author contributions

B. Hellenkamp, T. Hugel, J.M., and C.A.M.S. designed the research; B. Hellenkamp, S.S., O.D., O.O., R.K., S.R.A., B.A., M.A., A.B., H.C., T.E., C.F., C.G., G.G., P.H., C.A.H., A.H., J. Hendrix, L.L.H., V.H., J. Hohlbein, B. Hua, E.K., J.-Y.K., G.K., B.L., J.J.M., N.N.-R., D.N., T.N., R.Q., N.C.R., C.R., T.S., H.S., L.S., J.T., S.T., N.V., A.M.V., B.W., I.S.Y.-O., and T.D.C. performed measurements; B. Hellenkamp, S.S., and T. Hugel compared the measurements; all of the aforementioned authors and V.B., M.E.B., T.C., M.G., E.G., T. Ha, C.G.H., A.N.K., D.C.L., N.K.L., E.A.L., M.L., H. Sanabria, H. Seidel, M.S., B.S., P.T., K.R.W., J.M., and C.S. contributed to the analysis of the data and commented on the manuscript; B. Hellenkamp, S.S., T.D.C., J.M., C.A.M.S., and T. Hugel wrote the manuscript in consultation with O.D. and O.O.; and O.D. performed the calculations of the model distances.

Competing interests

The authors declare no competing interests.

Additional information

Supplementary information is available for this paper at <https://doi.org/10.1038/s41592-018-0085-0>.

Reprints and permissions information is available at www.nature.com/reprints.

Correspondence and requests for materials should be addressed to J.M. or C.A.M.S. or T.D.C. or T.H.

Publisher's note: Springer Nature remains neutral with regard to jurisdictional claims in published maps and institutional affiliations.

¹Institute of Physical Chemistry, University of Freiburg, Freiburg im Breisgau, Germany. ²Engineering and Applied Sciences, Columbia University, New York, NY, USA. ³Department of Bionanoscience, Kavli Institute of Nanoscience Delft, Delft University of Technology, Delft, the Netherlands. ⁴Molecular Physical Chemistry, Heinrich-Heine-Universität Düsseldorf, Düsseldorf, Germany. ⁵Department of Physics and Astronomy, Clemson University, Clemson, SC, USA. ⁶Department of Chemistry, University of Sheffield, Sheffield, UK. ⁷Interdisciplinary Nanoscience Center (iNANO) and Department of Chemistry, Aarhus University, Aarhus, Denmark. ⁸Physical Chemistry, Department of Chemistry, Nanosystems Initiative Munich (NIM), Center for Integrated Protein Science Munich (CiPSM) and Center for Nanoscience (CeNS), Ludwig-Maximilians-Universität München, Munich, Germany. ⁹Department of Physiology & Biophysics, Stony Brook University, Stony Brook, NY, USA. ¹⁰Department of Biomedical Engineering, University of California, Irvine, Irvine, CA, USA. ¹¹Molecular Microscopy Research Group, Zernike Institute for Advanced Materials, University of Groningen, Groningen, the Netherlands. ¹²Physical and Synthetic Biology, Faculty of Biology, Ludwig-Maximilians-Universität München, Planegg-Martinsried, Germany. ¹³Institute for Biophysics, Ulm University, Ulm, Germany. ¹⁴Laboratory of Biophysics, Wageningen University & Research, Wageningen, the Netherlands. ¹⁵Department of Biomedical Engineering, Johns Hopkins University, Baltimore, MD, USA. ¹⁶Department of Physics, North Carolina State University, Raleigh, NC, USA. ¹⁷B CUBE—Center for Molecular Bioengineering, TU Dresden, Dresden, Germany. ¹⁸Laboratory for Photochemistry and Spectroscopy, Department of Chemistry, University of Leuven, Leuven, Belgium. ¹⁹Dynamic Bioimaging Lab, Advanced Optical Microscopy Center and Biomedical Research Institute, Hasselt University, Hasselt, Belgium. ²⁰Institute of Physics, University of Lübeck, Lübeck, Germany. ²¹Microspectroscopy Research Facility Wageningen, Wageningen University & Research, Wageningen, the Netherlands. ²²Gene Machines Group, Clarendon Laboratory, Department of Physics, University of Oxford, Oxford, UK. ²³School of Chemistry, Seoul National University, Seoul, South Korea. ²⁴Molecular Biophysics, Technische Universität Kaiserslautern (TUK), Kaiserslautern, Germany. ²⁵Departments of Biology and Chemistry, Pharmacy and Geosciences, Johannes Gutenberg-University Mainz, Mainz, Germany. ²⁶Institute of Molecular Biology (IMB), Mainz, Germany. ²⁷Structural and Computational Biology Unit, European Molecular Biology Laboratory (EMBL), Heidelberg, Germany. ²⁸School of Molecular Sciences and The Biodesign Institute, Arizona State University, Tempe, AZ, USA. ²⁹Department of Biochemistry, University of Zurich, Zurich, Switzerland. ³⁰Department of Chemistry, Ludwig-Maximilians-Universität München, München, Germany. ³¹Institute of Physical & Theoretical Chemistry, Braunschweig Integrated Centre of Systems Biology (BRICS), and Laboratory for Emerging Nanometrology (LENA), Braunschweig University of Technology, Braunschweig, Germany. ³²BIOS Centre for Biological Signalling Studies, University of Freiburg, Freiburg im Breisgau, Germany. ³³These authors contributed equally: Björn Hellenkamp, Sonja Schmid. *e-mail: jens.michaelis@uni-ulm.de; cseidel@hhu.de; t.craggs@sheffield.ac.uk; thorsten.hugel@pc.uni-freiburg.de

Methods

Nomenclature and definitions. See Supplementary Table 5 for a summary of the following section.

The FRET efficiency E is defined as

$$E = \frac{F_{A|D}}{F_{D|D} + F_{A|D}} \quad (1)$$

where F is the signal. The stoichiometry S is defined as

$$S = \frac{F_{D|D} + F_{A|D}}{F_{D|D} + F_{A|D} + F_{A|A}} \quad (2)$$

The FRET efficiency for a single donor–acceptor distance R_{DA} is defined as

$$E = \frac{1}{1 + R_{DA}^6/R_0^6} \quad (3)$$

The mean FRET efficiency for a discrete distribution of donor–acceptor distances with the position vectors $\mathbf{R}_{D(i)}$ and $\mathbf{R}_{A(j)}$ is calculated as

$$\langle E \rangle = \frac{1}{nm} \sum_{i=1}^n \sum_{j=1}^m \frac{1}{1 + |\mathbf{R}_{A(j)} - \mathbf{R}_{D(i)}|^6/R_0^6} \quad (4)$$

The apparent donor–acceptor distance $R_{(E)}$ is computed from the average FRET efficiency for a distance distribution. It is a FRET-averaged quantity that is also referred to as the FRET-averaged distance $\langle R_{DA} \rangle_E$ (ref. 37):

$$R_{(E)} \equiv R(E) = R_0(E^{-1} - 1)^{1/6} \quad (5)$$

The distance between the mean dye positions with the position vectors $\mathbf{R}_{D(i)}$ and $\mathbf{R}_{A(j)}$ is obtained by normalization of sums over all positions within the respective AVs:

$$R_{MP} = |\langle \mathbf{R}_{D(i)} \rangle - \langle \mathbf{R}_{A(j)} \rangle| = \left| \frac{1}{n} \sum_{i=1}^n \mathbf{R}_{D(i)} - \frac{1}{m} \sum_{j=1}^m \mathbf{R}_{A(j)} \right| \quad (6)$$

Definitions of abbreviations in subscripts and superscripts are as follows:

- D or A: donor or acceptor
- A|D: acceptor fluorescence upon donor excitation (similarly for D|D, A|A, etc.)
- Aem|Dex: intensity in the acceptor channel upon donor excitation (similarly for Dem|Dex, Aem|Aex, etc.)
- app: apparent, that is, including systematic, experimental offsets
- BG: background
- DO/AO: donor-only/acceptor-only species
- DA: FRET species
- i–iii: (i) the uncorrected intensity; (ii) intensity after BG correction; (iii) intensity after BG, α , and δ corrections

The four correction factors are defined as follows.

Leakage of donor fluorescence into the acceptor channel:

$$\alpha = \frac{g_{R|D}}{g_{G|D}} = \frac{\langle i i_{app}^{(DO)} \rangle}{1 - \langle i i_{app}^{(DO)} \rangle}$$

Normalization of excitation intensities I and cross-sections σ of the acceptor and donor:

$$\beta = \frac{\sigma_{A|R} I_{Aex}}{\sigma_{D|G} I_{Dex}}$$

Normalization of effective fluorescence quantum yields, $^{eff}\Phi_F = a_b \Phi_F$, and detection efficiencies g of the acceptor and donor, where a_b is the fraction of molecules in the bright state and Φ_F is the fluorescence quantum yield without photophysical (saturation) effects:

$$\gamma = \frac{g_{R|A} \text{ } ^{eff}\Phi_{F,A}}{g_{G|D} \text{ } ^{eff}\Phi_{F,D}}$$

Direct acceptor excitation by the donor excitation laser (lower wavelength):

$$\delta = \frac{\sigma_{A|G} I_{Dex}}{\sigma_{A|R} I_{Aex}} = \frac{\langle i i_{app}^{(AO)} \rangle}{1 - \langle i i_{app}^{(AO)} \rangle}$$

where I is the experimentally observed intensity; F indicates the corrected fluorescence intensity; $\Phi_{F,A}$ and $\Phi_{F,D}$ are the fluorescence quantum yield of the acceptor and the donor, respectively; $g_{R|A}$ and $g_{G|D}$ represent the detection efficiency of the red detector (R) if only the acceptor was excited or green detector (G) if the donor was excited (analogously for other combinations); and $\sigma_{A|G}$ is the excitation

cross-section for the acceptor when excited with green laser (analogously for the other combinations).

The Förster radius (in angstroms) for a given J in the units shown below is given by

$$\frac{R_0}{\text{\AA}} = 0.2108 \sqrt[6]{\left(\frac{\Phi_{F,D} \kappa^2}{n_{im}^4} \right) \frac{J}{M^{-1} \text{cm}^{-1} \text{nm}^4}} \quad (7)$$

with the dipole orientation factor $\kappa^2 = (\cos \theta_{AD} - 3 \cos \theta_D \cos \theta_A)^2$ and the spectral overlap integral (in $\text{cm}^{-1} \text{M}^{-1} \text{nm}^4$)

$$J = \int_0^\infty \overline{F}_D(\lambda) \varepsilon_A(\lambda) \lambda^4 d\lambda$$

with the normalized spectral radiant intensity of the excited donor (in nm^{-1}), defined as the emission intensity F per unit wavelength,

$$\overline{F}_D(\lambda) \text{ with } \int_0^\infty \overline{F}_D(\lambda) d\lambda = 1$$

and the extinction coefficient of the acceptor (in $\text{M}^{-1} \text{cm}^{-1}$), $\varepsilon_A(\lambda)$, and the refractive index of the medium between the dyes, n_{im} .

Samples. Altogether, eight different FRET samples were designed with the acceptor dyes positioned 15 or 23 bp away from the donor dyes. The exact sequences and dye positions are given in Supplementary Table 1 and Supplementary Note 1. We ordered them from IBA GmbH (Göttingen), which synthesized and labeled the single DNA strands and then carried out HPLC purification. Here the dyes were attached to a thymidine (dT), which is known to cause the least fluorescence quenching of all nucleotides²⁶.

Most labs measured the four DNA samples listed in Supplementary Table 1. Therefore, we focus on these four samples in the main text of this paper. The additional samples and the corresponding measurements are described in Supplementary Note 1, Supplementary Fig. 2, and Supplementary Table 4. A buffer consisting of 20 mM MgCl₂, 5 mM NaCl, 5 mM Tris, pH 7.5, was requested for all measurements, with de-gassing just before the measurement at room temperature.

The linker lengths were chosen in such a way that all dyes had about the same number of flexible bonds between the dipole axis and the DNA. Atto 550, Alexa Fluor 647, and Atto 647N already have an intrinsic flexible part before the C-linker starts (Supplementary Fig. 1). In addition, the DNAs were designed such that the distance ratio between the high-FRET-efficiency and low-FRET-efficiency samples should be the same for all samples, largely independent of R_0 .

Details on all used setups and analysis software are presented in Supplementary Note 8.

General correction procedure. The FRET efficiency E and stoichiometry S are defined in equations (1) and (3). Determination of the corrected FRET E and S is based largely on the approach of Lee et al.¹⁷ and consists of the following steps: (1) data acquisition, (2) generation of uncorrected 2D histograms for E versus S , (3) background subtraction, (4) correction for position-specific excitation in TIRF experiments, (5) correction for leakage and direct acceptor excitation, and (6) correction for excitation intensities and absorption cross-sections, quantum yields, and detection efficiencies.

Data acquisition. The sample with both dyes is measured, and three intensity time traces are extracted: acceptor emission upon donor excitation ($I_{Aem|Dex}$), donor emission upon donor excitation ($I_{Dem|Dex}$), and acceptor emission upon acceptor excitation ($I_{Aem|Aex}$).

For the confocal setups, a straightforward burst identification is carried out in which the trace is separated into 1-ms bins. Usually a minimum threshold (e.g., 50 photons) is applied to the sum of the donor and acceptor signals after donor excitation for each bin. This threshold is used again in every step, such that the number of bursts used may change from step to step (if the γ correction factor is not equal to 1). Some labs use sophisticated burst-search algorithms. For example, the dual-channel burst search^{38,39} recognizes the potential bleaching of each dye within bursts. Note that the choice of burst-search algorithm can influence the γ correction factor. For standard applications, the simple binning method is often sufficient, especially for well-characterized dyes and low laser powers. This study shows that the results do not depend heavily on these conditions (if they are applied properly), as every lab used its own setup and procedure at this stage. The number of photon bursts per measurement was typically between 1,000 and 10,000.

For the TIRF setups, traces with one acceptor and one donor are selected, defined by a bleaching step. In addition, only the relevant range of each trajectory (i.e., prior to photobleaching of either dye) is included in all subsequent steps. The mean length of the time traces analyzed by the reference lab was 47 frames (18.8 s) for the 185 traces of sample 1-lo and 15 frames (6 s) for the 124 traces of sample 2-lo measured at an ALEX sampling rate of 2.5 Hz. For sample 1, bleaching was

donor limited, whereas bleaching for sample 2 was acceptor limited, which explains the significant difference in frame lengths. For details on the analysis from the reference lab, see ref. ⁴⁰.

2D histogram. A 2D histogram (Fig. 2a,e) of the apparent (uncorrected) stoichiometry, ${}^iS_{\text{app}}$, versus the apparent FRET efficiency, ${}^iE_{\text{app}}$, defined by equations (8) and (9), is generated, where

$${}^iS_{\text{app}} = \frac{I_{\text{Aem|Dex}} + I_{\text{Dem|Dex}}}{I_{\text{Aem|Dex}} + I_{\text{Dem|Dex}} + I_{\text{Aem|Aex}}} \quad (8)$$

$${}^iE_{\text{app}} = \frac{I_{\text{Aem|Dex}}}{I_{\text{Aem|Dex}} + I_{\text{Dem|Dex}}} \quad (9)$$

Background correction. Background $I^{(\text{BG})}$ is removed from each uncorrected intensity I separately, thus leading to the background-corrected intensities ${}^{ii}I$, ${}^{ii}S_{\text{app}}$, and ${}^{ii}E_{\text{app}}$:

$$\begin{aligned} {}^{ii}I_{\text{Dem|Dex}} &= I_{\text{Dem|Dex}} - I_{\text{Dem|Dex}}^{(\text{BG})} \\ {}^{ii}I_{\text{Aem|Aex}} &= I_{\text{Aem|Aex}} - I_{\text{Aem|Aex}}^{(\text{BG})} \\ {}^{ii}I_{\text{Aem|Dex}} &= I_{\text{Aem|Dex}} - I_{\text{Aem|Dex}}^{(\text{BG})} \end{aligned} \quad (10)$$

For confocal measurements, one can determine the background by averaging the photon count rate for all time bins that are below a certain threshold, which is defined, for example, by the maximum in the frequency-versus-intensity plot (the density of bursts should not be too high). Note that a previous measurement of only the buffer can uncover potential fluorescent contaminants, but may differ substantially from the background of the actual measurement. The background intensity is then subtracted from the intensity of each burst in each channel (equation (10)). Typical background values are 0.5–1 photon/ms (Fig. 2b).

For TIRF measurements, various trace-wise or global background corrections can be applied. The most common method defines background as the individual offset (time average) after photobleaching of both dyes in each trace. Other possibilities include selecting the darkest spots in the illuminated area and subtracting an average background time trace from the data, or using a local background, for example, with a mask around the particle. The latter two options have the advantage that possible (exponential) background bleaching is also corrected. We did not investigate the influence of the kind of background correction during this study, but a recent study showed that not all background estimators are suitable for samples with a high molecule surface coverage⁴¹.

To summarize, a correction of the background is very important but can be done very well in different ways.

Position-specific excitation correction (optional for TIRF). The concurrent excitation profiles of both lasers are key for accurate measurements (Supplementary Fig. 5). Experimental variations across the field of view are accounted for by a position-specific normalization:

$${}^{(\text{profile})}{}^{ii}I_{\text{Aem|Aex}} = {}^{ii}I_{\text{Aem|Aex}} \frac{I_{\text{D}}(x', y')}{I_{\text{A}}(x, y)} \quad (11)$$

where $I_{\text{D}}(x', y')$ and $I_{\text{A}}(x, y)$ denote the excitation intensities at corresponding positions in the donor or acceptor image, respectively. Individual excitation profiles are determined as the mean image of a stack of images recorded across a sample chamber with dense dye coverage.

Leakage (α) and direct excitation (δ). After the background correction, the leakage fraction of the donor emission into the acceptor detection channel and the fraction of the direct excitation of the acceptor by the donor-excitation laser are determined. The correction factor for leakage (α) is determined by equation (12), using the FRET efficiency of the donor-only population (“D only” in Fig. 2b,f). The correction factor for direct excitation (β) is determined by equation (13) from the stoichiometry of the acceptor-only population (“A only” in Fig. 2b,f).

$$\alpha = \frac{\langle {}^{ii}E_{\text{app}}^{(\text{DO})} \rangle}{1 - \langle {}^{ii}E_{\text{app}}^{(\text{DO})} \rangle} \quad (12)$$

$$\delta = \frac{\langle {}^{ii}S_{\text{app}}^{(\text{AO})} \rangle}{1 - \langle {}^{ii}S_{\text{app}}^{(\text{AO})} \rangle} \quad (13)$$

where ${}^{ii}E_{\text{app}}^{(\text{DO})}$ and ${}^{ii}S_{\text{app}}^{(\text{AO})}$ are calculated from the background-corrected intensities ${}^{ii}I$ of the corresponding population, donor-only or acceptor-only, respectively. This correction, together with the previous background correction, results in the

donor-only population being located at $E = 0, S = 1$ and the acceptor-only population at $S = 0, E = 0 \dots 1$. The corrected acceptor fluorescence after donor excitation, $F_{\text{A|D}}$, is given by equation (14), which yields the updated expressions for the FRET efficiency and stoichiometry, equations (15) and (16), respectively.

$$F_{\text{A|D}} = {}^{ii}I_{\text{Aem|Dex}} - \alpha {}^{ii}I_{\text{Dem|Dex}} - \delta {}^{ii}I_{\text{Aem|Aex}} \quad (14)$$

$${}^{iii}E_{\text{app}} = \frac{F_{\text{A|D}}}{F_{\text{A|D}} + {}^{ii}I_{\text{Dem|Dex}}} \quad (15)$$

$${}^{iii}S_{\text{app}} = \frac{F_{\text{A|D}} + {}^{ii}I_{\text{Dem|Dex}}}{F_{\text{A|D}} + {}^{ii}I_{\text{Dem|Dex}} + {}^{ii}I_{\text{Aem|Aex}}} \quad (16)$$

In principle, the leaked donor signal could be added back to the donor emission channel⁴². However, this would require precise knowledge about spectral detection efficiencies, which is not otherwise required, and has no effect on the final accuracy of the measurement. As the determination of α and δ influences the γ and β correction in the next step, both correction steps can be repeated in an iterative manner if required (e.g., if the γ and β factors deviate largely from 1).

γ and β correction factors. Differences in the excitation intensities and cross-section, as well as quantum yields and detection efficiencies, are accounted for by use of the correction factors γ and β , respectively. If the fluorescence quantum yields do not depend on efficiencies or if such dependence is negligible (homogeneous approximation), mean values of efficiencies $\langle {}^{iii}E_{\text{app}}^{(\text{DA})} \rangle$ and of stoichiometries $\langle {}^{iii}S_{\text{app}}^{(\text{DA})} \rangle$ are related by equation (17):

$${}^{iii}S_{\text{app}}^{(\text{DA})} = (1 + \gamma\beta + (1 - \gamma)\beta) \langle {}^{iii}E_{\text{app}}^{(\text{DA})} \rangle^{-1} \quad (17)$$

So, in the homogeneous approximation, γ and β correction factors can be determined by fitting of FRET populations to the histogram of ${}^{iii}S_{\text{app}}^{(\text{DA})}$ versus ${}^{iii}E_{\text{app}}^{(\text{DA})}$ with the line defined by equation (17). As this method relies on the analysis of ${}^{iii}S_{\text{app}}^{(\text{DA})}$ and ${}^{iii}E_{\text{app}}^{(\text{DA})}$ values obtained from multiple species, we term this method global γ -correction. Such a fit can be performed for all FRET populations together, for any of their subsets, and, in principle, for each single-species population separately (see below). Alternatively, a linear fit of inverse $\langle {}^{iii}S_{\text{app}}^{(\text{DA})} \rangle$ versus $\langle {}^{iii}E_{\text{app}}^{(\text{DA})} \rangle$ with y -intercept a and slope b can be performed.

In this case, $\beta = a + b - 1$ and $\gamma = (a - 1) / (a + b - 1)$.

Error propagation, however, is more straightforward if equation (17) is used. If there is a complex dependence between properties of dyes and efficiencies, the homogeneous approximation is no longer applicable. In this case, the relationship between ${}^{iii}S_{\text{app}}^{(\text{DA})}$ and ${}^{iii}E_{\text{app}}^{(\text{DA})}$ for different populations (or even subpopulations for the same single species) cannot be described by equation (17) with a single γ correction factor. Here, γ can be determined for a single species. We call this ‘single-species γ -correction’. This works only if the efficiency broadening is dominated by distance fluctuations. The reason for this assumption is the dependency of these correction factors on both the stoichiometry and the distance-dependent efficiency. In our study, global and local γ -correction yielded similar results. Therefore, the homogeneous approximation, with distance fluctuations as the main cause for efficiency broadening, can be assumed for samples 1 and 2. Systematic variation of the γ correction factor yields an error of about 10%.

Alternatively, determination of γ and β factors can be done trace-wise, as in, for example, msALEX experiments⁴³, where the γ factor is determined as the ratio of the decrease in acceptor signal and the increase in donor signal after acceptor bleaching. We call such an alternative correction individual γ -correction¹⁵. The analysis of local distributions can provide valuable insights about properties of the studied system.

After γ and β correction, the corrected donor (acceptor) fluorescence after donor (acceptor) excitation $F_{\text{D|D}}$ ($F_{\text{A|A}}$) amounts to

$$F_{\text{D|D}} = \gamma {}^{ii}I_{\text{Dem|Dex}} \quad (18)$$

$$F_{\text{A|A}} = \frac{1}{\beta} {}^{ii}I_{\text{Aem|Aex}} \quad (19)$$

Fully corrected values. Application of all corrections leads to the estimates of real FRET efficiencies E and stoichiometries S from the background-corrected intensities ${}^{ii}I$. The explicit expressions of fully corrected FRET efficiency and stoichiometry are

$$E = \frac{[{}^{ii}I_{\text{Aem|Dex}} - \alpha {}^{ii}I_{\text{Dem|Dex}} - \delta {}^{ii}I_{\text{Aem|Aex}}]}{\gamma [{}^{ii}I_{\text{Dem|Dex}}] + [{}^{ii}I_{\text{Aem|Dex}} - \alpha {}^{ii}I_{\text{Dem|Dex}} - \delta {}^{ii}I_{\text{Aem|Aex}}]} \quad (20)$$

$$S = \frac{\gamma [{}^{ii}I_{\text{Dem|Dex}}] + [{}^{ii}I_{\text{Aem|Dex}} - \alpha {}^{ii}I_{\text{Dem|Dex}} - \delta {}^{ii}I_{\text{Aem|Aex}}]}{\gamma [{}^{ii}I_{\text{Dem|Dex}}] + [{}^{ii}I_{\text{Aem|Dex}} - \alpha {}^{ii}I_{\text{Dem|Dex}} - \delta {}^{ii}I_{\text{Aem|Aex}}] + 1/\beta [{}^{ii}I_{\text{Aem|Aex}}]} \quad (21)$$

Plots of the E -versus- S histogram are shown in Fig. 2d,h. Now, the FRET population should be symmetric to the line for $S=0.5$. The donor-only population should still be located at $E=0$, and the acceptor-only population should be at $S=0$. Finally, the corrected FRET efficiency histogram is generated from events with a stoichiometry of $0.3 < S < 0.7$ (histograms in Fig. 2). The expected value of the corrected FRET efficiencies E is deduced as the center of a Gaussian fit to the efficiency histogram. This is a good approximation for FRET efficiencies in the range from about 0.1 to 0.9. In theory, the shot-noise limited efficiencies follow a binomial distribution if the photon number per burst is constant. For extreme efficiencies or data with a small average number of photons per burst, the efficiency distribution can no longer be approximated with a Gaussian. In this case and also in the case of efficiency broadening due to distance fluctuations, a detailed analysis of the photon statistics can be useful^{38,44–46}.

Uncertainty in distance due to R_0 . According to Förster theory¹, the FRET efficiency E and the distance R are related by equation (3). In this study, we focused on the comparison of E values across different labs in a blind study. Many excellent reviews have been published on how to determine the Förster radius R_0 ^{16,47,48}, and a complete discussion would be beyond the scope of the current study. In the following, we estimate and discuss the different sources of uncertainty in R_0 by utilizing standard error propagation (see also Supplementary Note 6 and ref. ²⁶). R_0 is given by equation (7).

The 6th power of the Förster radius is proportional to the relative dipole orientation factor κ^2 , the donor quantum yield $\Phi_{F,D}$, the overlap integral J , and n^{-4} , where n is the refractive index of the medium:

$$R_0^6 \sim \kappa^2 \cdot \Phi_{F,D} \cdot J \cdot n^{-4} \quad (22)$$

For Fig. 5b, we used a total Förster radius related distance uncertainty of 7%, which is justified by the following estimate. Please note that the error in the dipole orientation factor is always specific for the investigated system, whereas the errors in the donor quantum yield, overlap integral and refractive index are more general, although their mean values do also depend on the environment.

The refractive index. Different values for the refractive index in FRET systems have been used historically, but ideally the refractive index of the donor–acceptor intervening medium n_{im} should be used. Some experimental studies suggest that the use of the refractive index of the solvent may be appropriate, but this is still open for discussion (see, e.g., the discussion in ref. ⁴⁹).

$$R_0^6(n) \sim n_{im}^{-4} \quad (23)$$

In the worst case, this value n_{im} might be anywhere between the refractive index of the solvent ($n_{water} = 1.33$) and a refractive index for the dissolved molecule ($n < n_{oil} = 1.52$) (ref. ⁵⁰), that is, $n_{water} < n_{im} < n_{oil}$. This would result in a maximum uncertainty of $\Delta n_{im} < 0.085$. As recommended by Clegg⁵¹, we used $n_{im} = 1.40$ to minimize this uncertainty (Supplementary Table 6). The distance uncertainty propagated from the uncertainty of the refractive indices can then be assumed to be

$$\Delta R_0(n) \approx \frac{4}{6} R_0 \frac{\Delta n_{im}}{n} < 0.04 \cdot R_0 \quad (24)$$

The donor quantum yield Φ_{FD} is position dependent; therefore we measured the fluorescence lifetimes and quantum yields of the free dye Atto 550 and the 1-hi, 1-mid, and 1-lo donor-only labeled samples (Supplementary Table 2).

In agreement with the work of Sindbert et al.³⁷, the uncertainty of the quantum yield is estimated at $\Delta \Phi_{FD} = 5\%$, arising from the uncertainties of the Φ_F values of reference dyes and the precision of the absorption and fluorescence measurements. Thus, the distance uncertainty due to the quantum yield is estimated as

$$\Delta R_0(\Phi_{F,D}) \approx \frac{R_0}{6} \frac{\Delta \Phi_{F,D}}{\Phi_{F,D}} = 0.01 \cdot R_0 \quad (25)$$

The overlap integral J was measured for the unbound dyes in solution (Atto 550 and Atto 647N), as well as for samples 1-lo and 1-mid. This resulted in a deviation of about 10% for J when we used the literature values for the extinction coefficients. All single-stranded labeled DNA samples used in this study were purified with HPLC columns providing a labeling efficiency of at least 95%. The labeling efficiencies of the single-stranded singly labeled DNA and of the double-stranded singly labeled DNA samples were determined by the ratio of the absorption maxima of the dye and the DNA and were all above 97%. This indicates an error of the assumed extinction coefficient of less than 3%. Thus, the distance uncertainty due to the overlap spectra and a correct absolute acceptor extinction coefficient can be estimated by equation (26). However,

the uncertainty in the acceptor extinction coefficient might be larger for other environments, such as when bound to a protein.

$$\Delta R_0(J) \approx \frac{R_0}{6} \frac{\Delta J}{J} = 0.025 \cdot R_0 \quad (26)$$

In addition to the above uncertainty estimation, the J -related uncertainty can also be obtained through verification of the self-consistency of a β -factor network⁹. Finally, we found little uncertainty when we used the well-tested dye Atto 647N. Fluorescence spectra were measured on a Fluoromax4 spectrafluorimeter (Horiba, Germany). Absorbance spectra were recorded on a Cary5000 UV-VIS spectrometer (Agilent, USA) (Supplementary Fig. 6).

The κ^2 factor and model assumptions. The uncertainty in the distance depends on the dye model used²². Several factors need to be considered, given the model assumptions of unrestricted dye rotation, equal sampling of the entire accessible volume, and the rate inequality $k_{rot} \gg k_{FRET} \gg k_{diff} \gg k_{int}$.

First, the use of $\kappa^2 = 2/3$ is justified if $k_{rot} \gg k_{FRET}$, because then there is rotational averaging of the dipole orientation during energy transfer. k_{rot} is determined from the rotational correlation time $\rho_1 < 1$ ns, and k_{FRET} is determined from the fluorescence lifetimes $1 \text{ ns} < \tau_{fl} < 5$ ns. Hence the condition $k_{rot} \gg k_{FRET}$ is not strictly fulfilled. We estimate the error this introduces into κ^2 from the time-resolved anisotropies of donor and acceptor dyes. If the transfer rate is smaller than the fast component of the anisotropy decay (rotational correlation time) of donor and acceptor, then the combined anisotropy, r_C , is given by the residual donor and acceptor anisotropies ($r_{D,\infty}$ and $r_{A,\infty}$, respectively):

$$r_C = \sqrt{r_{A,\infty}^2 + r_{D,\infty}^2} \quad (27)$$

In theory, the donor and the acceptor anisotropy should be determined at the time of energy transfer. If the transfer rate is much slower than the fast component of the anisotropy decay of donor and acceptor, the residual anisotropy can be used (Supplementary Fig. 7)⁹. Also, the steady-state anisotropy values can give an indication of the rotational freedom of the dyes on the relevant time scales, if the inherent effect by the fluorescence lifetimes is taken into account (refer to the Perrin equation, $r(\tau) = r_0 / (1 + (\tau/\phi))$), where r is the observed anisotropy, r_0 is the intrinsic anisotropy of the molecule, τ is the fluorescence lifetime, and ϕ is the rotational time constant; Supplementary Table 2 and Supplementary Fig. 8).

If the steady-state anisotropy and r_C are low (< 0.2), one can assume (but not prove) sufficient isotropic coupling (rotational averaging), that is, $\kappa^2 = 2/3$, with an uncertainty of about 5% (ref. ⁵²):

$$\Delta R_0(\kappa^2, r_C < 0.2) \approx 0.05 \cdot R_0 \quad (28)$$

Spatial sampling. In addition, it is assumed that both dyes remain in a fixed location for the duration of the donor lifetime, that is, $k_{FRET} \gg k_{diff}$, where k_{diff} is defined as the inverse of the diffusion time through the complete AV. Recently the diffusion coefficient for a tethered Alexa Fluor 488 dye was determined to be $D = 10 \text{ \AA}^2/\text{ns}$ (ref. ³⁰). Therefore, k_{diff} is smaller than k_{FRET} . For short distances ($< 5 \text{ \AA}$) the rates become similar, but the effect on the inter-dye distance distribution within the donor's lifetime is small, as has been observed in time-resolved experiments. We also assumed that, in the experiment, the efficiencies are averaged over all possible inter-dye positions. This is the case when $k_{diff} \gg k_{int}$, which is a very good assumption for TIRF experiments with $k_{int} > 100$ ms, and also for confocal experiments with k_{int} values around 1 ms.

Overall uncertainty in R_0 . Time-resolved anisotropy measurements of samples 1 and 2 resulted in combined anisotropies less than 0.1. Therefore, we assumed isotropic coupling to obtain R_{MP} . The R_{MP} values matched the model distances very well, further supporting these assumptions. Finally, an experimental study of κ^2 distributions also yielded typical errors of 5% (ref. ³⁷).

The overall uncertainty for the Förster radius would then result in

$$\Delta R_0(n^{-4}, \Phi_{F,D}, J, \kappa^2) = \sqrt{\Delta R_0(n)^2 + \Delta R_0(\Phi_{F,D})^2 + \Delta R_0(J)^2 + \Delta R_0(\kappa^2)^2} \lesssim 0.07 \cdot R_0 \quad (29)$$

The absolute values determined for this study are summarized in Supplementary Table 6. Please note that the photophysical properties of dyes vary in different buffers and when the dyes are attached to different biomolecules. Therefore, all four quantities that contribute to the uncertainty in R_0 should be measured for the system under investigation. When supplier values or values from other studies are applied, the uncertainty can be much larger. The values specified here could be further evaluated and tested in another blind study.

Comparing distinct dye pairs. Even though time-resolved fluorescence anisotropy can show whether dye rotation is fast, the possibility of dyes interacting with the DNA cannot be fully excluded. Thus, it is not clear whether the dye molecule is completely free to sample the computed AV (free diffusion), or whether there are sites of attraction (preferred regions) or sites of repulsion (disallowed regions). To validate the model assumption of a freely rotating and diffusing dye, we define the

ratio R_{rel} for two apparent distances measured with the same dye pair (e.g., when comparing the low- to the mid-distance):

$$\begin{aligned}
 R_{\text{rel}} &= \frac{R_{(E),\text{lo}}}{R_{(E),\text{mid}}} \\
 &= \frac{R_{0,\text{lo}}}{R_{0,\text{mid}}} \sqrt[6]{\frac{1/E_{\text{lo}}-1}{1/E_{\text{mid}}-1}} \\
 &= \sqrt[6]{\frac{\kappa_{\text{lo}}^2 \Phi_{\text{D,lo}} I_{\text{lo}} n_{\text{lo}}^4}{\kappa_{\text{mid}}^2 \Phi_{\text{D,mid}} I_{\text{mid}} n_{\text{lo}}^4}} \sqrt[6]{\frac{1/E_{\text{lo}}-1}{1/E_{\text{mid}}-1}} \\
 &= f \cdot \sqrt[6]{\frac{1/E_{\text{lo}}-1}{1/E_{\text{mid}}-1}}
 \end{aligned} \tag{30}$$

For comparison of the other apparent distances, the ratio is adapted accordingly. Computed values relative to the mid-distance are shown in Supplementary Table 4. Note that R_{rel} values are (quasi) independent of R_0 for the following reasons: first, the donor positions in the lo, mid, and hi constructs are kept constant between samples 1, 2, 3 and 4, respectively. Therefore, the following assumptions can be made: (i) the ratios of the donor quantum yields are identical; (ii) the ratios of the spectral overlaps J for the lo, mid, and hi samples of one and the same dye pair should be the same; (iii) for a given geometry (Fig. 1) the refractive indices n_{m} of the medium between the dyes should also be very similar; and (iv) the ratios of the orientation factors κ^2 should be nearly equal, as the measured donor anisotropies are low for the lo, mid, and hi positions. Second, the acceptor extinction coefficients cancel each other out, as the acceptor is at the same position for the lo, mid, and hi constructs within a sample. Thus, the different dye pairs and the model used in this study should all give similar values for R_{rel} . Therefore, we compared the R_{rel} values for different dye pairs to determine whether for a particular dye pair the model assumptions are in agreement with the experimental data. Given our relative error in the determined distance of at most 2.8% (Fig. 5a), this is actually the case for all dye pairs investigated.

Reporting Summary. Further information on research design is available in the Nature Research Reporting Summary linked to this article.

Code availability. All custom code used herein is available from the authors upon reasonable request.

Data availability. All data are available from the corresponding authors upon reasonable request. The raw data for Fig. 2 are available at Zenodo (<https://doi.org/10.5281/zenodo.1249497>).

References

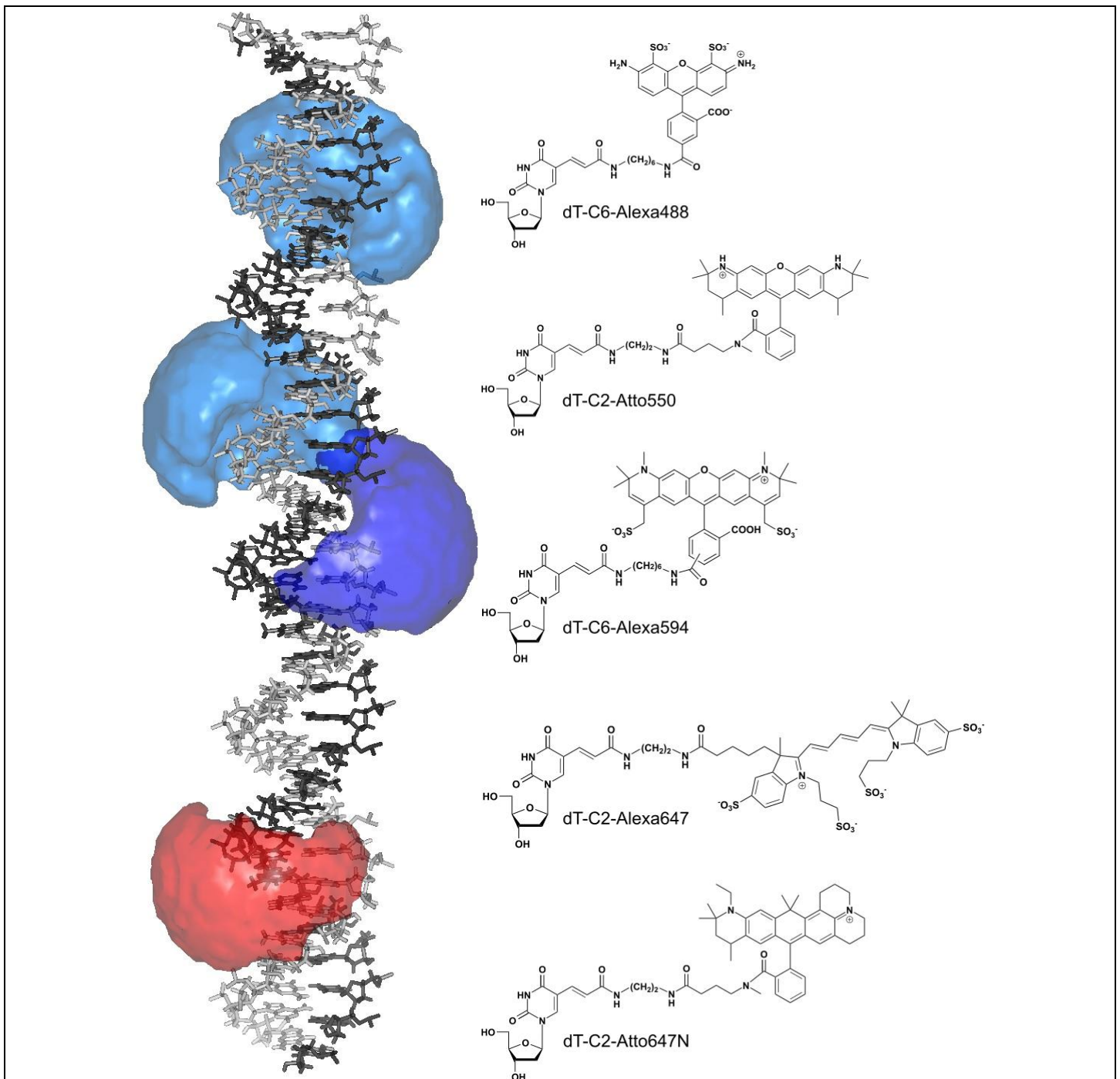
- Sindbert, S. et al. Accurate distance determination of nucleic acids via Förster resonance energy transfer: implications of dye linker length and rigidity. *J. Am. Chem. Soc.* **133**, 2463–2480 (2011).
- Nir, E. et al. Shot-noise limited single-molecule FRET histograms: comparison between theory and experiments. *J. Phys. Chem. B* **110**, 22103–22124 (2006).
- Barth, A., Voith von Voithenberg, L. & Lamb, D. C. MFD-PIE and PIE-FI: ways to extract more information with TCSPC. in *Advanced Photon Counting* Vol. 15 (eds Kapusta, P., Wahl, M. & Erdmann, R.) 129–157 (Springer, Cham, 2015).
- Schmid, S. & Hugel, T. Efficient use of single molecule time traces to resolve kinetic rates, models and uncertainties. *J. Chem. Phys.* **148**, 123312 (2018).
- Preus, S., Hildebrandt, L. L. & Birkedal, V. Optimal background estimators in single-molecule FRET microscopy. *Biophys. J.* **111**, 1278–1286 (2016).
- Neher, R. & Neher, E. Optimizing imaging parameters for the separation of multiple labels in a fluorescence image. *J. Microsc.* **213**, 46–62 (2004).
- Hildebrandt, L. L., Preus, S. & Birkedal, V. Quantitative single molecule FRET efficiencies using TIRF microscopy. *Faraday Discuss.* **184**, 131–142 (2015).
- Deniz, A. A. et al. Single-pair fluorescence resonance energy transfer on freely diffusing molecules: observation of Förster distance dependence and subpopulations. *Proc. Natl Acad. Sci. USA* **96**, 3670–3675 (1999).
- Antonik, M., Felekyan, S., Gaiduk, A. & Seidel, C. A. M. Separating structural heterogeneities from stochastic variations in fluorescence resonance energy transfer distributions via photon distribution analysis. *J. Phys. Chem. B* **110**, 6970–6978 (2006).
- Kalinin, S., Valeri, A., Antonik, M., Felekyan, S. & Seidel, C. A. M. Detection of structural dynamics by FRET: a photon distribution and fluorescence lifetime analysis of systems with multiple states. *J. Phys. Chem. B* **114**, 7983–7995 (2010).
- Clegg, R. M. Förster resonance energy transfer—FRET what is it, why do it, and how it's done. in *Laboratory Techniques in Biochemistry and Molecular Biology* Vol. 33 (ed Gadella, T. W. J.) 1–57 (Elsevier, Amsterdam, 2009).
- Braslavsky, S. E. et al. Pitfalls and limitations in the practical use of Förster's theory of resonance energy transfer. *Photochem. Photobiol. Sci.* **7**, 1444–1448 (2008).
- Knox, R. S. & van Amerongen, H. Refractive index dependence of the Förster resonance excitation transfer rate. *J. Phys. Chem. B* **106**, 5289–5293 (2002).
- Voros, J. The density and refractive index of adsorbing protein layers. *Biophys. J.* **87**, 553–561 (2004).
- Clegg, R. M. Fluorescence resonance energy transfer and nucleic acids. *Methods Enzymol.* **211**, 353–388 (1992).

In the format provided by the authors and unedited.

Precision and accuracy of single-molecule FRET measurements—a multi-laboratory benchmark study

Björn Hellenkamp^{1,2,33}, Sonja Schmid^{1,3,33}, Olga Doroshenko⁴, Oleg Opanasyuk⁴, Ralf Kühnemuth⁴, Soheila Rezaei Adariani⁵, Benjamin Ambrose⁶, Mikayel Aznauryan⁷, Anders Barth⁸, Victoria Birkedal⁷, Mark E. Bowen⁹, Hongtao Chen¹⁰, Thorben Cordes^{11,12}, Tobias Eilert¹³, Carel Fijen¹⁴, Christian Gebhardt¹², Markus Götz¹, Giorgos Gouridis^{11,12}, Enrico Gratton¹⁰, Taekjip Ha¹⁵, Pengyu Hao¹⁶, Christian A. Hanke⁴, Andreas Hartmann¹⁷, Jelle Hendrix^{18,19}, Lasse L. Hildebrandt⁷, Verena Hirschfeld²⁰, Johannes Hohlbein^{14,21}, Boyang Hua¹⁵, Christian G. Hübner²⁰, Eleni Kallis¹³, Achillefs N. Kapanidis²², Jae-Yeol Kim²³, Georg Krainer^{17,24}, Don C. Lamb⁸, Nam Ki Lee²³, Edward A. Lemke^{25,26,27}, Brié Levesque⁹, Marcia Levitus²⁸, James J. McCann⁹, Nikolaus Naredi-Rainer⁸, Daniel Nettels²⁹, Thuy Ngo¹⁵, Ruoyi Qiu¹⁶, Nicole C. Robb²², Carlheinz Röcker¹³, Hugo Sanabria⁵, Michael Schlierf¹⁷, Tim Schröder³⁰, Benjamin Schuler²⁹, Henning Seidel²⁰, Lisa Streit¹³, Johann Thurn¹, Philip Tinnefeld^{30,31}, Swati Tyagi²⁷, Niels Vandenberk¹⁸, Andrés Manuel Vera³⁰, Keith R. Weninger¹⁶, Bettina Wünsch³¹, Inna S. Yanez-Orozco⁵, Jens Michaelis^{13*}, Claus A. M. Seidel^{4*}, Timothy D. Craggs^{6,22*} and Thorsten Hugel^{1,32*}

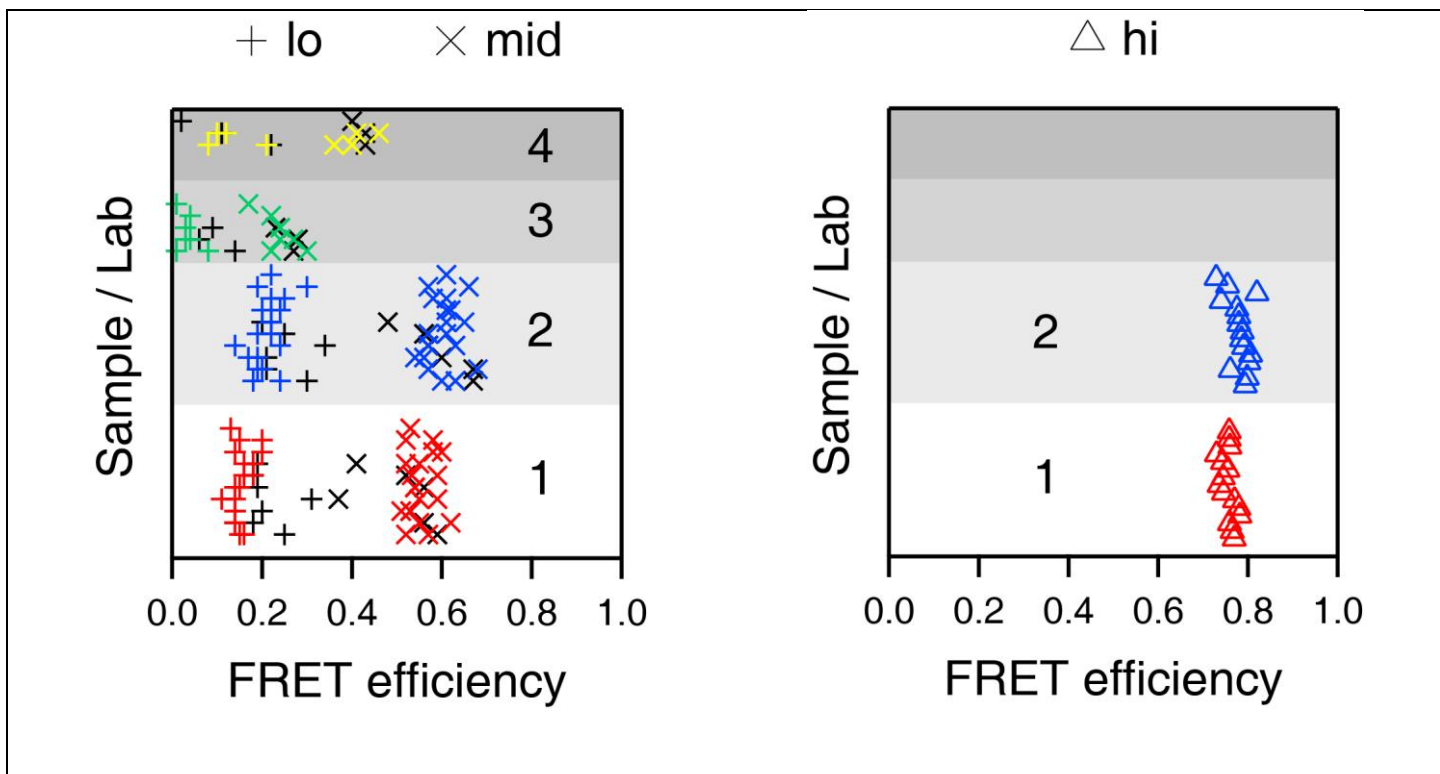
¹Institute of Physical Chemistry, University of Freiburg, Freiburg im Breisgau, Germany. ²Engineering and Applied Sciences, Columbia University, New York, NY, USA. ³Department of Bionanoscience, Kavli Institute of Nanoscience Delft, Delft University of Technology, Delft, the Netherlands. ⁴Molecular Physical Chemistry, Heinrich-Heine-Universität Düsseldorf, Düsseldorf, Germany. ⁵Department of Physics and Astronomy, Clemson University, Clemson, SC, USA. ⁶Department of Chemistry, University of Sheffield, Sheffield, UK. ⁷Interdisciplinary Nanoscience Center (iNANO) and Department of Chemistry, Aarhus University, Aarhus, Denmark. ⁸Physical Chemistry, Department of Chemistry, Nanosystems Initiative Munich (NIM), Center for Integrated Protein Science Munich (CiPSM) and Center for Nanoscience (CeNS), Ludwig-Maximilians-Universität München, Munich, Germany. ⁹Department of Physiology & Biophysics, Stony Brook University, Stony Brook, NY, USA. ¹⁰Department of Biomedical Engineering, University of California, Irvine, Irvine, CA, USA. ¹¹Molecular Microscopy Research Group, Zernike Institute for Advanced Materials, University of Groningen, Groningen, the Netherlands. ¹²Physical and Synthetic Biology, Faculty of Biology, Ludwig-Maximilians-Universität München, Planegg-Martinsried, Germany. ¹³Institute for Biophysics, Ulm University, Ulm, Germany. ¹⁴Laboratory of Biophysics, Wageningen University & Research, Wageningen, the Netherlands. ¹⁵Department of Biomedical Engineering, Johns Hopkins University, Baltimore, MD, USA. ¹⁶Department of Physics, North Carolina State University, Raleigh, NC, USA. ¹⁷B CUBE—Center for Molecular Bioengineering, TU Dresden, Dresden, Germany. ¹⁸Laboratory for Photochemistry and Spectroscopy, Department of Chemistry, University of Leuven, Leuven, Belgium. ¹⁹Dynamic Bioimaging Lab, Advanced Optical Microscopy Center and Biomedical Research Institute, Hasselt University, Hasselt, Belgium. ²⁰Institute of Physics, University of Lübeck, Lübeck, Germany. ²¹Microspectroscopy Research Facility Wageningen, Wageningen University & Research, Wageningen, the Netherlands. ²²Gene Machines Group, Clarendon Laboratory, Department of Physics, University of Oxford, Oxford, UK. ²³School of Chemistry, Seoul National University, Seoul, South Korea. ²⁴Molecular Biophysics, Technische Universität Kaiserslautern (TUK), Kaiserslautern, Germany. ²⁵Departments of Biology and Chemistry, Pharmacy and Geosciences, Johannes Gutenberg-University Mainz, Mainz, Germany. ²⁶Institute of Molecular Biology (IMB), Mainz, Germany. ²⁷Structural and Computational Biology Unit, European Molecular Biology Laboratory (EMBL), Heidelberg, Germany. ²⁸School of Molecular Sciences and The Biodesign Institute, Arizona State University, Tempe, AZ, USA. ²⁹Department of Biochemistry, University of Zurich, Zurich, Switzerland. ³⁰Department of Chemistry, Ludwig-Maximilians-Universität München, München, Germany. ³¹Institute of Physical & Theoretical Chemistry, Braunschweig Integrated Centre of Systems Biology (BRICS), and Laboratory for Emerging Nanometrology (LENA), Braunschweig University of Technology, Braunschweig, Germany. ³²BIOSS Centre for Biological Signalling Studies, University of Freiburg, Freiburg im Breisgau, Germany. ³³These authors contributed equally: Björn Hellenkamp, Sonja Schmid. *e-mail: jens.michaelis@uni-ulm.de; cseidel@hhu.de; t.craggs@sheffield.ac.uk; thorsten.hugel@pc.uni-freiburg.de



Supplementary Figure 1

DNA sample and utilized dyes.

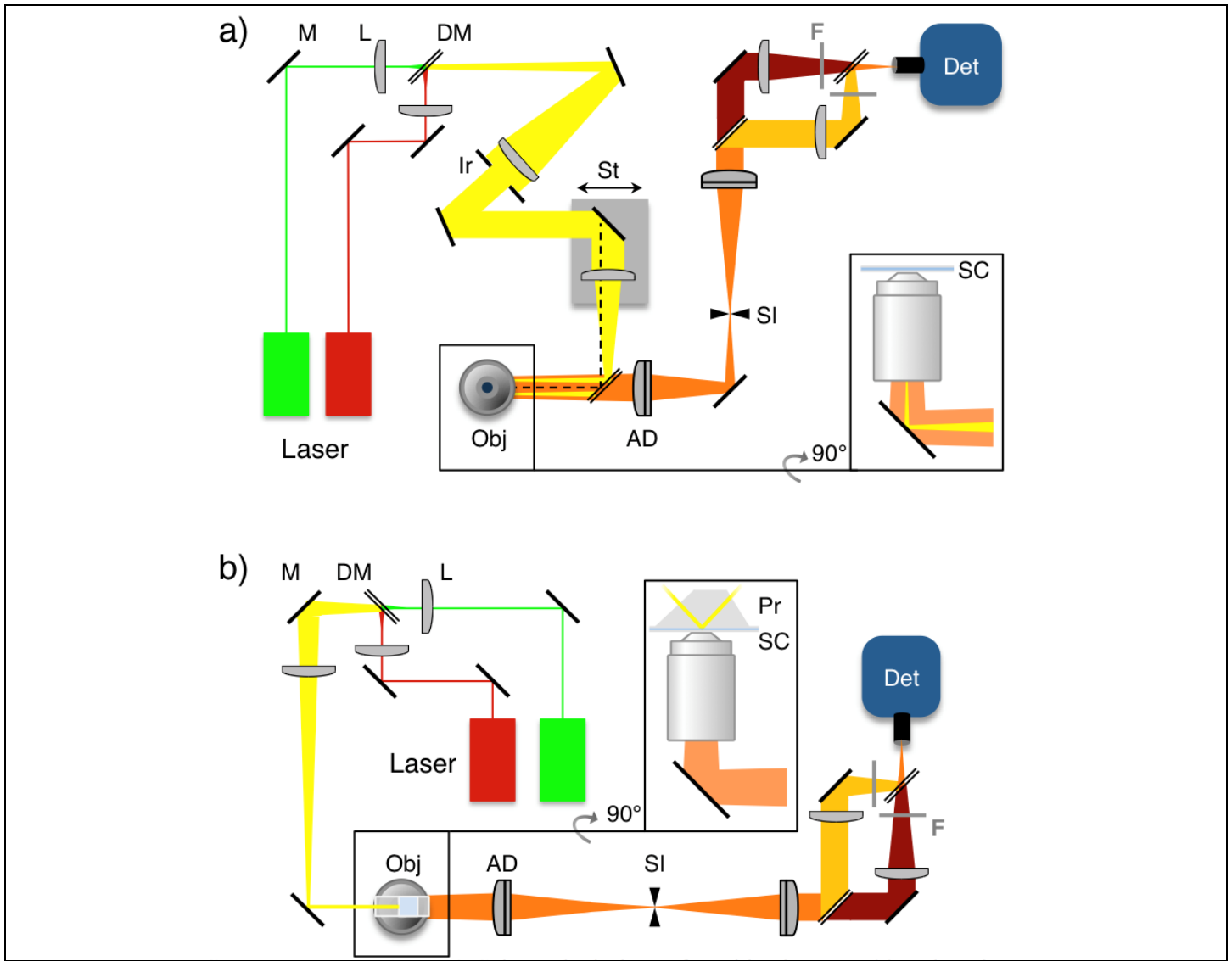
Left: DNA model with dye accessible volumes of the donor (blue) and acceptor (red) that were used in this study, indicating lo-, mid- and hi-FRET samples. Right: Structural formula of the dyes used in this study. Based on dyes from Molecular Probes / Thermo Fisher Scientific (Waltham, USA) and Atto-tec (Siegen, D).



Supplementary Figure 2

FRET efficiencies of all labs for all measured samples as indicated.

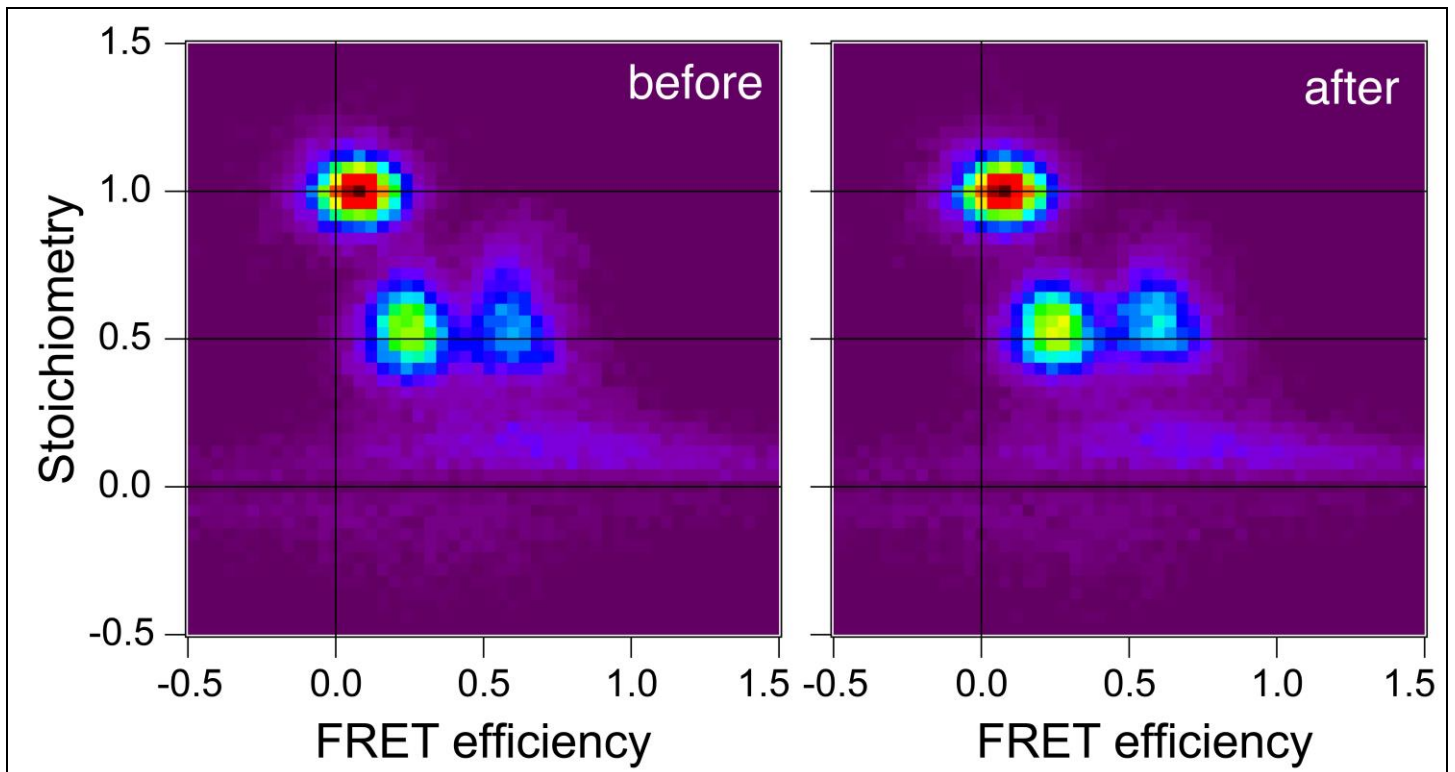
FRET efficiencies of all labs for all measured samples as indicated. Sample 1 to 4 (see Supplementary Table 1 and Supplementary Note 1) are color coded (red, blue, green, yellow) for all data points from intensity-based techniques. For a table of $R_{(E)}$ and R_{MP} and sample size for these measurements see Supplementary Table 4. Ensemble lifetime, single molecule lifetime and phasor approach derived data is shown in black. The FRET efficiencies (means and s.d.) for these measurements (depicted in black, sample size n) are: $E_{1a} = 0.21 \pm 0.05$ (n = 6); $E_{1b} = 0.51 \pm 0.08$ (n = 6); $E_{2a} = 0.25 \pm 0.06$ (n = 4); $E_{2b} = 0.59 \pm 0.07$ (n = 4); $E_{3a} = 0.10 \pm 0.04$ (n = 3); $E_{3b} = 0.26 \pm 0.03$ (n = 3); $E_{4a} = 0.12 \pm 0.10$ (n = 3); $E_{4b} = 0.42 \pm 0.02$ (n = 3). The left figure depicts all measurements from the main study, the right figure depicts all measurements from the later measurements of two additional samples (1-hi, 2-hi).



Supplementary Figure 4

Schematic designs of an objective-type (a) and a prism-type TIRF setup (b).

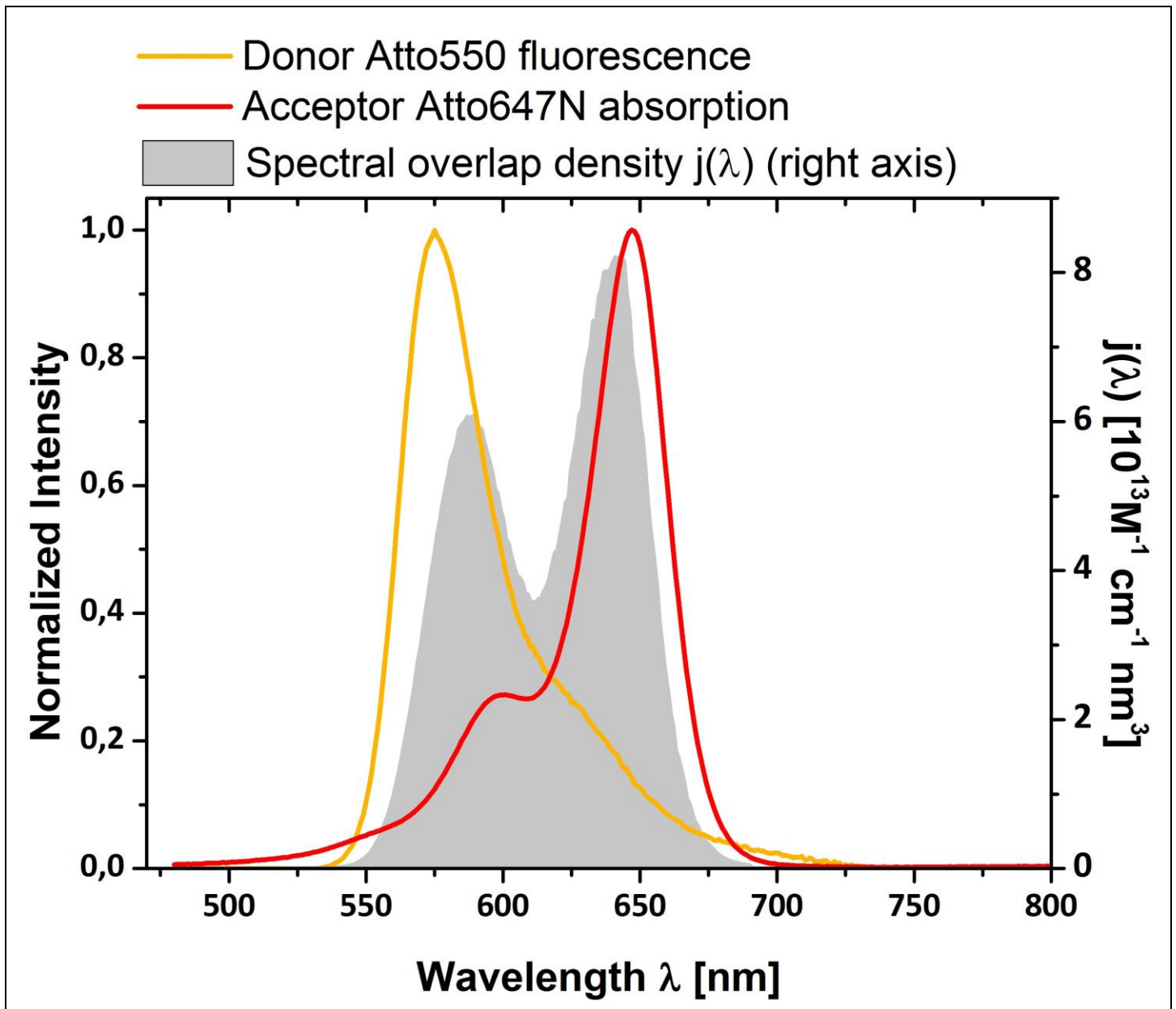
Green and red lasers are used to excite donor and acceptor dyes, respectively. M, mirror. L, lens. DM, dichroic mirror. Obj, objective. AD, achromatic doublet lens. SI, tunable slit. F, filters. Det, detector (e.g. electron multiplying charge-coupled device camera, EMCCD). The inset shows a side view of the objective with the out-of-plane (45°) mirror below. SC, sample chamber. Pr, prism. The dashed black line in (a) indicates the *on-axis* path to the objective, in contrast to the displayed *off-axis* path for TIR illumination. Elements used for the correction factors in Table 2 (main text) were: Dichroic before objective: F53-534 (AHF), Dichroics in detection: F33-726 and F33-644 (AHF). Band pass filters in detection: BP F39-572 and BP F37-677 (AHF). SI: SP40 (Owis), Objective: CFI Apo TIRF 100x, NA 1.49 (Nikon). Camera: EMCCD, iXonUltra, Andor. Lasers: 532nm, Compass 215M (Coherent) and 635nm, Lasiris (Stoker Yale). Note that we have used a Dichroic in the fluorescence excitation and emission path that reflects the higher wavelength, but this does not have any effect on the FRET efficiency measurement and related determination of correction factors. For details on all used setups and analysis software, see Supplementary Note 8.



Supplementary Figure 5

Correcting for differences in the excitation intensity in TIRF microscopy.

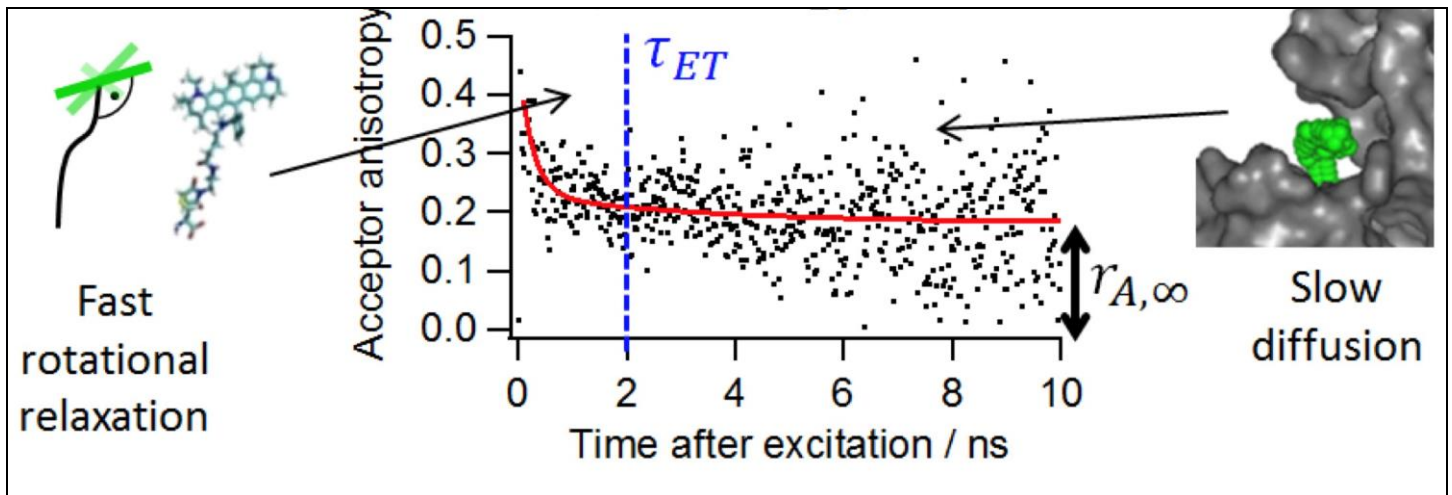
Accounting for the differences in the excitation intensity profiles of the green and red laser across the field of view. The individual excitation profiles are determined as the mean image of a stack of images recorded while moving across a dense layer of dyes. In contrast to the uncorrected case (“before”), a position specific normalization creates narrower and more symmetric SE-populations (“after”). The standard corrections described in the main text are performed subsequently.



Supplementary Figure 6

Computation of the spectral overlap integral J

Computation of the spectral overlap integral J for the FRET pair Atto550-Atto647N in sample 1. Normalized donor fluorescence and acceptor absorption spectra normalized to the maximum (left scale). Spectral overlap density $j(\lambda)$ (right scale) to compute the spectral overlap integral J [$\text{cm}^{-1}\text{M}^{-1}\text{nm}^4$] with $J = \int_0^\infty j(\lambda) d\lambda$ and $j(\lambda) = \bar{F}_D(\lambda)\epsilon_A(\lambda)\lambda^4$. The extinction coefficient ϵ_A of Atto647N was assumed to be $150000 \text{ M}^{-1}\text{cm}^{-1}$ at the maximum as provided by the manufacturer. The donor fluorescence and the acceptor absorption spectra were recorded in two laboratories in at least three independent experiments. Spectra with a flat baseline were selected. The computation was performed once.

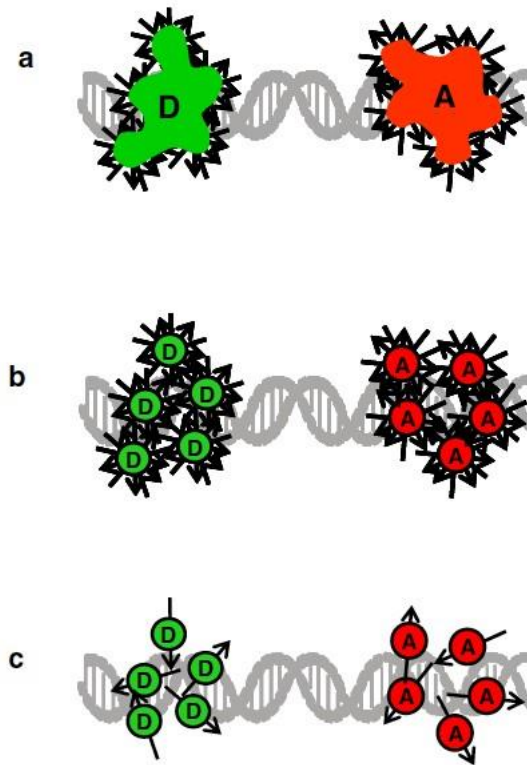


Supplementary Figure 7

Time-resolved anisotropies and FRET

The time-resolved anisotropies of dyes bound to a larger object (e.g. DNA or protein) normally consist of a fast decay from rotational relaxation of the dipole (left) and of a slow decay from translational relaxation (right). $\tau_{ET} = 1/k_{FRET}$: time of energy transfer; $r_{A,\infty}$: residual anisotropy of dye A. (Figure from ref. ¹). The data exemplarily shown is from a single measurement.

¹ Hellenkamp, B., Wortmann, P., Kandzia, F., Zacharias, M. & Hugel, T. Multidomain Structure and Correlated Dynamics Determined by Self-Consistent FRET Networks. *Nat. Meth.* 14, 174-180 (2017).



Supplementary Figure 8

Visualizations of different averages for efficiencies according to different fluorophore dynamics.

(a) Dynamic average, which applies in the case of the fluorophore movements being faster than the rate of energy transfer. There the rate of energy transfer has to be calculated taking into account the average over all possible distances and orientations. (b) Intermediate case, called the isotropic average, where the orientational variation of the fluorophores is faster than the rate of energy transfer while the positional variation is slower (c) Static case, where the fluorophore movements are much slower than the rate of energy transfer. In this case each distance and respective fluorophore orientation has to be taken into account with its individual transfer efficiency. These efficiencies then are averaged by the measurement process. (Figure from ref. ²).

² Wozniak, A. K., Schröder, G. F., Grubmüller, H., Seidel, C. A. M. & Oesterhelt, F. *Single-Molecule FRET Measures Bends and Kinks in DNA*. *Proc. Natl. Acad. Sci. USA* 105, 18337-18342 (2008).

Supplementary Material:

Precision and accuracy of single-molecule FRET measurements – a worldwide benchmark study

Björn Hellenkamp^{1a,°}, Sonja Schmid^{1a,°}, Olga Doroshenko²⁰, Oleg Opanasyuk²⁰, Ralf Kühnemuth²⁰, Soheila Rezaei Adariani¹⁵, Benjamin Ambrose², Mikayel Aznauryan⁹, Anders Barth²¹, Victoria Birkedal⁹, Mark E. Bowen¹¹, Hongtao Chen²⁶, Thorben Cordes^{14,25}, Tobias Eilert¹⁹, Carel Fijen⁷, Christian Gebhardt²⁵, Markus Götz^{1a}, Giorgos Gouridis^{14,25}, Enrico Gratton²⁶, Taekjip Ha²², Pengyu Hao¹², Christian A. Hanke²⁰, Andreas Hartmann¹⁷, Jelle Hendrix^{5,6}, Lasse L. Hildebrandt⁹, Verena Hirschfeld¹⁶, Johannes Hohlbein^{7,8}, Boyang Hua²², Christian G. Hübner¹⁶, Eleni Kallis¹⁹, Achillefs N. Kapanidis¹⁰, Jae-Yeol Kim²³, Georg Krainer^{17,18}, Don C. Lamb²¹, Nam Ki Lee²³, Edward A. Lemke^{3a,b,c}, Brié Levesque¹¹, Marcia Levitus²⁴, James J. McCann¹¹, Nikolaus Naredi-Rainer²¹, Daniel Nettels⁴, Thuy Ngo²², Ruoyi Qiu¹², Nicole C. Robb¹⁰, Carlheinz Röcker¹⁹, Hugo Sanabria¹⁵, Michael Schlierf¹⁷, Tim Schröder²⁷, Benjamin Schuler⁴, Henning Seidel¹⁶, Lisa Streit¹⁹, Johann Thurn^{1a}, Philip Tinnefeld^{13,27}, Swati Tyagi^{3c}, Niels Vandenberk⁵, Andrés Manuel Vera²⁷, Keith R. Weninger¹², Bettina Wünsch¹³, Inna S. Yanez-Orozco¹⁵, Jens Michaelis^{19,*}, Claus A.M. Seidel^{20,*}, Timothy D. Craggs^{2,10,*}, Thorsten Hugel^{1a,b,*}

Supplementary Information	Page
Supplementary Table 1 Samples	3
Supplementary Table 2 Spectroscopic parameters of the dyes in samples 1 and 2.	4
Supplementary Table 3 Typical correction factors	6
Supplementary Table 4 Resulting efficiencies and (relative) distances	6
Supplementary Table 5 Nomenclature and definitions	7
Supplementary Table 6 Typical dye parameters	8
Supplementary Note 1: Further samples	9
Supplementary Note 2 Time-resolved experiments	10
Supplementary Note 3 AV simulations to compute donor acceptor distances	15
Supplementary Note 4 FRET efficiency measurements and distance determinations in more complex systems, e.g. proteins	16
Supplementary Note 5 $R_{(E)}$ to R_{MP} conversion	17

Supplementary Note 6 Error propagation	20
Supplementary Note 7 MD simulations	21
Supplementary Note 8 Setup and data analysis details	25
Bibliography	35

Supplementary Table 1. The main focus in the manuscript are the 1 and 2 samples. The so-called donor strand (D-strand) is labeled with donor dye and acceptor strand (A-strand) with acceptor dye. The labeling sites of the donor and acceptor are shown in green and in red on the sequence respectively. See Supplementary Note 1 for further samples.

Name	Base position (Linker), strand	Dyes (Donor/Acceptor)	Sequence
1-lo	T 31(C2), D-strand T 31(C2), A-strand	Atto550 NHS Ester/ Atto647N NHS	5' - GAG CTG AAA GTG TCG AGT TTG TTT GAG TGT TTG TCT GG - 3' 3' - CTC GAC TTT CAC AGC TCA AAC AAA CTC ACA AAC AGA CC - 5' - biotin
1-mid	T 23(C2), D-strand T 31(C2), A-strand	Atto550 NHS Ester/ Atto647N NHS	5' - GAG CTG AAA GTG TCG AGT TTG TTT GAG TGT TTG TCT GG - 3' 3' - CTC GAC TTT CAC AGC TCA AAC AAA CTC ACA AAC AGA CC - 5' - biotin
1-hi	T 19(C2), D-strand T 31(C2), A-strand	Atto550 NHS Ester/ Atto647N NHS	5' - GAG CTG AAA GTG TCG AGT TTG TTT GAG TGT TTG TCT GG - 3' 3' - CTC GAC TTT CAC AGC TCA AAC AAA CTC ACA AAC AGA CC - 5' - biotin
2-lo:	T 31(C2), D-strand T 31(C2), A-strand	Atto550 NHS Ester/ Alexa647 NHS Ester	5' - GAG CTG AAA GTG TCG AGT TTG TTT GAG TGT TTG TCT GG - 3' 3' - CTC GAC TTT CAC AGC TCA AAC AAA CTC ACA AAC AGA CC - 5' - biotin
2-mid:	T 23(C2), D-strand T 31(C2), A-strand	Atto550 NHS Ester/ Alexa647 NHS Ester	5' - GAG CTG AAA GTG TCG AGT TTG TTT GAG TGT TTG TCT GG - 3' 3' - CTC GAC TTT CAC AGC TCA AAC AAA CTC ACA AAC AGA CC - 5' - biotin
2-hi:	T 19(C2), D-strand T 31(C2), A-strand	Atto550 NHS Ester/ Alexa647 NHS Ester	5' - GAG CTG AAA GTG TCG AGT TTG TTT GAG TGT TTG TCT GG - 3' 3' - CTC GAC TTT CAC AGC TCA AAC AAA CTC ACA AAC AGA CC - 5' - biotin

Supplementary Table 2: Spectroscopic parameters of the dyes in samples 1 and 2. Residual anisotropy r_∞ , combined anisotropy r_c , fluorescence quantum yields of donor and acceptor $\Phi_{F,D}$ and $\Phi_{F,A}$, respectively (determined according to the procedure detailed in the online methods), and species average fluorescence lifetimes $\langle\tau\rangle_x$ for the samples 1 (Atto550 /Atto647N) and the samples 2 (Atto550 /Alexa647). All measurements were done in 20mM MgCl₂,5mM NaCl,5mM TRIS at pH 7.5 measurement buffer.

Sample 1	1-lo (Atto550)	1-lo (Atto647N)	1-mid (Atto550)	1-mid (Atto647N)	1-hi (Atto550)	1-hi (Atto647N)
Base position (Linker), strand	T 31,(C2), D-strand	T 31(C2), A-strand	T 23(C2), D-strand	T 31(C2), A-strand	T 19 (C2), D-strand	T 31(C2), A-strand
Residual anisotropy $r_{A,\infty}$ or $r_{D,\infty}$ [a]	0.08	0.07	0.11	0.07	0.13	0.07
Combined anisotropy r_c	0.07		0.09		0.10	
Steady state anisotropy r_S	0.11	0.09	0.13	0.09	0.15	0.09
Lifetime $\langle\tau\rangle_x /$ ns (SD: 2%) [b]	3.76	3.62	3.81	3.62	3.74	3.62
Fluorescence quantum yield $\Phi_{F,D}$ or $\Phi_{F,A}$	0.76±0.015 [c]	0.65 [d]	0.77±0.015 [c]	0.65 [d]	0.76±0.015 [c]	0.65 [d]
fraction bright a_b [g]	≈ 1 [e]	≈ 1 [e]	≈ 1 [e]	≈ 1 [e]	≈ 1 [e]	≈ 1 [e]
R_θ [Å]	62.6					
$\langle\Phi_{F,D}\rangle$	0.765±0.015					
ϵ_A [M ⁻¹ cm ⁻¹]	150000					
J [cm ⁻¹ nm ⁴ M ⁻¹]	5.180·10 ¹⁵					
n_{im}	1.40					
κ^2	2/3					
Sample 2	2-lo (Atto550)	2-lo (Alexa647)	2-mid (Atto550)	2-mid (Alexa647)	2-hi (Atto550)	2-hi (Alexa647)
Base position (Linker), strand	T 31, (C2), D-strand	T 31(C2), A-strand	T 23(C2), D-strand	T 31(C2), A-strand	T 19 (C2), D-strand	T 31(C2), A-strand
Residual anisotropy $r_{A,\infty}$ or $r_{D,\infty}$ [a]	0.08	0.05	0.11	0.05	0.13	0.05
Combined anisotropy r_c	0.06		0.07		0.10	
Steady state anisotropy r_S	0.11	0.15	0.14	0.14	0.15	0.14
Lifetime $\langle\tau\rangle_x /$ ns (SD: 2%) [b]	3.76	1.19	3.81	1.19	3.74	1.19
Fluorescence quantum yield $\Phi_{F,D}$ or $\Phi_{F,A}$ [g]	0.77±0.015 [c]	0.39±0.015 [d]	0.77±0.015 [c]	0.39±0.015 [d]	0.77±0.015 [c]	0.39±0.015 [d]

fraction bright a_b [g]	≈ 1 [e]	0.75 ± 0.02 [f]	≈ 1 [e]	0.85 ± 0.02 [f]	≈ 1 [e]	0.86 ± 0.02 [f]
R_0 [Å]	68.0					
$\langle \Phi_{F,D} \rangle$	0.765					
ϵ_A [M ⁻¹ cm ⁻¹]	270000					
J [cm ⁻¹ nm ⁴ M ⁻¹]	$8.502 \cdot 10^{15}$					
n_{im}	1.40					
κ^2	2/3					

[a] The depolarization time of all species are given together with their amplitudes in *Supplementary Table N2.2*.

[b] The fluorescence lifetimes of all species are given together with their species fractions in *Supplementary Table N2.1*.

[c] Measured relative to Rhodamine 6G in a steady state spectrometer in air-saturated Ethanol with $\Phi_{F,Rh6G} = 0.95$. In the same measurement we obtained for the free dye $\Phi_{F,Atto550} = 0.8\pm 0.014$ and $\tau_{Atto550} = 3.60 \text{ ns} \pm 2\%$, which corresponds to the values given by the manufacturer.

[d] The following reference values for the free dyes in solution were used from the manufacturers to scale the fluorescence quantum via the fluorescence lifetime of the free dye:

$\Phi_{F,Atto647N} = 0.65$; $\tau_{Atto647N} = 3.5 \text{ ns}$; $\Phi_{F,Alexa647} = 0.33\pm 0.015$; $\tau_{Alexa647} = 1.0 \text{ ns}$. The parameters of Alexa647 agree nicely with the values for free Cy5 $\Phi_{F,Cy5} = 0.32\pm 0.015$ and $\Phi_{F,Cy5} = 0.38\pm 0.015$ Cy5-labelled dsDNA¹

A fluorescence lifetime analysis to relate the quantum yield Φ'_F and lifetime τ' specified by the manufacturer to the measured lifetime τ and quantum yield Φ_F :

$$\Phi_F = \Phi'_F \cdot \tau / \tau'$$

Here, we assume that the manufacturer Φ'_F is correct, that the radiative constant is unchanged and that the lifetime decay is monoexponential. For many dyes in distinct environments, this might not be the case.

[e] The excitation irradiance is usually low enough (especially in TIRF experiments) to avoid the population of dark states (triplet and radical states). The fraction of bright species a_b can be determined by fluorescence correlation spectroscopy.

[f] Cyanine dyes exhibit saturation effects due to cis-trans isomerization². Moreover, Widengren et al³ have shown that that the fraction of bright trans state a_b depends slightly on the FRET efficiency. In this study, we determined a_b by fluorescence correlation analysis of the FRET-sensitized acceptor signal in a confocal setup.

[g] Note that the correction factor γ was experimentally determined in this work. For completeness, we want to point out that the definition of γ in Online Methods section 1 can be used to compute the ratio of the detection efficiencies $g_{R|A}/g_{G|D}$ to check the detection performance of the setup provided the effective fluorescence quantum yields $^{eff}\Phi_F$ are known. Therefore we list the steady fluorescence quantum yields Φ_F and the fraction of bright species a_b .

Supplementary Table 3: Typical correction factors for sample 1 (Atto550-Atto647N) at given setups (reference lab). For the instrumental details of the setups see Supplementary Figures 3 and 4.

Factor	Experiment type	
	confocal	TIRF
α	0.11	0.07
β	1.80	0.85
γ	1.20	1.14
δ	0.11	0.065

Supplementary Table 4: Summary of resulting mean efficiencies $\langle E \rangle$, apparent distance $R_{\langle E \rangle}$, mean position distance R_{MP} and corresponding model distances $R_{\langle E \rangle}^{(model)}$ (Supplementary Note 3) and dynamic model distances $R_{\langle E \rangle}^{(dynamic\ model)}$ (Supplementary Note 7) and the experimental ratio $R_{rel} = R_{\langle E \rangle}^{(i)}/R_{\langle E \rangle}^{(mid)}$ and the model $R_{rel}^{(model)} = R_{\langle E \rangle}^{(model/i)} / R_{\langle E \rangle}^{(model,mid)}$ for all intensity based measurements. The errors (standard deviations) report on the precision of the measurements and not their accuracy. Literature values differ mainly because the refractive index of water is often assumed, while we used $n_{im} = 1.40$ here (see Online Methods, Section 4.1). Note that these errors only include the statistical variations of the FRET efficiencies, but do not include the error in the Förster radii, thus these errors represent the precision of the measurement, but not the accuracy. Including the knowledge of the dye attachment positions, a static structure of the DNA and this particular dye model, we computed also model values as described in Supplementary Note 3, which are also given here.

Sample	N	$\langle E \rangle$	R_0 [Å]	$R_{\langle E \rangle}$ [Å]	$R_{\langle E \rangle}^{(model)}$ [Å]	$R_{\langle E \rangle}^{(dynamic\ model)}$ [Å]	R_{rel}	$R_{rel}^{(model)}$	R_{MP} [Å]	$R_{MP}^{(model)}$ [Å]
1-lo	19	0.15±0.02	62.6±4.0	83.4±2.5	83.5±2.4	83.9	1.38	1.42	85.4±2.7	84.2±2.1
1-mid	19	0.56±0.03		60.3±1.3	58.7±1.6	60.3	1	1	58.2±1.7	55.8±2.3
1-hi	13	0.76±0.015		51.8±0.7	51.6±2.9	51.9	0.86	0.88	47.0±1.0	46.6±3.2
2-lo	19	0.21±0.04	68.0±5.0	85.4±3.4	83.9±2.2	84.2	1.34	1.41	86.9±3.7	84.2±2.4
2-mid	19	0.60±0.05		63.7±2.3	59.6±1.3	61.0	1	1	61.3±2.9	55.8±2.6
2-hi	13	0.78±0.025		55.0±1.3	52.3±1.9	52.6	0.86	0.88	50.1±1.8	46.6±1.8
3-lo	7	0.04±0.02	49.3[a]	89.5±12.3	82.4±2.4	83.1	1.49	1.46	85.7±5.3	84.0±2.1
3-mid	7	0.24±0.04	57.0[a]	60.1±2.3	56.4±1.6	58.4	1	1	61.1±2.9	55.7±2.3
4-lo	4	0.13±0.06		79.6±6.2	82.6±2.4	83.5	1.31	1.43	82.9±6.8	83.8±2.1
4-mid	4	0.41±0.04		60.7±1.7	57.6±1.6	59.5	1	1	60.4±2.3	55.5±2.3

[a] The R_0 for these samples have been taken from the literature and converted from a refractive index of $n_{im} = 1.33$ to $n_{im} = 1.40$:

Sample 3: $R_0 = 49.3$ Å from ref. ⁴

Sample 4: $R_0 = 57.0$ Å from ref. ⁵

Supplementary Table 5: Nomenclature and definitions. Since the nomenclature for FRET-based experiments is not consistent, we propose and use the following terms in this manuscript.

Central Definitions:	
$E = \frac{F_{A D}}{F_{D D} + F_{A D}}$	FRET efficiency (1)
$S = \frac{F_{D D} + F_{A D}}{F_{D D} + F_{A D} + F_{A A}}$	Stoichiometry (2)
$E = \frac{1}{1 + R_{DA}^6/R_0^6}$	FRET efficiency for a single donor acceptor distance R_{DA} (3)
$\langle E \rangle = \frac{1}{nm} \sum_{i=1}^n \sum_{j=1}^m \frac{1}{1 + \mathbf{R}_{A(j)} - \mathbf{R}_{D(i)} ^6/R_0^6}$	Mean FRET efficiency for a discrete distribution of donor acceptor distances with the position vectors $\mathbf{R}_{D(i)}$ and $\mathbf{R}_{A(j)}$ (4)
$R_{\langle E \rangle} \equiv R(\langle E \rangle) = R_0(\langle E \rangle^{-1} - 1)^{1/6}$	The apparent donor acceptor distance is computed from the average FRET efficiency for a distance distribution. It is a FRET averaged quantity which was also referred to as FRET-averaged distance $\langle R_{DA} \rangle_E$ (ref ¹). (5)
$R_{MP} = \left \langle \mathbf{R}_{D(i)} \rangle - \langle \mathbf{R}_{A(j)} \rangle \right $ $= \left \frac{1}{n} \sum_{i=1}^n \mathbf{R}_{D(i)} - \frac{1}{m} \sum_{j=1}^m \mathbf{R}_{A(j)} \right $	Distance between the mean dye positions with the position vectors $\langle \mathbf{R}_{D(i)} \rangle$ and $\langle \mathbf{R}_{A(j)} \rangle$ (6)
Subscripts:	
D or A	Concerning donor or acceptor
$A D$	Acceptor fluorescence given donor excitation, $D D, A A$ accordingly
$Aem Dex$	Intensity in the acceptor channel given donor excitation, $Dem Dex, Aem Aex$, accordingly
app	apparent, i.e. including systematic, experimental offsets
Superscripts:	
BG	Background
DO/ AO	Donor-only species/ Acceptor-only species
DA	FRET species
i -iii	Indicates (i) the uncorrected intensity; (ii) intensity after BG correction; (iii) intensity after BG, alpha and delta corrections
Correction Factors:	
$\alpha = \frac{g_{R D}}{g_{G D}} = \frac{\langle {}^{ii}E_{app}^{(DO)} \rangle}{1 - \langle {}^{ii}E_{app}^{(DO)} \rangle}$	Leakage of D fluorescence into A channel
$\beta = \frac{\sigma_{A R} I_{Aex}}{\sigma_{D G} I_{Dex}}$	Normalization of excitation intensities, I , and cross-sections, σ , of A and D
$\gamma = \frac{g_{R A} {}^{eff}\Phi_{F,A}}{g_{G D} {}^{eff}\Phi_{F,D}}$	Normalization of effective fluorescence quantum yields, ${}^{eff}\Phi_{F=a_b} \cdot \Phi_F$, and detection efficiencies, g , of A and D. a_b is the fraction of molecules in the bright state and Φ_F is the fluorescence quantum yield without photophysical (saturation) effects.

$\delta = \frac{\sigma_{A G} I_{Dex}}{\sigma_{A R} I_{Aex}} = \frac{\langle ii S_{app}^{(AO)} \rangle}{1 - \langle ii S_{app}^{(AO)} \rangle}$	Direct acceptor excitation by the donor excitation laser (lower wavelength)
Primary Quantities:	
I	Experimentally observed intensity
F	Corrected fluorescence intensity
τ	Fluorescence lifetime [ns]
$\Phi_{F,A}$ or $\Phi_{F,D}$	Fluorescence quantum yield of A and D, respectively
r	Fluorescence anisotropy
R	Inter-dye distance [\AA]
$\frac{R_0}{\text{\AA}} = 0.2108 \sqrt[6]{\left(\frac{\Phi_{F,D} \kappa^2}{n_{im}^4}\right) \frac{J}{M^{-1} \text{cm}^{-1} \text{nm}^4}}$	Förster radius [\AA], for a given J in units below (7)
$\kappa^2 = (\cos \theta_{AD} - 3 \cos \theta_D \cos \theta_A)^2$	Dipole orientation factor
$J = \int_0^\infty \bar{F}_D(\lambda) \varepsilon_A(\lambda) \lambda^4 d\lambda$	Spectral overlap integral [$\text{cm}^{-1} \text{M}^{-1} \text{nm}^4$] (see Supplementray Figure 6)
$\bar{F}_D(\lambda) \text{ with } \int_0^\infty \bar{F}_D(\lambda) d\lambda = 1$	Normalized spectral radiant intensity of the excited donor [nm^{-1}], defined as the derivative of the emission intensity F with respect to the wavelength.
$\varepsilon_A(\lambda)$	Extinction coefficient of A [$\text{M}^{-1} \text{cm}^{-1}$]
n_{im}	Refractive index of the medium in-between the dyes
$g_{R A}$ or $g_{G D}$	Detection efficiency of the red detector (R) if only acceptor was excited or green detector (G) if donor was excited. Analogous for others.
$\sigma_{A/G}$	Excitation cross-section for acceptor when excited with green laser. Analogous for the others.

Supplementary Table 6: Typical parameters for sample 1 and sample 2 that define R_0 (Seidel lab). For their determination see Online Methods section 4.

dye pairs	κ^2	n_{im}	$\Phi_{F,D}$	$\varepsilon_A [\text{M}^{-1} \text{cm}^{-1}]$	$J [\text{cm}^{-1} \text{M}^{-1} \text{nm}^4]$	$R_0 [\text{\AA}]$
Atto550-Atto647N	2/3	1.40	0.765	150000	$5.180 \cdot 10^{15}$	62.6
Atto550-Alexa647	2/3	1.40	0.765	270000	$8.502 \cdot 10^{15}$	68.0

Supplementary Note 1: Further samples

Name	Base position (Linker), strand	Dyes (Donor/ Acceptor)	Sequence
3-lo	T 31(C6), D-strand	Alexa488 Tetrafluorophenyl ester/	5' - GAG CTG AAA GTG TCG AGT TTG TTT GAG TGT TTG TCT GG-3'
	T 31(C2), A-strand	Atto647N NHS	3' - CTC GAC TTT CAC AGC TCA AAC AAA CTC ACA AAC AGA CC-5' - biotin
3-mid:	T 23(C6), D-strand	Alexa488 Tetrafluorophenyl ester/	5' - GAG CTG AAA GTG TCG AGT TTG TTT GAG TGT TTG TCT GG-3'
	T 31(C2), A-strand	Atto647N NHS	3' - CTC GAC TTT CAC AGC TCA AAC AAA CTC ACA AAC AGA CC-5' -biotin
4-lo:	T 31(C6), D-strand	Alexa488 Tetrafluorophenyl ester/	5' - GAG CTG AAA GTG TCG AGT TTG TTT GAG TGT TTG TCT GG-3'
	T 31(C6), A-strand	Alexa594 NHS	3' - CTC GAC TTT CAC AGC TCA AAC AAA CTC ACA AAC AGA CC-5' - biotin
4-mid:	T 23(C6), D-strand	Alexa488 Tetrafluorophenyl Ester/	5' - GAG CTG AAA GTG TCG AGT TTG TTT GAG TGT TTG TCT GG-3'
	T 31(C6), A-strand	Alexa594 NHS	3' - CTC GAC TTT CAC AGC TCA AAC AAA CTC ACA AAC AGA CC-5' - biotin

Even for samples 3 and 4 the precision of the hi-samples, where all individual FRET efficiencies were in a sensitive range of the specific dye pairs, is very good (2 - 4 %). Moreover, the experimental and model values of the low- and hi-samples agree very well with each other (the deviations range between 2 and 10 %). This suggests that we do not have dye artifacts for all four FRET pairs. The results obtained for the different FRET pairs will be important in the future to judge key aspects of different fluorophore properties.

NHS: N-hydroxysuccinidylester (mixed isomers according to the manufacturer)

TFP: (tetrafluorophenyl) ester (pure isomer according to the manufacturer)

Supplementary Note 2: Time-resolved experiments

Global fit of the time-resolved polarized and magic angle fluorescence ensemble data

All polarization resolved fluorescence decay curves ($F_{VV}(t), F_{VH}(t)$) with the Polarizer / Analyzer settings (Vertical, V /Horizontal, H) of singly labeled molecules were studied in ensemble experiments in the Seidel lab by high-precision time correlated single-photon counting and were fitted jointly with corresponding magic angle (M) fluorescence decay $f_{VM}(t) = f(t)$. To reduce the number of parameters in the fits we used the so called homogenous approximation⁶. We assumed that de-excitation and depolarization of dyes are independent, i.e. in each donor de-excitation state dyes are characterized by the same set of depolarization times. For this case we can write model functions for the decay of the excited state population $f(t)$ and the fluorescence anisotropy $r(t)$:

$$f_{VV}(t) = f(t)[1 + 2r(t)] \quad (2.1)$$

$$f_{VH}(t) = f(t)[1 - r(t)] \quad (2.2)$$

$$\text{with } f(t) = \sum_i x_i e^{-t/\tau_i} \quad \text{and } r(t) = \sum_j b^{(j)} e^{-t/\rho_j}$$

Here, τ is the fluorescence lifetime and ρ is the depolarization times. x_i is (with $\sum_i x^{(i)} = 1$) the species fraction of molecules having the lifetime τ_i and the factor b_j is fraction of molecules having the depolarization time ρ_j where the fundamental anisotropy r_0 is given by $\sum_j b^{(j)} = r_0$ and the residual anisotropy is given by $b^{(3)} = r_\infty$. A maximum of three species for i and j were necessary to obtain satisfactory fits judged by χ^2_r .

To fit real experimental decays IRF, background and amplitudes of the VV , VH signals are accounted as:

$$F_{VV}(t) = F_0 \cdot IRF_{VV}(t) \otimes f_{VV}(t) + B_{VV} \quad (2.3)$$

$$F_{VH}(t) = g_{VV/VH} F_0 \cdot IRF_{VH}(t) \otimes f_{VH}(t) + B_{VH} \quad (2.4)$$

Where $g_{VV/VH}$ is a correction factor for a polarization dependent detection efficiency, F_0 - amplitude scaling factor, $IRF_{VV}(t)$, $IRF_{VH}(t)$ - instrument response functions and B_{VV} , B_{VH} - background values. The “ \otimes ” sign designates circular convolution.

The fit results for fluorescent signal in parallel and perpendicular polarization planes with respect to the vertically polarized excitation light with their rotation correlation times and amplitudes for D-only and A-only labeled DNA are presented in Supplementary Tables N2.1 and N2.2. The measured data and fitted curves with their weighted residuals are presented in the first column of the Supplementary Figure N2.1. Typical magic angle fluorescence decays are shown in the right column of the Supplementary Figure N2.1.

As expected¹, the amplitude b_l for the fast depolarization motion with ρ_l is approximately a factor 2 larger for dyes where the transition dipole moment is more perpendicular to the linker (disc case: Alexa 488 and Alexa594) than for dyes with a more parallel the transition dipole moment (cone case: Atto550, Atto647N and Alexa647) (compare Supplementary Figure 1 and Supplementary Table N2.2). Note that some dyes (e.g. Alexa488 and Alexa594) depolarize especially fast, because they have a large fraction of the fastest depolarization time such that $k_{rot} \gg k_{FRET}$ might be satisfied

for even higher FRET efficiencies. The depolarization of these dyes is best described by a disc model ².

Supplementary Table N2.1: Fluorescence lifetimes τ_i and their amplitudes x_i for all studied Donor-only (DO) and Acceptor-only samples (AO). The quality of the fit was judged by χ^2_r . [a,b]

Base position (Linker), strand	Dye [c]	Sample (DO or AO)	τ_1 [ns] (x_1)	τ_2 [ns] (x_2)	τ_3 [ns] (x_3)	$\langle\tau\rangle_x$ [ns]	χ^2_r [d]
T 31(C2), D-strand	Atto550	1-lo (DO), 2-lo (DO)	0.74 (0.03)	3.47 (0.59)	4.44 (0.38)	3.76	1.03
T 23(C2), D-strand	Atto550	1-mid (DO), 2-mid (DO)	0.86 (0.03)	3.54 (0.63)	4.59 (0.34)	3.81	1.02
T 19(C2), D-strand	Atto550	1-hi (DO), 2-hi (DO)	0.50 (0.04)	3.02 (0.30)	4.31 (0.66)	3.74	1.05
T 31(C2), A-strand	Atto647N	1-(AO), 3-(AO)	0.24 (0.04)	3.40 (0.52)	4.19 (0.44)	3.62	1.03
T 31 (C2), A-strand	Alexa647	2-(AO)	0.66 (0.05)	1.18 (0.90)	1.90 (0.05)	1.19	1.00
T 31(C6), D-strand	Alexa488	3-lo (DO)	0.36 (0.03)	2.37 (0.05)	4.11 (0.92)	3.91	1.03
T 23(C6), D-strand	Alexa488	3-mid (DO)	0.37 (0.04)	2.70 (0.04)	4.13 (0.92)	3.92	1.08
T 31 (C6), A-strand	Alexa594	4-(AO)	0.31 (0.03)	3.76 (0.64)	4.55 (0.33)	3.91	0.99

[a] in 20mM MgCl₂, 5mM NaCl, 5mM TRIS at pH 7.5 measurement buffer.

[b] typical errors: average lifetime: $\tau \pm 0.02$ ns. Three lifetime: shortest lifetime $\tau_1 \pm 20\%$ (with $x_1 \sim 15\%$), $\tau_2 \pm 10\%$ (with $x_2 \sim 25\%$), $\tau_3 \pm 3\%$ (with $x_3 \sim 15\%$).

[c] Spectral settings:

Atto550 (fluor. max 574 nm): excitation wavelength 552 nm, emission wavelength 580 nm (bandpass 5.4 nm).

Atto647N (fluor. max 664 nm): excitation wavelength 635 nm, emission wavelength 665 nm (bandpass 9.2 nm).

Alexa647 (fluor. max 665 nm): excitation wavelength 635 nm, emission wavelength 665 nm (bandpass 8.1 nm).

Alexa488 (fluor. max 525 nm): excitation wavelength 485 nm, emission wavelength 520 nm (bandpass 9.2 nm).

Alexa594 (fluor. max 617 nm): excitation wavelength 590 nm, emission wavelength 617 nm (bandpass 8.1 nm).

Note that the fluorescence lifetime analysis exhibited signatures of solvent relaxation. Therefore, we use wide bandpasses.

[d] χ^2_r was computed from a non-linear least squares fit of the corresponding model function to TCSPC data. Thus, χ^2_r refers to a single data set.

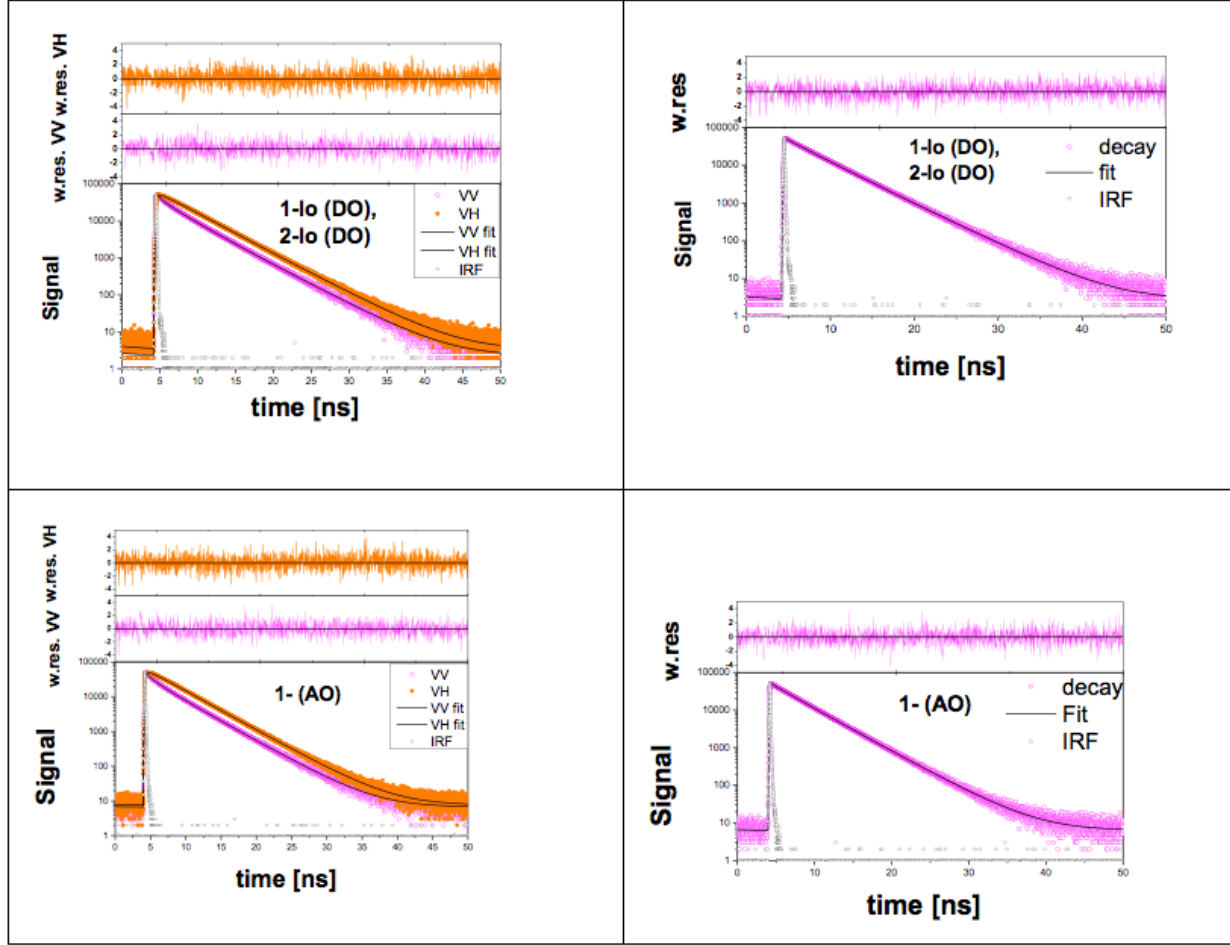
Supplementary Table N2.2: Rotation correlation times ρ_i with correspondent amplitudes b_i for Donor-only (DO) ($r_0=0.38$) and Acceptor-only (AO) ($r_0=0.38$) samples. The 1σ confidence range for the longest correlation time is indicated in square brackets. The fit model is described by eqs 2.1-2.2 with the model functions eqs. 2.3-2.4. The quality of the fit was judged by χ^2_r .

Base position (Linker),strand	dye	Sample (DO or AO)	ρ_1 [ns] (b_1)	ρ_2 [ns] (b_2)	ρ_3 [ns] (1σ conf.) ($b_3 = r_\infty$) [b]	χ^2_r [c]
T 31(C2), D-strand	Atto550	1-lo (DO), 2-lo (DO)	0.63 (0.14)	3.08 (0.16)	174 [97-540] (0.08)	1.04
T 23(C2), D-strand	Atto550	1-mid (DO), 2-mid (DO)	0.58 (0.12)	2.76 (0.15)	63 [50-86] (0.11)	1.01
T 19(C2), D-strand	Atto550	1-hi (DO), 2-hi (DO)	0.47 (0.10)	2.49 (0.16)	29.99 (0.13)	1.03
T 31(C2), A-strand	Atto647N	1-(AO), 3-(AO)	0.41 (0.14)	2.05 (0.17)	46 [37-62] (0.07)	1.01
T 31 (C2), A-strand	Alexa647 [a]	2 -(AO)	0.32 (0.09)	1.14 (0.23)	1e5 [125- ∞] (0.06)	0.99
T 31(C6), D-strand	Alexa488	3-lo (DO)	0.25 (0.22)	1.31 (0.12)	31 [24-42] (0.04)	1.03
T 23(C6), D-strand	Alexa488	3-mid (DO)	0.26 (0.22)	1.43 (0.12)	37 [31-46] (0.04)	1.04
T 31 (C6), D-strand	Alexa594	4-(AO)	0.46 (0.22)	1.88 (0.09)	77 [58-121] (0.07)	1.02

[a] Only VV, VH depolarization curves used for fitting in this case.

[b] Due to fluctuations in the G-factor determinations we have small systematic errors; i.e. $\rho_3 > 20$ ns and not the fitted value

[c] χ^2_r was computed from a non-linear least squares fit of the corresponding model function to. Thus, χ^2_r refers to a single data set.



Supplementary Figure N2.1: Left panels: Typical fluorescent signal in parallel and perpendicular polarization channels (magenta and orange) with the corresponding fits (black) for 1-lo (DO), 2-lo (DO), 1-(AO) samples with weighted residuals on the top. Right panels: the corresponding magic angle fluorescence decay curves with weighted residuals on the top. The fit results are displayed in Supplementary Tables N2.1 and N2.2 using fit procedure described by eqs 2.1-2.2 with the model functions eqs 2.3-2.4. The quality of the non-linear fit of the corresponding model function to TCSPC data was judged by χ^2_r . Thus, χ^2_r is a measure for the goodness of fit to a single data set.

Species average lifetime determination

Magic angle fluorescence decays were described with three fluorescence lifetimes τ_i and the species fractions x_i and thus species averaged lifetime $\langle \tau \rangle_x$ was calculated as:

$$\langle \tau \rangle_x = x_1 \tau_1 + x_2 \tau_2 + x_3 \tau_3 \quad (2.5)$$

Experimental deviations obtained during lifetime-based experiments

The lifetime-based measurements had a significantly lower precision and accuracy than intensity-based measurements. The following factors might be responsible for the observed deviations in the fluorescence lifetime-based FRET experiments:

1. The precision propagates differently for intensity based and time-resolved techniques. In intensity-based FRET measurements the relative error of a normalized donor-acceptor

distance changes less with increasing distance. The precision of time-resolved FRET measurements is highest for small DA distances (the minimum is $R_{DA}/R_0 \approx 0.7$) which were not the focus of this study ⁷.

2. Time-resolved techniques strongly depend on a representative (chemically equivalent) Donor-only reference sample that is crucial for resolving large distances accurately.
3. If in the ensemble measurements the FRET sample contains also molecules, which are labeled with a donor, it becomes very difficult to resolve species with low FRET efficiencies.
4. The accuracy of time-resolved FRET measurements depends on an appropriate fit model. It is crucial to consider the heterogeneity of the donor lifetimes and dye-linker distributions (eq. 27 in ref. ⁶). Moreover, the analysis model should allow fitting a variable fraction of donor-only species, which was needed for all provided samples. Altogether, this results in complex fit models which are not widely used in the FRET community because they are difficult to implement in commercial software. In contrast, some groups analyzed the donor decays by a simple series of exponentials, which results in a systematic shift of the obtained FRET parameters.

Thus, all four effects in time-resolved FRET measurements contributed to the fact that the precision and accuracy of the distances recovered especially for all lo-samples was markedly lower than that of intensity-based methods.

In contrast, the FRET efficiencies and inter-dye distances of the 1-hi and 2-hi samples were recovered very accurately by the Seidel lab as predicted by Ref⁶ (Fig. 11), because the effects 1-3 do not apply anymore.

Supplementary Note 3: AV simulations to compute donor acceptor distances

The model for the double-stranded B-DNA is generated using the Nucleic Acid Builder version 04/17/2017 for Amber⁸ (see Figure 1, main text). For modelling the dye molecule, we use a geometrical approach that considers sterically allowed dye positions within the linker length from the attachment point with equal probability. This defines the accessible volume (AV)⁹. The dye molecules are modeled as ellipsoids (approximated by three radii; AV3-Model) and AVs are generated using the FPS software¹⁰. For the distance computation a dye pair specific Förster Radius is used; i.e., it is assumed that within the AV the dye molecule samples all positions isotropically, however, for a single excitation it is at a fixed position. Moreover, it is assumed that dye rotation is so fast, that all possible orientations are sampled during the fluorescence lifetime and thus the factor $\langle \kappa^2 \rangle = 2/3$ (isotropic coupling).

The boundary tolerance (called ‘allowed sphere’ in the FPS software) is used to ignore small residues that are fixed in the PDB-model, but flexible in solution. The larger this value, the larger the structural parts that are ignored for the AV generation. The labelling position is the C7 of the thymine (the C-atom of the thymine’s methyl group). All mean geometric dyes parameters are estimated with ChemDraw software (see Supplementary Table N3.1). Further used parameters are: Boundary tolerance 0.5, accessible volume grid (rel.) 0.2; Min. grid [Å] 0.4, Search nodes: 3 and E samples: 200.

Supplementary Table N3.1: Recommended dye parameters for the AV simulations with AV3-model.

	linker length [Å]	linker width [Å]	R1 [Å]	R2 [Å]	R3 [Å]
dT-C6-Alexa488	20.5	4.5	5.0	4.5	1.5
dT-C2-Atto550	20.4	4.5	7.1	5.0	1.5
dT-C6-Alexa594	20.0	4.5	8.1	3.2	2.6
dT-C2-Alexa647	21.0	4.5	11.0	4.7	1.5
dt-C2-Atto647N	20.4	4.5	7.2	4.5	1.5

Error estimation. For each sample the distances between mean dye positions (R_{MP}^{model}) and expected experimentally observed apparent distance $R_{(E)}^{model}$ are calculated (see Supplementary Table 4). The error for the model distances is estimated by varying the linker lengths (from 10 to 21 Å), linker width (from 4.0 to 5.0 Å), the dye model (single sphere with the radius 6 Å (AV1 model) and ellipsoid with three radii R1=7.1 Å, R2=4.5 Å and R3=1.8 Å (AV3 model) and the boundary tolerance between dye and DNA (0.5 and 1.5 Å). The standard deviation of all DA distances computed by FPS was used as error.

Supplementary Note 4: FRET efficiency measurements and distance determinations in more complex systems, e.g. proteins.

The described determination of FRET efficiencies and their transformation into distances is fully generalizable to more complex systems like protein samples. However, uncertainties can arise from insufficient dynamic averaging of dye position and orientation, which might be caused by static or dynamic site specific dye quenching as well as transient interactions between the dye molecule and its local environment. This can (and should) be tested for each dye pair by measuring the time-resolved anisotropies of donor-acceptor labelled samples. As a result of such tests, dye pairs with insufficient dynamic averaging (a combined anisotropy of donor and acceptor > 0.2) can either be removed from the analysis¹¹ or described using different dye models¹²⁻¹⁴ (see also Online Methods). If this is done, the described error analysis is also fully transferable to protein systems. Note that the determined distance uncertainties (Fig. 5 and Online Methods) already include an estimated error for insufficient dynamic averaging.

Significant challenges arise from the need to label proteins with both donor and acceptor dyes. In systems where *intermolecular* distances are required, e.g. between different polypeptides (exchangeable homo dimers or hetero dimers), or between a protein and its bound DNA substrate, a single unique site on the protein for dye attachment is sufficient. In the case of homo dimers, the samples with two donors or two acceptors (about 25 % each) that will remain after the exchange, can be selected out following the ALEX procedure described in the main text. A single unique reaction site is often achieved using a unique reactive cysteine residue coupling to a maleimide-derivative of the chosen dye. However, this requires that other native, reactive cysteines are mutated (often to serine) and that the resulting ‘cys-lite’ protein remains active. For proteins with native reactive cysteines that cannot be removed by mutagenesis, incorporation of an unnatural amino acid carrying a completely orthogonal chemistry for dye attachment, or incorporation of specific peptide tags that can be site specifically labelled using enzymatic dye transfer reactions¹⁵ are possible strategies.

Intramolecular FRET measurements can be more challenging, given the need to put both the donor and acceptor on the same molecule. The stochastic labelling of double cysteine mutants, leads to at least four labelled populations (AD, DA, DD, AA). A key strength of the presented ALEX method is the ability to separate the FRET species (DA, AD) from donor-only (DD) or acceptor-only (AA) labelled species. The difference between mixed populations of donors attached at two different positions (i.e. DA vs AD) can be an issue for the width of the measured FRET distribution but becomes smaller with increasing linker lengths and presumably depends on the spatial separation of the dyes. For linkers comparable to the ones used in this study the standard deviation was previously determined to be ~ 0.8 Å (Ref⁶, Fig. 13). For some systems the differential reactivity of the two cysteines can be exploited to enable a biased labelling of the system¹⁶. Even a moderate (threefold) difference in local reactivity can yield highly specific double-labeling with sequential addition of the maleimide-dye derivatives. Alternatively, a combination with unnatural amino acids with mutually orthogonal reactivities can be incorporated¹⁷ (for a review see ref¹⁸).

Future work will involve a comparative blind study using protein samples. This will be an even larger study and the next step towards having FRET-based structures in the PDB. Yet it is important to note that the current study is essential as the pre-requisite to a future protein study, as it e.g. presents all the procedures unified across the field for the first time.

Supplementary Note 5: $R_{\langle E \rangle}$ to R_{MP} conversion

For the conversion between $R_{\langle E \rangle}$ and R_{MP} we distinguish two cases, a known and unknown environment of the dye molecule:

Case 1, the local environment of the dye molecule is known. Here, we use average (apparent) distances from different data-sources, i.e., $R_{\langle E \rangle}$ from experiment, and R_{MP} from coarse-grained-structural modeling to generate conversion functions. Typically, we use coarse-grained simulations to approximate accessible volumes (AVs) for biomolecules¹⁰. These AVs are translated / rotated and the average apparent DA distance ($R_{\langle E \rangle}$) and the distance R_{MP} are calculated, which introduces noise. The resulting conversion tables are approximated by third order polynomials. Here we used the AVs for the samples 1,2,3,4 low and high FRET correspondingly. For the polynomial $R_{MP} = (a_0 + a_1 R_{\langle E \rangle} + a_2 R_{\langle E \rangle}^2 + a_3 R_{\langle E \rangle}^3)$ the coefficients are given in the Supplementary Table N5.1 for all FRET pairs.

Note that the conversion functions are specific for the chosen dye pair because they depend on the Förster Radius of the FRET pair and the used dye parameters for the AV simulation. The differences between AVs in different molecular environments (DNA or protein) become smaller the less restricted the dye is. The offset of the conversion function depends on the size of the dye spheres and the linker lengths.

Supplementary Table N5.1. Conversion polynomial for $R_{MP} = (a_0 + a_1 R_{\langle E \rangle} + a_2 R_{\langle E \rangle}^2 + a_3 R_{\langle E \rangle}^3)$ using the dye pair specific R_0 and specific AVs of the samples 1, 2, 3 and 4, respectively. Note that these polynomials are only valid for this specific geometry and dyes.

FRET pair	R_0 [Å]	a_0 [Å]	a_1	a_2 [Å] ⁻¹	a_3 [Å] ⁻²
Atto550-Atto647N	62.6	-41.8	2.13	$-0.92 \cdot 10^{-2}$	$2.40 \cdot 10^{-5}$
Atto550-Alexa647	68.0	-40.3	1.99	$-0.74 \cdot 10^{-2}$	$1.67 \cdot 10^{-5}$
Alexa488-Atto647N	49.3	-53.8	2.83	$-1.89 \cdot 10^{-2}$	$6.17 \cdot 10^{-5}$
Alexa488-Alexa594	57.0	-43.9	2.24	$-1.02 \cdot 10^{-2}$	$2.48 \cdot 10^{-5}$

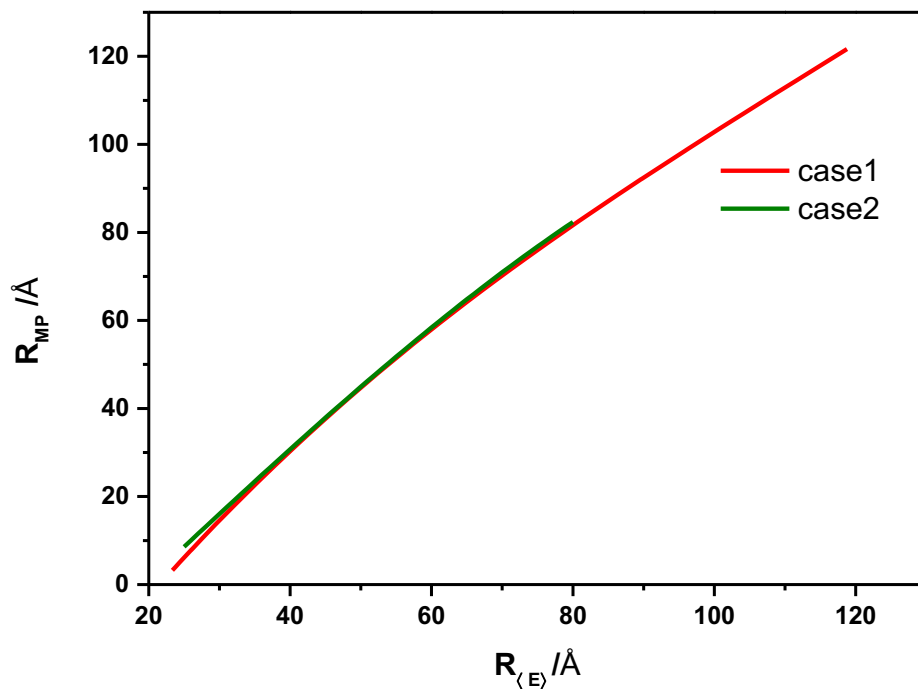
Case 2, the local environment of the dye molecule is not known. Here, we make the most general assumption that the AV can be approximated by a sphere with its radius estimated from the size of the dye and linker length (slightly smaller than the dye and linker length). This allows us to estimate the conversion of $R_{\langle E \rangle}$ to R_{MP} by performing Monte Carlo simulations¹⁹. In the Monte Carlo simulation, we place 10,000 positions uniformly distributed within a sphere of 18 Å radius for both dyes. For a given distance of the mean position of these spheres (R_{MP}) we calculate the respective FRET efficiencies via the Förster formula with an orientation factor of $\kappa^2 = 2/3$. The mean of these values is an unbiased estimate for the expected value of the FRET efficiency. We vary the mean position distance from $0.5 R_0$ to $1.5 R_0$ and fit the resulting means with a third order polynomial (coefficients a_0 , a_1 , a_2 and a_3). For convenience the conversion coefficients for a large range of used Förster radii were determined and given here in Supplementary Table N5.2.

The equivalence of both approaches is demonstrated in Supplementary Figure N5.1 for the dye pair Atto550-Atto647N.

Supplementary Table N5.2.: Coefficients for the conversion polynomials $R_{(E)}$ to R_{MP} for case 2. These are valid for the specified Förster radius R_0 .

R_0 [Å]	a_0 [Å]	a_1	a_2 [Å] ⁻¹	a_3 [Å] ⁻²
50	-33.6	1.65	$3.25 \cdot 10^{-3}$	$-7.26 \cdot 10^{-5}$
51	-34.0	1.70	$1.55 \cdot 10^{-3}$	$-5.68 \cdot 10^{-5}$
52	-33.0	1.64	$2.25 \cdot 10^{-3}$	$-5.85 \cdot 10^{-5}$
53	-31.7	1.57	$2.93 \cdot 10^{-3}$	$-5.91 \cdot 10^{-5}$
54	-32.8	1.64	$1.27 \cdot 10^{-3}$	$-4.65 \cdot 10^{-5}$
55	-32.0	1.61	$1.43 \cdot 10^{-3}$	$-4.46 \cdot 10^{-5}$
56	-30.0	1.51	$2.78 \cdot 10^{-3}$	$-4.98 \cdot 10^{-5}$
57	-30.0	1.51	$2.19 \cdot 10^{-3}$	$-4.39 \cdot 10^{-5}$
58	-30.0	1.52	$1.73 \cdot 10^{-3}$	$-3.91 \cdot 10^{-5}$
59	-27.7	1.42	$3.03 \cdot 10^{-3}$	$-4.37 \cdot 10^{-5}$
60	-29.1	1.49	$1.55 \cdot 10^{-3}$	$-3.42 \cdot 10^{-5}$
61	-27.5	1.42	$2.36 \cdot 10^{-3}$	$-3.67 \cdot 10^{-5}$
62	-26.5	1.37	$2.77 \cdot 10^{-3}$	$-3.74 \cdot 10^{-5}$
63	-27.3	1.42	$1.67 \cdot 10^{-3}$	$-2.99 \cdot 10^{-5}$
64	-25.6	1.35	$2.56 \cdot 10^{-3}$	$-3.28 \cdot 10^{-5}$
65	-26.1	1.38	$1.88 \cdot 10^{-3}$	$-2.83 \cdot 10^{-5}$
66	-26.4	1.39	$1.42 \cdot 10^{-3}$	$-2.50 \cdot 10^{-5}$
67	-24.9	1.33	$2.07 \cdot 10^{-3}$	$-2.69 \cdot 10^{-5}$
68	-24.1	1.30	$2.27 \cdot 10^{-3}$	$-2.68 \cdot 10^{-5}$
69	-24.2	1.31	$1.90 \cdot 10^{-3}$	$-2.39 \cdot 10^{-5}$
70	-23.3	1.28	$2.29 \cdot 10^{-3}$	$-2.49 \cdot 10^{-5}$
71	-24.4	1.33	$1.30 \cdot 10^{-3}$	$-1.95 \cdot 10^{-5}$
72	-23.4	1.29	$1.80 \cdot 10^{-3}$	$-2.11 \cdot 10^{-5}$
73	-22.6	1.27	$1.86 \cdot 10^{-3}$	$-2.04 \cdot 10^{-5}$
74	-23.0	1.28	$1.53 \cdot 10^{-3}$	$-1.84 \cdot 10^{-5}$
75	-22.4	1.26	$1.62 \cdot 10^{-3}$	$-1.80 \cdot 10^{-5}$
76	-21.8	1.24	$1.70 \cdot 10^{-3}$	$-1.77 \cdot 10^{-5}$
77	-21.6	1.24	$1.58 \cdot 10^{-3}$	$-1.66 \cdot 10^{-5}$
78	-21.8	1.25	$1.28 \cdot 10^{-3}$	$-1.47 \cdot 10^{-5}$
79	-21.2	1.23	$1.44 \cdot 10^{-3}$	$-1.49 \cdot 10^{-5}$
80	-21.2	1.24	$1.32 \cdot 10^{-3}$	$-1.41 \cdot 10^{-5}$
81	-20.5	1.22	$1.43 \cdot 10^{-3}$	$-1.39 \cdot 10^{-5}$
82	-20.3	1.21	$1.40 \cdot 10^{-3}$	$-1.34 \cdot 10^{-5}$
83	-20.5	1.22	$1.17 \cdot 10^{-3}$	$-1.20 \cdot 10^{-5}$
84	-19.8	1.20	$1.36 \cdot 10^{-3}$	$-1.24 \cdot 10^{-5}$
85	-20.3	1.22	$0.96 \cdot 10^{-3}$	$-1.05 \cdot 10^{-5}$
86	-19.5	1.19	$1.20 \cdot 10^{-3}$	$-1.10 \cdot 10^{-5}$
87	-19.1	1.18	$1.22 \cdot 10^{-3}$	$-1.08 \cdot 10^{-5}$
88	-19.0	1.18	$1.15 \cdot 10^{-3}$	$-1.02 \cdot 10^{-5}$
89	-19.0	1.18	$1.04 \cdot 10^{-3}$	$-0.95 \cdot 10^{-5}$
90	-18.8	1.18	$0.99 \cdot 10^{-3}$	$-0.91 \cdot 10^{-5}$

We tested that the polynomials derived using case 1 or case 2 yield almost identical conversion functions (Supplementary Figure N5.1).



Supplementary Figure N5.1. Polynomial $R_{MP} = a_0 + a_1 R_{(E)} + a_2 R_{(E)}^2 + a_3 R_{(E)}^3$ for the dye pair Atto550-Atto647N with AVs for DNA (case 1: $R_0 = 62.6 \text{ Å}$) and with the approximation by a sphere (case 2: $R_0 = 62.0 \text{ Å}$). Interpolated points in steps of 1 Å .

Supplementary Note 6: Error propagation

Based on the measurements of sample 1-lo and 1-hi, we performed an error propagation using $\Delta E = 0.033$ (which was the precision for these two best investigated samples). *Figure 5* follows from the following distance uncertainty:

$$\Delta R(R_0, \Delta R_0, \Delta E | R) = \sqrt{\left(\frac{\partial R(R_0, E)}{\partial R_0} \cdot \Delta R_0\right)^2 + \left(\frac{\partial R(R_0, E)}{\partial E} \cdot \Delta E\right)^2} = \sqrt{\left(\frac{R}{R_0} \cdot \Delta R_0\right)^2 + \left(\frac{1}{6} \left(1 + \left(\frac{R}{R_0}\right)^6\right)^2 \left(\frac{R}{R_0}\right)^{-5} R_0 \cdot \Delta E\right)^2} \quad (6.1)$$

In the following, we performed more detailed error propagation with disentangled error sources. We estimate the uncertainties of all quantities separately and propagate them towards an uncertainty in the distance. The overall uncertainty in the distance is given by:

$$\Delta R \left(R_0, \Delta R_0, \gamma, \Delta \gamma, \langle F \rangle, \Delta I_{Dem|Dex}^{(BG)}, \Delta I_{Aem|Dex}^{(BG)}, \Delta \beta, \Delta \alpha \middle| R \right) = \sqrt{\Delta R_{R_0}^2 + \Delta R_{\gamma}^2 + \Delta R_{bgD}^2 + \Delta R_{bgA}^2 + \Delta R_{\alpha}^2 + \Delta R_{\delta}^2} \quad (6.2)$$

with the following error contribution for the Förster radius:

$$\Delta R_{R_0}(R) = R \frac{\Delta R_0}{R_0} \quad (6.3)$$

And the following error contribution for the gamma factor:

$$\Delta R_{\gamma}(R) = \frac{R}{6} \cdot \frac{\Delta \gamma}{\gamma} \quad (6.4)$$

And the following error contribution for the background in the donor channel after donor excitation:

$$\Delta R_{bgD}(R) = \frac{R}{6} \left[\gamma \left(1 + \left(\frac{R_0}{R} \right)^6 \right) + \alpha \left(1 + \left(\frac{R}{R_0} \right)^6 \right) \right] \cdot \frac{\Delta I_{Dem|Dex}^{(BG)}}{\langle F \rangle} \quad (6.5)$$

And the following error contribution for the background in the acceptor channel after donor:

$$\Delta R_{bgA}(r) = -\frac{R}{6} \left(1 + \left(\frac{R}{R_0} \right)^6 \right) \cdot \frac{\Delta I_{Aem|Dex}^{(BG)}}{\langle F \rangle} \quad (6.6)$$

And the following error contribution for the direct excitation factor of the acceptor with the green laser:

$$\Delta R_{\delta}(R) = -\frac{R}{6} \beta \left(1 + \left(\frac{R}{R_0} \right)^6 \right) \cdot \Delta \delta \quad (6.7)$$

And the following error contribution for the leakage factor of donor fluorescence in the acceptor channel:

$$\Delta R_{\alpha}(R) = -\frac{R}{6} \frac{1}{\gamma} \left(\frac{R}{R_0} \right)^6 \cdot \Delta \alpha \quad (6.8)$$

Please note that for determination of background we set $\gamma = \beta = 1$ and $\alpha = \delta = 0$. This represents the ideal values. Further parameters and uncertainties are taken from the reference lab: $\Delta \gamma / \gamma = 0.1$, $\langle F \rangle = 50$, $\Delta I_{Dem|Dex}^{(BG)} = 1$, $\Delta I_{Aem|Dex}^{(BG)} = 1$, $\Delta \delta / \delta = 0.1$, $\Delta \alpha / \alpha = 0.1$, $\Delta R_0 = 0.07$. See Online Methods, Section 1 and 3 for the nomenclature and details on the Förster radius. $\langle F \rangle$ is the average sum of the corrected donor and acceptor fluorescence.

The above error analysis is based on R_{DA} and may be further propagated to the apparent donor-acceptor distance $R_{(E)}$ and the distance between the mean positions of the dyes, R_{MP} , when the above model assumption of a freely rotating and diffusing dye is applied. This becomes very involved and does not show significant deviations from *Figure 5* in the main text.

Supplementary Note 7: MD simulations

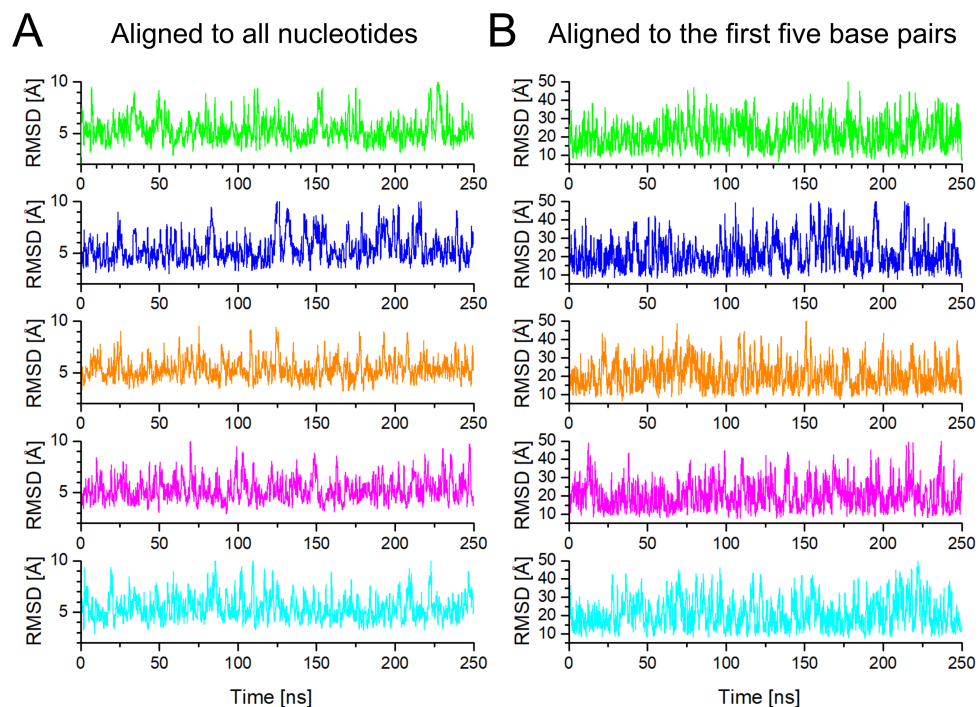
While the analysis in this paper used a static model for the double-stranded DNA structure, there is plenty of experimental and theoretical evidence that DNA is not completely rigid²⁰⁻²³. Therefore, we performed Molecular dynamics (MD) simulations of the DNA molecule to explore its rigidity using the latest force fields which were reported to be consistent with experimental observables of the conformational flexibility of dsDNA.

The all-atom MD simulations were performed with the Amber16 suite of programs²⁴ using the bsc1 force field⁸. The initial structure of the B-DNA molecule, which was generated by 3D-DART (see main text), was placed in an octahedral box of TIP3P water molecules²⁵, such that the distance between the edge of the water box and the closest DNA atom was at least 11 Å. MgCl₂ and NaCl were added to achieve concentrations of 20 mM and 10 mM, respectively. For Na⁺ and Cl⁻, the parameters by Joung and Cheatham²⁶ were used, while for Mg²⁺ the parameters by Li et al.²⁷ were used.

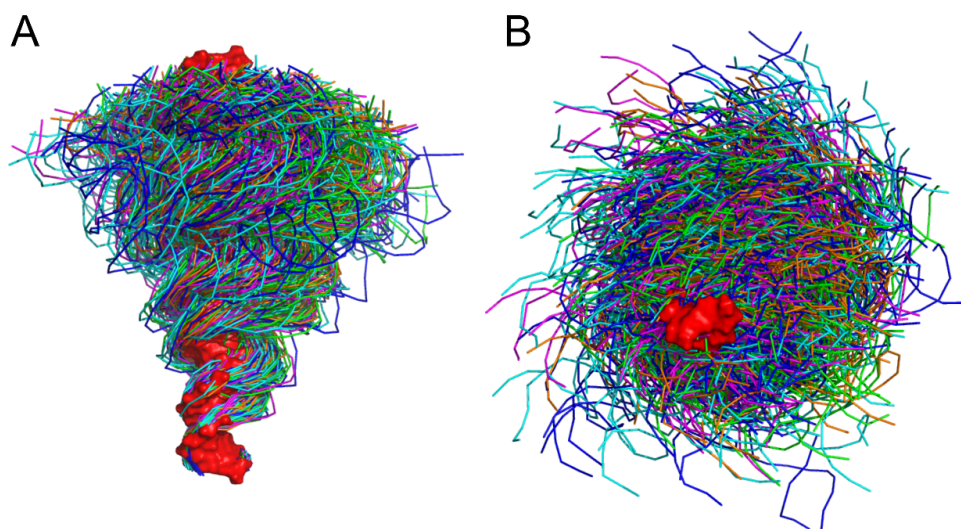
Each system was then prepared based on a protocol used earlier²⁸. The simulation system was minimized by 200 steps of steepest descent and subsequently 50 steps of conjugate gradient minimization. The minimized system was heated from 100 to 300 K over 50 ps, and subsequently the solvent density was adjusted for 150 ps by NPT-MD simulation. During the previous two steps, harmonic force restraints were applied on all solute atoms with force constants of 5 kcal mol⁻¹ Å⁻². These harmonic force restraints were gradually reduced to 1 kcal mol⁻¹ Å⁻² during 250 ps of NVT-MD simulation. This step was followed by 50 ps of NVT-MD simulation without positional restraints. Subsequently, we performed five independent MD simulations of 250 ns length each. The time step for all MD simulations was 2 fs. Coordinates were extracted from the simulations every 20 ps. The traces of the RMSD as a function of calculation time show that the calculations have converged (Supplementary Figure N.7.1).

We used the FPS program¹⁰ to calculate FRET efficiencies for the structural ensemble of the MD simulation, i.e. for each structure the AVs with the spatial dye (D and A) distributions is calculated and the average FRET efficiency is computed.

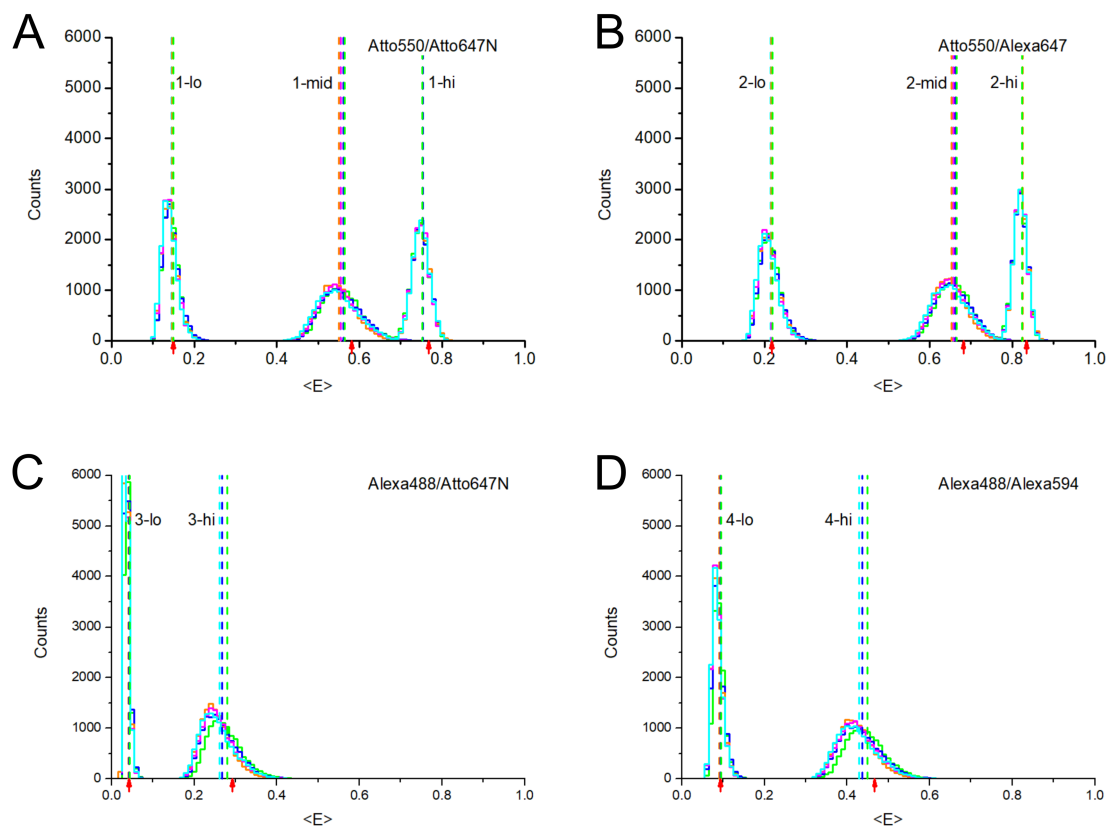
The ensembles from the MD simulations suggest that the DNA is not completely rigid, but exhibits some bending motion (Supplementary Figure N.7.2). The obtained distributions of FRET efficiencies show that the ensembles from the MD simulations yield comparable, but slightly lower mean FRET efficiencies and thus longer distances than for the static model (Supplementary Figure N.7.3, Supplementary Table N.7.1).



Supplementary Figure N.7.1: RMSD calculated over the simulation time for the five simulations performed. The RMSD was calculated with respect to the straight DNA molecules, which served as starting structure, considering all atoms for the calculation after aligning the structures to the straight DNA using all atoms (A) and only the first five base pairs (B). For better visibility, the lines were smoothed with a sliding average window of length 200 ps.



Supplementary Figure N.7.2: Structural ensembles from the MD simulations. The starting structure (red surface representation) was overlaid with conformations extracted from the MD simulations using the first 5 base pairs of the DNA. The five independent MD simulations are shown as differently colored ribbons (green, blue, orange, magenta, and cyan). For visibility, snapshots extracted every 2 ns were used for this representation. A: Side view; B: Top view.



Supplementary Figure N.7.3: Distribution of FRET efficiencies calculated for the conformation extracted from the MD simulations for the four samples (A: Atto550/Atto647N, B: Atto550/Alexa647, C: Alexa488/Atto647N, D: Alexa488/Alexa594). The five colors (green, blue, orange, magenta, and cyan) correspond to the five independent MD simulations performed. Vertical dashed lines indicate the mean of the distribution, while the red arrows below the X-axis indicate the values calculated for the starting structure.

Supplementary Table N.7.1: Comparison of FRET efficiencies $\langle E \rangle_{dyn}$ and corresponding DA distances $R_{\langle E \rangle}^{(dyn)}$ calculated from the five MD simulations to the values from experiments ($\langle E \rangle_{exp}$, $R_{\langle E \rangle}^{(exp)}$) and the static model with $\langle E \rangle_{static}$.

Sample	$\langle E \rangle_{dyn}$ ^[a]	$\langle E \rangle_{static}$ ^[b]	$\langle E \rangle_{exp}$ ^[c]	$R_{\langle E \rangle}^{(dyn)}$ [Å] ^[d]	$R_{\langle E \rangle}^{(exp)}$ [Å] ^[e]
Atto550/Atto647N					
1-lo	0.15	0.15	0.15 ± 0.02	83.9	83.4 ± 2.5
1-mid	0.56	0.58	0.56 ± 0.03	60.3	60.3 ± 1.3
1-hi	0.75	0.77	0.76 ± 0.02	51.9	51.7 ± 0.9
Atto550/Alexa647					
2-lo	0.22	0.22	0.21 ± 0.04	84.2	85.4 ± 3.4
2-mid	0.66	0.68	0.60 ± 0.05	61.0	63.7 ± 2.3
2-hi	0.82	0.83	0.78 ± 0.03	52.6	55.1 ± 1.6
Alexa488/Atto647N					
3-lo	0.04	0.04	0.04 ± 0.02	83.1	89.5 ± 12.3
3-mid	0.27	0.29	0.24 ± 0.04	58.4	60.1 ± 2.3
Alexa488/Alexa594					
4-lo	0.09	0.09	0.13 ± 0.06	83.5	79.6 ± 6.2
4-mid	0.44	0.47	0.41 ± 0.04	59.5	60.7 ± 1.7

[a] Calculated as average over the five simulations (the standard deviation is in all cases below 0.008).

[b] Calculated for the static starting structure.

[c] From measurements (cf. Supplementary Table 4).

[d] Calculated from $\langle E \rangle_{dyn}$ using Formula (5) in the main text. The SD is not significant (determined by an error propagation from [a]).

[e] Calculated from experiments (cf. Supplementary Table 4).

Supplementary Note 8: Description of setups and analysis software *(in alphabetic order)*

Birkedal lab (TIRF)

Single-molecule FRET experiments were performed on surface-immobilized molecules using a prism-based total internal reflection microscope with a set up similar to Supplementary Figure 4b. About 5 pM labeled molecules were immobilized inside a coverslide chamber and imaged using alternating laser excitation with 532 and 648 nm diode lasers (Cobolt) or with 514 and 630 nm lasers (Coherent). Fluorescence from the donor and acceptor fluorophores was spatially separated using a wedge mirror (Chroma Technology Corp.) and detected with two color channels onto an EMCCD camera (iXON 3 897, Andor). Details of the experimental setup and immobilization procedures are published elsewhere²⁹.

Movies were recorded with a 200 ms integration time per frame and analyzed using the iSMS software³⁰. The newest version of the software is available at www.isms.au.dk.

Bowen lab (TIRF)

Samples were imaged using a prism-based Total Internal Reflection Fluorescence microscope constructed on an IX71 base with a 60x, 1.2 NA water-immersion objective (Olympus, Center Valley, PA)³¹. Alternating laser excitation, with mechanical shutters (Uniblitz, Rochester, NY), was used to confirm the presence of both a donor and acceptor dye in all molecules used for analysis. Samples were excited with: a laser diode at 635 nm (Newport Corporation, Irvine, CA) for Alexa 647 and Atto 647N; a diode pumped solid-state laser at 532 nm (Newport Corporation, Irvine, CA) for Atto 550; or a laser diode at 473 nm (Photop Technologies Inc. Chasworth, Ca) for Alexa 488. Emission from donor and acceptor was separated using an Optosplit ratiometric image splitter (Cairn Research Ltd, Faversham UK). For experiments with Atto 550 and Alexa 647 (or Atto 647N), we used a 645 nm dichroic mirror with a 585/70 band pass filter for the donor channel and a 670/30 band pass filter for the acceptor channel. For experiments with Alexa 488 and Atto 647N, we used a 593 nm dichroic mirror with a 550/100 band pass filter for the donor channel and a 700/75 band pass filter for the acceptor channel (all filters from Chroma, Bellows Falls, VT). The replicate images were relayed to a single iXon DU-897 EMCCD camera (Andor Technologies, Belfast, UK) at a frame rate of 10 Hz.

Data was processed in home written MATLAB scripts to cross-correlate the replicate images and extract time traces for diffraction limited spots with intensity above baseline³². Single molecules were verified by selecting only events showing single step photobleaching to baseline. The γ correction was individually calculated for each selected molecule based upon the relative changes in intensities before and after the photobleaching event.

Cordes Lab (confocal)

Measurements were performed on a confocal setup, as shown in Supplementary Figure 3, but with the addition of a fiber coupling between the laser combining dichroic mirror DM1 and the second dichroic mirror DM2 to improve and clean the beam profile³³.

Elements used were: ZET532/10x (Chroma/AHF) and ZET640/10x (Chroma/AHF) laser clean-up filter (right after Laser 532 and 640 nm); polarization maintaining single-mode fiber P3-488PM-FC-2 (Thorlabs); DM2: Dual line beam splitter ZT532/640rpc (Chroma/AHF); DM3: laser-laser beam splitter H643 LPXR (AHF); FG: BrightLine HC 582/75 (Semrock/AHF); FR: Longpass 647 LP Edge Basic (Semrock/AHF); Objective: Super achromat objective UPLSAPO60XW (Olympus); Detectors: SPAD SPCM-AQRH-64 (Excelitas); Pinholes: 50 μm ; Laser power at sample: $\approx 60 \mu\text{W}$ for 532 nm and $\approx 25 \mu\text{W}$ for 640 nm; Beam diameter $\approx 12 \text{ mm}$.

Laser-APD synchronization and readout is performed with NI-Card PCI-6602 (National Instruments) and a LabView (LabVIEW 2009) based home written software³³.

Analysis was also done with a LabView based home written software.

Craggs lab (confocal)

Setup is similar to Supplementary Figure 3, with the following specifications: Lasers used are 515 nm and 635 nm – LuxX plus, precoupled (No DM₁). DM₂ is a Chroma ZT532/640rpc excitation dichroic. The objective O is a Olympus x60 objective UPLSAPO 60XO (WD = 0.17 mm). The lense L is a Edmond Optics 49793 (50 mm focal length). The pinhole PH is a 20 μm (Newport PNH-20). The dichroic DM₃ is a 640 nm longpass (Chroma NC395323 – T640lpxr). The F_G is a Semrock: FF01-582/75-25. The F_R a Semrock: FF01-679/41-25. The APD an Excelitas SPCM-AQRH-14.

The following description is from Bennet et al.³⁴:

smFRET data were acquired using a custom built confocal microscope and alternating laser excitation. Two diode lasers (515 nm and 635 nm – LuxX plus) were directly modulated (100 us, duty cycle 45%) and combined into an optical fibre. The output beam was collimated and then cropped to 2.5 mm diameter by an iris. The beam was directed into the back of the objective (Olympus UPLSAPO 60 \times NA = 1.35 oil immersion) using a dichroic mirror (Chroma ZT532/640 rpc 3 mm) with the fluorescence emission collected by the same objective, focussed onto a 20 μm pinhole and then split (dichroic mirror: Chroma NC395323 – T640lpxr) for detection by two avalanche photodiodes (SPCM-AQRH-14 and SPCM-NIR-14, Excililas). Photon arrival times were recorded by a national instruments card (PCIe-6353), with the acquisition controlled using custom software (LabView 7.1).

Gratton lab (confocal)

The measurements were done on a modified Olympus FV1000 laser scanning confocal microscope. It is similar to Supplementary Figure 3. Our excitation source was a 20 MHz supercontinuum laser (SC390, Fianium Inc). A filter-wheel with eight interference bandpass filters was used to select desired excitation wavelengths. In our measurements, one set data was collected with the excitation from 530-550nm and the emission from 560-620nm. The other set data was collected with the excitation from 483-493nm and the emission from 505-525nm. An Olympus60 \times water objective (Olympus UPlanSApo, NA=1.2) was used to focus the laser beam and collect the emission signal.

The internal PMT was modified to send the signal out to a FastFLIM system (ISS Inc), which was synchronized with the 20MHz frequency output from the laser.

Data was then collected and analyzed by SimFCS (available from <http://www.lfd.uci.edu/>).

Ha lab (TIRF)

Measurements were done on a setup similar to Supplement Figure 4. Instead of using lenses and dichroic mirrors in the excitation pathway to combine the lasers, half-wave plates and a polarizing beam splitter cube were used. The collected fluorescence then passes a slit as shown, and is split with a dichroic and redirected through a lens using only mirrors, so that the two images are put beside each other on the camera chip.

Dichroics in detection: FF640-FDi01-25×36 (Semrock). Filters in detection: BLP02-561R-25 (F1, Semrock) and ZET633TopNotch (F2, Chroma). Objective: water immersion, 60 ×/1.2 NA (Olympus). Camera: EMCCD (iXon 897, Andor). Lasers: 532 nm (Compass 315M, Coherent) and 633 nm (06-MLD, Cobolt).³⁵

Data were analyzed by custom-made MatLab codes.

Hendrix lab (confocal)

Our multi-parameter fluorescence detection setup equipped with pulsed interleaved excitation is conceptually identical to the confocal microscope presented in Supplementary Figure 3. Emission from a pulsed 483-nm laser diode (LDH-P-C-470, Picoquant, Berlin, Germany) was cleaned up (Chroma ET485/20x, F49-482, AHF Analysentechnik, Tübingen, Germany), emission from a 635-nm laser diode (LDH-P-C-635B, Picoquant) was cleaned up (Chroma z635/10x, Picoquant) and both lasers were alternated at 26.67 MHz (PDL 828 Sepia2, Picoquant), delayed ~18-ns with respect to each other and combined via a 483-nm-reflecting dichroic mirror in a single-mode optical fiber (coupler: 60FC-4-RGBV11-47, fiber: PMC-400Si-2.6-NA012-3-APC-150-P, Schäfter und Kirchhoff GmbH, Hamburg, Germany). After collimation (60FC-L-4-RGBV11-47, SuK GmbH), the linear polarization was cleaned up (Codixx VIS-600-BC-W01, F22-601, AHF) and the light was reflected on a 3-mm thick excitation polychroic mirror (Chroma zt470-488/640rpc, F58-PQ08, AHF) upward and into the back port of the microscope (IX70, Olympus Belgium NV, Berchem, Belgium) via two mirrors and upward to the sample (3-mm thick Full Reflective Ag Mirror, F21-005, AHF, mounted in a TIRF Filter Cube for BX2/IX2, F91-960, AHF) to the objective (UPLSAPO-60XW, Olympus). Sample emission was transmitted focused through a 75- μ m pinhole (P75S, Thorlabs, Munich, Germany) via an achromatic lens (AC254-200-A-ML, Thorlabs), collimated again (AC254-50-A-ML, Thorlabs) and spectrally split (Chroma T560lpxr, F48-559, AHF). The blue range was filtered (Chroma ET525/50m, F47-525, AHF) and polarization was split (PBS251, Thorlabs). The red range was also filtered (Chroma ET705/100m, AHF) and polarization was split (PBS252, Thorlabs). Photons were detected on four avalanche photodiodes (Perkin Elmer or EG&G SPCM-AQR12/14), which were connected to a time-correlated single photon counting (TCSPC) device (SPC-630, Becker & Hickl GmbH, Berlin, Germany) over a router (HRT-82,

Becker & Hickl) and power supply (DSN 102, Picoquant). Signals were stored in 12-bit first-in-first-out (FIFO) files.

All analyses of experimental data were performed in the software package PAM³⁶. The software is available as source code, requiring MATLAB to run, or as pre-compiled standalone distributions for Windows or MacOS at <http://www.cup.uni-muenchen.de/pc/lamb/software/pam.html> or hosted in Git repositories under <http://www.gitlab.com/PAM-PIE/PAM> and <http://www.gitlab.com/PAM-PIE/PAMcompiled>. Sample data is provided under <http://www.gitlab.com/PAM-PIE/PAM-sampled>. A detailed manual is found under <http://pam.readthedocs.io>.

Hohlbein lab (TIRF)

Our setup is conceptually identical to the TIRF microscope presented in Supplementary Figure 4 (for TIRF)³⁷. For excitation, we used a fibre-coupled laser engine (Omicron, Germany) equipped with four lasers of different wavelengths (405 nm, 473 nm, 561 nm, and 642 nm). A home-written LabVIEW program independently controlled the laser intensities and triggered the camera. The single mode fibre generated a Gaussian shaped beam profile and a point source output at the other end of the fibre. The divergent light is collimated ($f = 100$ mm, Thorlabs, Germany) and a second lens focuses ($f = 200$ mm, Thorlabs, Germany) the light back into the back focal plane of a 100x NA 1.49 TIRF objective (Nikon, Japan). A polychroic mirror (zt405/473/561/640rpc, Chroma, USA) and a multibandpass filter (zet405/473/561/640m, Chroma, USA) are used to block any laser light in the emission path. After spatial filtering of the fluorescence with a two-lens system consisting of two tube lenses ($f = 200$ mm, Thorlabs, Germany) and an adjustable slit (Thorlabs, Germany), the light was spectrally split using two dichroic mirrors (zt561rdc and zt640rdc, Chroma) and a mirror into three beams corresponding to a blue, green, and red fluorescence detection channel. The three beams were then focused ($f = 300$ mm) on an Ixon Ultra 897 emCCD camera with 512 x 512 pixel (Andor, Northern-Ireland) that was operated in a photon-counting mode.

For image analysis we used a modified version of TwoTone, a freely available, MATLAB-based software package, which identifies molecules and measures the photon counts by fitting the molecular point spread functions to two dimensional Gaussians³⁸.

Hübner lab (confocal)

The setup was similar to Supplementary Figure 3 with the following components. Donor and acceptor excitation was done with a cw laser at 532 nm (GCL-005-L-LK, Crystalaser, Reno, NV) for the donor and a 635 nm pulsed laser diode (LDH-P-635+Sepia -PDL-808, Picoquant GmbH, Germany) using 100 ps pulses at 10 MHz for the acceptor. Lasers were put through a glass fiber (SMC-460, Schäfter und Kirchhoff) and collimated with UPLSAPO 4X collimation lens. Combining the lasers was accomplished with dichroic mirror Q555LP (Chroma, DM1). Dichroic DM2 was a Z532/633 (Chroma). Fluorescence collection and focusing was done with a CFI Plan Apo VC 60XWI (Nikon) objective. Lenses L1 and L2 focussing the fluorescence on a 50 μ m pinhole (P50H, Thorlabs) were two tube lenses ($f=200$ mm, MXA20696, Nikon). Fluorescence

separation was done with dichroic 640DCXR (Chroma, DM3). For fluorescence clean-up the filters FF01-582/75 (Semrock) were used for donor and HQ650/100 (Chroma) for acceptor fluorescence. The signal was then collected with SPCM-AQRH-14 (Excelitas) APDs. TCSPC electronics were a TimeHarp 200 (Picoquant).

For the measurements a home written software based on LabView (National Instruments) and for the data reduction an Igor Pro (Wavemetrics) based home written software was used.

Kapanidis lab (confocal)

smFRET experiments were carried out on a custom-built confocal microscope^{39,40}, as shown schematically in Supplementary Figure 3. The setup was modified to allow ALEX of donor and acceptor fluorophores. Custom-written LabVIEW software was used to register and evaluate the detected signal.

Data analysis was carried out using custom-written Matlab software⁴¹.

Lamb lab (confocal)

Single-molecule FRET experiments with pulsed-interleaved excitation (PIE) and multiparameter fluorescence detection (MFD) were performed on a homebuilt confocal microscope as described previously⁴². In addition to the schematic shown in Supplementary Figure 3, a polarizing beam splitter is installed after the confocal pinhole to split the signal by polarization before the dichroic mirror (640DCXR, AHF Analysentechnik). Pulsed-interleaved excitation was performed at 532 nm (PicoTA 530, PicoQuant) and 640 nm (LDH-D-C640, PicoQuant) at a repetition rate of 26.67 MHz with a delay of ~18 ns and a laser power of 100 μ W. Fluorescence emission was filtered (donor: Brightline HQ582/75, acceptor: Brightline HQ700/75, AHF Analysentechnik), focused on avalanche photodiodes (SPCM-AQR, Perkin-Elmer) and recorded on single-photon-counting cards (SPC-154, Becker&Hickl). Data analysis was performed using the *PAM* software package written in MATLAB (The MathWorks)³⁶. Single-molecule events were identified using a sliding-time-window burst search algorithm with a countrate threshold of 10 kHz, a time window of 500 μ s and a minimum photon number of 100. To remove photoblinking and -bleaching events, the ALEX-2CDE filter was applied using an upper threshold of 10 (ref. ⁴³).

Lee lab (confocal)

We performed smFRET measurement using a home-built confocal microscope, similar with the setup described in Supplementary Figure 3, which has been well described in our previous works^{44,45}. The alternation of two lasers (ALEX) was achieved using acoustic-optic modulators. The data acquisition and analysis were performed using a home-built software based on LabVIEW program as described before⁴⁶.

Lemke lab (confocal)

The setup was as described in Supplementary Figure 3 and previously in detail in refs. ^{47,48}, with the following elements changed. Lasers were a LDH 485 (Picoquant) and a SuperK Extreme (NKT Potonics) filtered with a 572/15 bandpass alternating at 26,6 Mhz and combined onto the laser path with DM1= R488-Di01. Dichroic Mirror DM2 was a ZT 488/561/660 (AHF) and for DM3 a zt

561 RDC-UF (Chroma) and a FF650-D01 (Semrock) were used in sequence for three detection channels. For the three detection channels the filters 525/50 ET (Semrock), 620/60 ET (Chroma) and 700/75 ET (Chroma) were used. The analysis was done using self-written code in IgorPro (Wavemetrics) following procedures described in detail in refs.^{49,50}.

Levitus Lab (confocal)

Fluorescence intensity decays were acquired at room temperature using the timecorrelated single photon counting technique. A fiber supercontinuum laser (Fianium SC450) was used as the excitation source. The laser provides 6 ps pulses at a variable repetition rate, set at 20 MHz. The laser output was sent through an acousto-optical tunable filter (Fianium AOTF) to obtain 552 nm excitation. Fluorescence emission was collected at a 90° angle and detected using a double-grating monochromator (Jobin-Yvon, Gemini-180) and a microchannel plate photomultiplier tube (Hamamatsu R3809U-50). The emission monochromator was set to 580 nm. The polarization of the emission was collected at the magic angle relative to the excitation. A single photon counting card (Becker-Hickl, SPC830) was used for data acquisition. The IRF was measured with a 3% Ludox scattering solution (Sigma-Aldrich, MO) and had a fwhm of approximately 80 ps when measured at 552 nm. The data were deconvoluted and fitted with a sum of exponential terms using software written in-house (ASUFIT). The quality of the fit was evaluated based on the residuals.

Michaelis lab (Confocal)

The confocal setup used for this study has been described in detail recently⁵¹. It resembles the one depicted in supplementary figure 3, but with the major addition of polarization sensitivity. A polarizing beam splitting cube positioned after the collimating lens behind the pinhole splits the light into its components parallel and perpendicular with respect to the excitation light. Each of the two resulting beams is then split by a dichroic mirror and focused onto an APD after passing an emission filter, similar to what is shown in supplementary figure 3. Differing from Schwarz et al. 2018, a different polychroic mirror was used during the initial measurements of samples 1-lo, 1-mid, 2-lo and 2-mid (Triple Line zt488/532/658, AHF Analysentechnik AG, Tübingen, Germany). The setup also provides an additional 488nm laser line and the filters and dichroic mirrors can be exchanged in order to perform smFRET experiments with a 488nm-excitable donor and a 647nm-excitable acceptor (e.g. samples 3-lo and 3-mid described in supplementary note 6).

For data analysis, an earlier version of the software package PAM (PIE analysis with MATLAB) was used³⁶. The newest version of the software is available via <https://gitlab.com/PAM-PIE/PAM>.

Michaelis lab (TIRF)

All TIRF-measurements were conducted using a custom-build prism-type TIRF setup which has been described in detail recently⁵². The setup is similar to the setup described in Supplementary Figure 4, only with some minor additions namely an acousto-optic tunable filter (AOTFnC-VIS, AA Opto-Electronic) and an IR-laser based auto-focus system. The AOTF allows for the selection of the excitation wavelength and the control of laser intensity and duration.

The acquired data was analyzed using a custom-written software called *SM-FRET* which was described in detail⁵².

Sanabria Lab (confocal)

The home built confocal system and data analysis at the Sanabrias' lab was recently described in detail^{53,54}. It is similar to the one described in Supplementary Figure 3, but with four detectors and different spectral windows. Differences are briefly described below. The microscope body is an Olympus IX-73 with a 60X, 1.2 NA collar (0.17) corrected Olympus objective. It uses Pulsed Interleaved Excitation (PIE)⁴² with diode lasers at 485 nm and 640 nm (PicoQuant, Germany) operated at 40 MHz with 25 ns interleaved time. The power at the objective was 120 μ W at 485 nm and 39 μ W at 640 nm. Emitted photons were collected through the same objective and spatially filtered through a 70 μ m pinhole to limit the effective confocal detection volume. Fluorescence emission is separated into parallel and perpendicular polarization components at two different spectral windows using band pass filters ET525/50 and ET720/150 (Chroma Technology Co.) for donor and acceptor, respectively. In total, four photon-detectors are used—two for donor (PMA Hybrid model 40 PicoQuant, Germany) and two for acceptor (PMA Hybrid model 50, PicoQuant, Germany). To insure temporal data registration of the 4 synchronized input channels, we used a HydraHarp 400 TCSPC module (PicoQuant, Germany) in Time-Tagged Time-Resolved mode. Data analysis uses Multiparameter Fluorescence Detection software suit developed at the Seidel's lab (<http://www.mpc.hhu.de/software/software-package.html>).

Schlierf Lab (confocal)

Observations of single-molecule fluorescence were made on a custom-built dual-color and dual-polarization confocal setup based on an inverted microscope (Eclipse Ti-E, Nikon, Tokyo, Japan) as previously described in^{55,56}. Briefly, donor and acceptor fluorophores were excited with linearly polarized 530-nm and 640-nm picosecond pulsed laser sources (LDH-P-FA-530L and LDH-D-C-640, both from PicoQuant, Berlin, Germany) driven in pulsed interleaved excitation mode at a total repetition rate of 50 MHz. The laser beams were coupled to a polarization-maintaining single-mode optical fiber (P3-488PM-FC-2, Thorlabs, NJ, USA), collimated (60FC-T-4-RGBV42-47, Schäfter und Kirchhoff, Hamburg, Germany), and focused by a water immersion objective (CFI Plan Apo WI 60x, NA 1.2, Nikon). Emitted fluorescent light was collected by the same objective, separated from the excitation light by a dual-edge dichroic mirror (zt532/642rpc, Chroma, Bellows Falls, VT, USA), and focused on a 50- μ m pinhole (Thorlabs). Donor and acceptor photons were spectrally separated by single-edge dichroic mirrors (FF650-Di01, Semrock, USA) after a polarizing beam splitter (CM1-PBS251, Thorlabs), band-pass-filtered (FF01-582/75, Semrock, Rochester, NY, USA; ET700/75M, Chroma), and focused onto four single-photon-counting avalanche diodes (τ -SPADs, PicoQuant). Photons were registered by four individual time-correlated single-photon counting modules (Hydra Harp, PicoQuant) with a time resolution of 16 ps. Synchronization with the lasers for alternating excitation was accomplished with the aid of a diode laser driver (PDL828, PicoQuant).

Data analysis was performed with custom-written Matlab scripts (Mathworks, USA) and single-molecule events were identified from the acquired photon stream by a burst search algorithm as described in^{57,58}. The analysis software is available upon request.

Schuler Lab (confocal)

A commercial confocal instrument (MT200, PicoQuant, Berlin) or a custom-built instrument⁵⁹ were used for the measurements. Both instruments were equipped with an UplanApo 60×/1.20-W objective (Olympus), a 100-μm confocal pinhole, and HydraHarp 400 counting electronics (PicoQuant, Berlin). They were operated with pulsed interleaved excitation (20 MHz) in a configuration similar to that shown in Supplementary Figure 3 with the following components.

In the MT200 setup a 485-nm pulsed diode laser (LDH-D-C-485, Picoquant) was used for donor excitation, and a SC-450-4 supercontinuum fiber laser (Fianium) filtered with a z582/15 bandpass filter (Chroma) for acceptor excitation. Dichroic mirror DM2 was a BS R405/488/594 (Semrock) and DM3 a 585DCXR (Chroma). Donor fluorescence was filtered with a ET 525/50 (Chroma) and recorded with a SPCM-AQRH-14 (PerkinElmer Optoelectronics) APD. Acceptor fluorescence was filtered with an HQ 650/100 (Chroma) and recorded with a SPCM-AQR-14 APD (PerkinElmer Optoelectronics) APD.

In the custom built setup, the donor was excited with a SC-450-4 supercontinuum fiber laser (Fianium) filtered with a BrightLine HC 520/5 band-pass filter (Semrock) and acceptor excitation was done with a 635nm pulsed diode laser (LDH-D-C-635M, PicoQuant). In this instrument, the dichroic mirrors here were a zt405/530/630rpc (Chroma) for DM2 and a 635DCXR (Chroma) for DM3. Donor fluorescence was filtered with an ET585/65m (Chroma) and recorded with a τ-SPAD (PicoQuant). Acceptor fluorescence was cleaned up with LP647RU and HC750/SP (Chroma) filters and recorded with an SPCM-AQR-14 APD (PerkinElmer Optoelectronics). Data were analyzed using custom-developed software written in C++ and Mathematica.

Seidel Lab

Ensemble Time Correlated Single Photon Counting (eTCSPC)

Fluorescence lifetime decays were recorded by FT300 setup (PicoQuant, Germany) using a white light laser from NKT Photonics (Germany) with repetition rate 20 MHz for excitation. All samples were measured in Quartz Ultra-Micro-cuvettes (Helma #105.252.85.40), with a total sample volume of 20μl. A Ludox scattering solution was used to record the instrument response function (IRF). The detailed measurement conditions for the experiments are provided in the Table N8.1.

Table N8.1: Settings for Picoquant FT300 setup

Settings/dye	Atto 550	Alexa 488	Atto 647N	Alexa647	Alexa 594
Excitation, nm	552	485	635	635	590
Emission, nm	580	520	665	665	617
Bandpass, nm	5.4	9.2	9.2	8.1	8.1
Excitation filter	none	ZET 488/10x	ZET 635/20x	ZET 635/20x	none
Emission filter	FGL 570	FGL 515	FGL 645	FGL 645	FGL 610

Confocal setup 1 (for samples labelled with Alexa488-Atto647N)

The general scheme of the setup is described by Sisamakris et al⁵⁰ (see Fig. 18.5 therein). All sample solutions were measured in NUNC chambers (Lab-Tek, Thermo Scientific, Germany) with 300 μ L sample volume. The fluorescent donor molecules (Alexa 488) are excited by a pulsed diode laser (LDH-D-C 485, PicoQuant), at 485 nm operated at 64 MHz, 110 μ W at the sample in one color excitation experiment or at 32 MHz in PIE experiment, 110 μ W at the sample. The laser light is guided into the epi-illuminated confocal microscope (Olympus IX71, Hamburg, Germany) by dichroic beamsplitter FF500/646-Di01 (Semrock, USA) focussed by a water immersion objective (UPlanSApo 60x/1.2w, Olympus Hamburg, Germany). In PIE experiments the fluorescent acceptor molecules (Atto647N) are additionally excited by 635 nm pulsed diode laser (LDH-D-C 640, PicoQuant). The emitted fluorescence is collected through the objective and spatially filtered using a pinhole with typical diameter with 100 μ m. Then, the signal is split into parallel and perpendicular components via a polarizing beam splitter and then at two different spectral windows (e.g. “green” and “red”) and then split again using 50/50 beam splitters resulting in a total of eight detection channels. Additionally green (HQ 520/35 nm for Alexa488) from AHF, Tübingen, Germany and red (HQ 720/150 nm for Atto647N) bandpass filters (AHF, Tübingen, Germany) are placed in front of the detectors to provide the registration only of the fluorescence photons coming from the acceptor and donor molecules. Detection is performed using eight avalanche photodiodes (4 green channels: τ -SPAD (PicoQuant, Germany) and 4 red channels: AQR 14 (Perkin Elmer). The detector outputs were recorded by a TCSPC module (HydraHarp 400, PicoQuant).

Confocal setup 2 (for samples labelled with Atto550-Atto647N)

The confocal setup 2 is similar to the confocal setup 1 described above. It has the following components (only the differences are mentioned):

Confocal microscope: Olympus IX71 (Hamburg, Germany).

Objective: Olympus UPlanSApo 60x/1.2w (Hamburg, Germany).

Dichroic Beamsplitter: F68-532_zt532/640NIRrpo (AHF, Tübingen, Germany).

Fluorescence dichroic beamsplitter: T640lpxr (AHF, Tübingen, Germany).

Diode lasers: 530 nm (LDH-P-FA 530B, PicoQuant) and 640 nm (LDH-D-C 640, PicoQuant), both with a repetition rate 32 MHz and with a power 75.5 μ W and 16.7 μ W at the sample, respectively.

Bandpass filters: green ET595/50 and red HQ730/140.

2 green and 2 red detectors: both SPCM-AQRH 14 (Excelitas, USA).

Confocal setup 3 (for samples labelled with Alexa488-Alexa594)

The confocal setup 3 is similar to the confocal setup 1 described above. It has the following components (only the differences are mentioned):

Confocal microscope (Olympus IX70, Hamburg, Germany).

Dichroic beam splitter: Q505LP (AHF, Tübingen, Germany).

Fluorescence dichroic beamsplitter: 595 LP DCXR (AHF, Tübingen, Germany).

Diode lasers: 495 nm (PicoQuant, Germany) with a repetition rate of 32 MHz and a power at the sample of 110 μ W.

Bandpass filters: green HQ520/66, red HQ630/60.

2 green and 2 red detectors: SPCM-AQRH 14 (Perkin Elmer).
TCSPC module SPC 132 (Becker&Hickl, Germany).

The recorded data were analyzed with a home-written LabView software that was developed in the Seidel lab and is described in ref. ⁵⁰. The software is available on the homepage of the Seidel group (<http://www.mpc.hhu.de/software/software-package.html>).

To analyze the recorded fluorescence bursts, a burst search algorithm according to reference ⁶⁰ was applied. The confocal setups were calibrated by the PIE measurements as described in this work or by FRET-lines relating the donor fluorescence lifetime to the intensity-based FRET efficiency as described in ref. ⁶¹.

Tinnefeld lab (confocal)

The measurements were carried out on a custom-built confocal microscope ⁶² based on an IX 71 (Olympus) similar to the setup shown in Supplementary Figure 3 with alternating laser excitation. Pulsed Lasers (637 nm, 80 MHz, LDH-D-C-640; 532 nm 80 MHz, LDH-P-FA-530B; both PicoQuant) were powered by a Sepia 2 (PicoQuant) unit. Both lasers were combined by a dichroic mirror (640 LPXR, AHF). In addition to the setup shown in Supplementary Figure 3, the lasers were alternated by an acousto optical tunable filter (AOTFnc-VIS, AA optoelectronic) and coupled into a single mode fiber (P3-488PM-FC-2, Thorlabs) to obtain a Gaussian beam profile. After a linear polarizer (LPVISE100 A, Thorlabs) and lambda quarter plate (AQWP05M 600, Thorlabs), circular polarized light was obtained. After a dual band dichroic beam splitter (z532/633, AHF), the light was focused by an oil-immersion objective (UPLSAPO 100XO, NA 1.40, Olympus). The emitted light was collected by the same objective and focused on a 50 μm pinhole (Linos). Subsequently, the fluorescence was split by a dichroic mirror (640DCXR, AHF) into a green (Brightline HC582/75, AHF; RazorEdge LP 532, Semrock) and red (Bandpass ET 700/75m, AHF; RazorEdge LP 647, Semrock) detection channel. Two SPADs (τ -SPAD 100, PicoQuant) accounted for the detection. The SPAD signals were registered by a TCSPC card (SPC-830, Becker&Hickl). The setup was controlled with custom-made LabView (National Instruments) software. Recorded data were analyzed with a LabView software ⁶³. To analyze the recorded fluorescence bursts, a burst search algorithm according to reference ⁶⁴ was applied.

Weninger lab (TIRF)

The microscope is similar to that in Supplementary Figure 4 ³¹. Briefly, we illuminate immobilized samples at the surface of a quartz microscope slide with prism-type total internal reflection of laser beams at the quartz/buffer interface. Alternating illumination of 532 nm or 640 nm allows sequential excitation of donor and acceptor dyes when using Atto 550, Alexa 647 and Atto 647N. Fluorescence emission is collected by a 1.20 N.A. water-immersion microscope objective (Olympus UIS2 UPlanSApo 60x/1.20 W). The fluorescence image is spectrally divided with a Dualview splitter (DV2, Photometrics) incorporating a 645dcxr dichroic mirror with a 585/70 bandpass filter (donor) and a 700/75 bandpass filter (acceptor) (all from Chroma Technology Corp.). The spectrally divided image is detected with an emCCD (Cascade 521B, Photometrics) operating at 10 Hz.

We use home-written analysis software implemented in MATLAB (MathWorks)³². Immobilized single molecules are detected in a ten-frame averaged image as pixels of maximum intensity above an empirically determined threshold (typically based on the statistics of all pixels in the field of view as 7 standard deviations above the average), separated by five or more pixels from any neighboring maxima. Fluorescence intensity for a single molecule is extracted from each frame of a movie as the sum of the 4 brightest pixels in a 3x3 pixel region centered on the local maximum. Before a FRET experiment, we acquire a spectrally split image of a field of immobilized, fluorescent 100 nm diameter polystyrene spheres that emit broadly into both channels to build a mapping between donor and acceptor channels using the MATLAB image processing toolbox command `cp2tform`. This mapping is applied to movies containing FRET data to obtain donor and acceptors intensities from immobilized single molecules. Background for each detected molecule is calculated locally as the median value of the 16x16 pixel region around the identified peak pixel. The background value is subtracted from the single molecule intensity values. The background value is verified by requiring the background-subtracted intensity time-trace for a single molecule emission return to zero upon a single step photobleaching event. Leakage between donor and acceptor channels is measured separately using singly labeled samples. FRET efficiency is then calculated as described in the main text.

Bibliography:

1. Sindbert, S. *et al.* Accurate Distance Determination of Nucleic Acids via Förster Resonance Energy Transfer: Implications of Dye Linker Length and Rigidity. *J. Am. Chem. Soc.* **133**, 2463-2480 (2011).
2. Widengren, J. & Schwille, P. Characterization of photoinduced isomerization and back-isomerization of the cyanine dye Cy5 by fluorescence correlation spectroscopy. *J. Phys. Chem. A* **104**, 6416-6428 (2000).
3. Widengren, J., Schweinberger, E., Berger, S. & Seidel, C. A. M. Two new concepts to measure fluorescence resonance energy transfer via fluorescence correlation spectroscopy: Theory and experimental realizations. *J. Phys. Chem. A* **105**, 6851-6866 (2001).
4. Hendrix, J. & Lamb, D. C. Pulsed Interleaved Excitation: Principles and Applications. *Fluorescence Fluctuation Spectroscopy (Ffs), Pt A* **518**, 205-243 (2013).
5. Margeat, E. *et al.* Direct Observation of Abortive Initiation and Promoter Escape Within Single Immobilized Transcription Complexes. *Biophys. J.* **90**, 1419-1431 (2006).
6. Peulen, T. O., Opanasyuk, O. & Seidel, C. A. M. Combining graphical and analytical methods with molecular simulations to analyze time-resolved FRET-measurements of labeled macromolecules accurately. *J. Phys. Chem. B* **121**, 8211-8241 (2017).
7. Wozniak, A. K., Schröder, G. F., Grubmüller, H., Seidel, C. A. M. & Oesterhelt, F. Single-Molecule FRET Measures Bends and Kinks in DNA. *Proc. Natl. Acad. Sci. USA* **105**, 18337-18342 (2008).
8. Ivani, I. *et al.* Parmbsc1: a refined force field for DNA simulations. *Nat. Meth.* **13**, 55-58 (2016).
9. Muschielok, A. *et al.* A Nano-Positioning System for Macromolecular Structural Analysis. *Nat. Meth.* **5**, 965-971 (2008).
10. Kalinin, S. *et al.* A toolkit and benchmark study for FRET-restrained high-precision structural modeling. *Nat. Meth.* **9**, 1218-1227 (2012).

11. Hellenkamp, B., Wortmann, P., Kandzia, F., Zacharias, M. & Hugel, T. Multidomain Structure and Correlated Dynamics Determined by Self-Consistent FRET Networks. *Nat. Meth.* **14**, 174-180 (2017).
12. Beckers, M., Drechsler, F., Eilert, T., Nagy, J. & Michaelis, J. Quantitative Structural Information from Single-Molecule FRET. *Farad. Discuss.* **184**, 117-129 (2015).
13. Dimura, M. *et al.* Quantitative FRET Studies and Integrative Modeling Unravel the Structure and Dynamics of Biomolecular Systems. *Curr. Opin. Struct. Biol.* **40**, 163-185 (2016).
14. Nagy, J., Eilert, T. & Michaelis, J. Precision and Accuracy in smFRET based structural studies - a benchmark study of the FAST-Nano-Positioning System. *J. Chem. Phys.* **148** (2018).
15. Treutlein, B. *et al.* Dynamic architecture of a minimal RNA polymerase II open promoter complex. *Mol. Cell* **46**, 136-146 (2012).
16. Hohlbein, J. *et al.* Conformational landscapes of DNA polymerase I and mutator derivatives establish fidelity checkpoints for nucleotide insertion. *Nat. Commun.* **4**, 2131 (2013).
17. Tyagi, S. & Lemke, E. A. Genetically encoded click chemistry for single-molecule FRET of proteins. *Methods Cell Biol.* **113**, 169-187 (2013).
18. Tyagi, S. & Lemke, E. A. Single-molecule FRET and crosslinking studies in structural biology enabled by noncanonical amino acids. *Curr. Opin. Struct. Biol.* **32**, 66-73 (2015).
19. Eilert, T., Beckers, M., Drechsler, F. & Michaelis, J. Fast-NPS - A Markov chain Monte Carlo-based analysis tool to obtain structural information from single-molecule FRET measurements. *Comput. Phys. Commun.* **219**, 377-389 (2017).
20. Lipfert, J. *et al.* Double-stranded RNA under force and torque: Similarities to and striking differences from double-stranded DNA. *Proc. Natl. Acad. Sci. USA* **111**, 15408-15413 (2014).
21. Liebl, K., Drsata, T., Lankas, F., Lipfert, J. & Zacharias, M. Explaining the striking difference in twist-stretch coupling between DNA and RNA: A comparative molecular dynamics analysis. *Nucleic Acids Res.* **43**, 10143-10156 (2015).
22. Stelzl, L. S., Erlenbach, N., Heinz, M., Prisner, T. F. & Hummer, G. Resolving the conformational dynamics of DNA with Ångström resolution by pulsed electron-electron double resonance and molecular dynamics. *J. Am. Chem. Soc.* **139**, 11674-11677 (2017).
23. Vafabakhsh, R. & Ha, T. Extreme Bendability of DNA Less than 100 Base Pairs Long Revealed by Single-Molecule Cyclization. *Science* **337**, 1097-1101 (2012).
24. Case, D. A. *et al.* AMBER 2016. (University of California, San Francisco, 2016).
25. Jorgensen, W. L., Chandrasekhar, J., Madura, J. D., Impey, R. W. & Klein, M. L. Comparison of Simple Potential Functions for Simulating Liquid Water. *J. Chem. Phys.* **79**, 926-935 (1983).
26. Joung, I. S. & Cheatham, T. E. Determination of alkali and halide monovalent ion parameters for use in explicitly solvated biomolecular simulations. *J. Phys. Chem. B* **112**, 9020-9041 (2008).
27. Li, P. F., Roberts, B. P., Chakravorty, D. K. & Merz, K. M. Rational design of particle mesh ewald compatible Lennard-Jones parameters for +2 metal cations in explicit solvent. *J. Chem. Theory Comput.* **9**, 2733-2748 (2013).
28. Gohlke, H., Kiel, C. & Case, D. A. Insights into protein-protein binding by binding free energy calculation and free energy decomposition for the Ras-Raf and Ras-RalGDS complexes. *J. Mol. Biol.* **330**, 891-913 (2003).
29. Kruger, A. C., Hildebrandt, L. L., Kragh, S. L. & Birkedal, V. Structural dynamics of nucleic acids by single-molecule FRET. *Methods Cell Biol.* **113**, 1-37 (2013).
30. Preus, S., Noer, S. L., Hildebrandt, L. L., Gudnason, D. & Birkedal, V. iSMS: single-molecule FRET microscopy software. *Nat Methods* **12**, 593-594 (2015).
31. McCann, J. J., Choi, U. B., Zheng, L., Weninger, K. & Bowen, M. E. Optimizing Methods to Recover Absolute FRET Efficiency from Immobilized Single Molecules. *Biophys. J.* **99**, 961-970 (2010).

32. Choi, U. B., Weninger, K. R. & Bowen, M. E. Immobilization of proteins for single-molecule fluorescence resonance energy transfer measurements of conformation and dynamics. *Methods Mol. Biol.* **896**, 3-20 (2012).
33. Gouridis, G. *et al.* Conformational dynamics in substrate-binding domains influences transport in the ABC importer GlnPQ. *Nat. Struct. Mol. Biol.* **22**, 57-64 (2015).
34. Bennet, I. A. *et al.* Regional conformational flexibility couples substrate specificity and scissile phosphate diester selectivity in human flap endonuclease 1. *Nucleic Acids Res.* **46**, 5618-5633 (2018).
35. Hua, B. *et al.* An improved surface passivation method for single-molecule studies. *Nat Methods* **11**, 1233-1236 (2014).
36. Schrimpf, W., Barth, A., Hendrix, J. & Lamb, D. C. PAM: A Framework for Integrated Analysis of Imaging, Single-Molecule, and Ensemble Fluorescence Data. *Biophys. J.* **114**, 1518-1528 (2018).
37. Farooq, S. & Hohlbein, J. Camera-based single-molecule FRET detection with improved time resolution. *Phys. Chem. Chem. Phys.* **17**, 27862-27872 (2015).
38. Holden, S. J. *et al.* Defining the limits of single-molecule FRET resolution in TIRF microscopy. *Biophys. J.* **99**, 3102-3111 (2010).
39. Santoso, Y. *et al.* Conformational transitions in DNA polymerase I revealed by single-molecule FRET. *Proc Natl Acad Sci U S A* **107**, 715-720 (2010).
40. Robb, N. C. *et al.* The transcription bubble of the RNA polymerase-promoter open complex exhibits conformational heterogeneity and millisecond-scale dynamics: implications for transcription start-site selection. *J. Mol. Biol.* **425**, 875-885 (2013).
41. Tomescu, A. I., Robb, N. C., Hengrung, N., Fodor, E. & Kapanidis, A. N. Single-molecule FRET reveals a corkscrew RNA structure for the polymerase-bound influenza virus promoter. *Proc Natl Acad Sci U S A* **111**, E3335-3342 (2014).
42. Kudryavtsev, V. *et al.* Combining MFD and PIE for Accurate Single-Pair Förster Resonance Energy Transfer Measurements. *ChemPhysChem* **13**, 1060-1078 (2012).
43. Tomov, T. E. *et al.* Disentangling Subpopulations in Single-Molecule FRET and ALEX Experiments with Photon Distribution Analysis. *Biophys. J.* **102**, 1163-1173 (2012).
44. Kim, C., Kim, J. Y., Kim, S. H., Lee, B. I. & Lee, N. K. Direct characterization of protein oligomers and their quaternary structures by single-molecule FRET. *Chem Commun (Camb)* **48**, 1138-1140 (2012).
45. Kim, J. Y. *et al.* Solution single-vesicle assay reveals PIP2-mediated sequential actions of synaptotagmin-1 on SNAREs. *EMBO J.* **31**, 2144-2155 (2012).
46. Lee, N. K. *et al.* Accurate FRET Measurements Within Single Diffusing Biomolecules Using Alternating-Laser Excitation. *Biophys. J.* **88**, 2939-2953 (2005).
47. Milles, S., Koehler, C., Gambin, Y., Deniz, A. A. & Lemke, E. A. Intramolecular three-colour single pair FRET of intrinsically disordered proteins with increased dynamic range. *Mol Biosyst* **8**, 2531-2534 (2012).
48. Milles, S. & Lemke, E. A. Single Molecule Study of the Intrinsically Disordered FG-Repeat Nucleoporin 153. *Biophys. J.* **101**, 1710-1719 (2011).
49. Eggeling, C. *et al.* Data registration and selective single-molecule analysis using multi-parameter fluorescence detection. *J. Biotechnol.* **86**, 163-180 (2001).
50. Sisamakias, E., Valeri, A., Kalinin, S., Rothwell, P. J. & Seidel, C. A. M. Accurate Single-Molecule FRET Studies Using Multiparameter Fluorescence Detection. *Methods Enzymol.* **475**, 455-514 (2010).
51. Schwarz, M. *et al.* Single-molecule nucleosome remodeling by INO80 and effects of histone tails. *FEBS Lett.* **592**, 318-331 (2018).

52. Dörfler, T., Eilert, T., Rocker, C., Nagy, J. & Michaelis, J. Structural Information from Single-molecule FRET Experiments Using the Fast Nano-positioning System. *Jove-Journal of Visualized Experiments* (2017).
53. Dolino, D. M., Rezaei Adariani, S., Shaikh, S. A., Jayaraman, V. & Sanabria, H. Conformational selection and submillisecond dynamics of the ligand-binding domain of the N-methyl-D-Aspartate receptor. *J Biol Chem* **291**, 16175-16185 (2016).
54. Ma, J. *et al.* High Precision FRET at Single-molecule Level for Biomolecule Structure Determination. *J Vis Exp*, e55623 (2017).
55. Hartmann, A., Krainer, G. & Schlierf, M. Different fluorophore labeling strategies and designs affect millisecond kinetics of DNA hairpins. *Molecules* **19**, 13735-13754 (2014).
56. Krainer, G., Hartmann, A. & Schlierf, M. farFRET: Extending the Range in Single-Molecule FRET Experiments beyond 10 nm. *Nano Lett* **15**, 5826-5829 (2015).
57. Hartmann, A., Krainer, G., Keller, S. & Schlierf, M. Quantification of Millisecond Protein-Folding Dynamics in Membrane-Mimetic Environments by Single-Molecule Forster Resonance Energy Transfer Spectroscopy. *Anal. Chem.* **87**, 11224-11232 (2015).
58. Krainer, G., Hartmann, A., Anandamurugan, A., Gracia, P. & Schlierf, M. Ultrafast protein folding through polar interactions in membrane-mimetic environments. *J. Mol. Biol.* **430** (2018).
59. König, I. *et al.* Single-molecule spectroscopy of protein conformational dynamics in live eukaryotic cells. *Nat. Meth.* **12**, 773-779 (2015).
60. Fries, J. R., Brand, L., Eggeling, C., Kollner, M. & Seidel, C. A. M. Quantitative identification of different single molecules by selective time-resolved confocal fluorescence spectroscopy. *J. Phys. Chem. A* **102**, 6601-6613 (1998).
61. Kalinin, S., Valeri, A., Antonik, M., Felekyan, S. & Seidel, C. A. M. Detection of Structural Dynamics by FRET: A Photon Distribution and Fluorescence Lifetime Analysis of Systems with Multiple States. *J. Phys. Chem. B* **114**, 7983-7995 (2010).
62. Nickels, P. C. *et al.* Molecular force spectroscopy with a DNA origami-based nanoscopic force clamp. *Science* **354**, 305-307 (2016).
63. Kapanidis, A. N. *et al.* Fluorescence-aided molecule sorting: Analysis of structure and interactions by alternating-laser excitation of single molecules. *Proc. Natl. Acad. Sci. USA* **101**, 8936-8941 (2004).
64. Nir, E. *et al.* Shot-Noise Limited Single-Molecule FRET Histograms: Comparison Between Theory and Experiments. *J. Phys. Chem. B* **110**, 22103-22124 (2006).